THE ASTROPHYSICAL JOURNAL, 466:55–91, 1996 July 20

CEPHEID CALIBRATION OF THE PEAK BRIGHTNESS OF SNe Ia. V. SN 1981B IN NGC 4536

A. SAHA
Space Telescope Science Institute, 3700 San Martin Drive, Baltimore, MD 21218
ALLAN SANDAGE
Observatories of the Carnegie Institution of Washington, 813 Santa Barbara Street, Pasadena, CA 91101
LUKAS LABHARDT AND G. A. TAMMANN
Astronomisches Institut der Universität Basel, Venusstrasse 7, CH-4102 Binningen, Switzerland
AND
F. D. MACCHETTO[1] AND N. PANAGIA[1]
Space Telescope Science Institute, 3700 San Martin Drive, Baltimore, MD 21218
Received 1995 November 28; accepted 1996 February 6

ABSTRACT

Observations have been made with the *Hubble Space Telescope* between 1994 June and August over a 67 day interval, comprising 17 epochs in the F555W band and 5 epochs in the F814W band. The target was a region of an outlying spiral arm of NGC 4536 [Sbc(s)I–II], a galaxy that was parent to the type Ia supernova SN 1981B. Seventy-three Cepheids were found with periods ranging between 5.4 and 65 days. The apparent distance modulus of NGC 4536 is $(m - M)_{AV} = 31.23 \pm 0.05$ and $(m - M)_{AB} = 31.27 \pm 0.05$. There is no statistically significant differential absorption between the Cepheids inside and outside the spiral arm, or between the Cepheids and the position of the supernova (SN). The resulting absolute magnitudes of SN 1981B are $M_V(\max) = -19.32 \pm 0.12$ and $M_B(\max) = -19.29 \pm 0.13$ using the apparent modulus of NGC 4536 and the apparent magnitudes of SN 1981B as if there is no differential extinction between them. If we correct the SN for reddening, determined independently of the Cepheids, and then use the true modulus of NGC 4536 of $(m - M)_0 = 31.10 \pm 0.13$, the SN values are $M_B(\max) = -19.46 \pm 0.24$ and $M_V(\max) = -19.44 \pm 0.21$.

Combining these calibrations with the three calibrations previously available for the SNe 1895B, 1937C, and 1972E, determined in the first four papers of this series, gives the interim calibrations of $\langle M_B(\max)\rangle = -19.48 \pm 0.12$ and $\langle M_V(\max)\rangle = -19.47 \pm 0.10$. These require interim Hubble constants of

$$H_0(B) = 55 \pm 3(\text{internal}) \text{ km s}^{-1} \text{ Mpc}^{-1} ,$$

and

$$H_0(V) = 58 \pm 3(\text{internal}) \text{ km s}^{-1} \text{ Mpc}^{-1} .$$

Improvement is expected when the fifth and sixth calibrators, SN 1960F in NGC 4496A and SN 1990N in NGC 4639, are added to the four available here. When these data are available, any putative decay rate–absolute magnitude correlation can also begin to be studied directly from the Cepheid calibrations themselves.

Subject headings: Cepheids — distance scale — galaxies: distances and redshifts — galaxies: individual (NGC 4536) — supernovae: individual (SN 1981B)

1. INTRODUCTION

This is the fifth Paper of a series whose purpose is to determine Cepheid distances to galaxies that have produced well-observed, prototypical supernovae of Type Ia (SNe Ia). Available data for such "Branch normal" SNe Ia (Branch & Tammann 1992; Branch, Fisher, & Nugent 1993; Branch & Miller 1993; Branch et al. 1994; Fisher et al. 1995), when put into a Hubble diagram (apparent magnitude vs. log redshift), show a remarkably tight correlation about the linear redshift-distance line of slope $dm/d \log v = 5$ in both B and V (Sandage & Tammann 1993; Tammann & Sandage 1995; Hamuy et al. 1995). The intrinsic dispersion is smaller than 0.3 mag in both the B and V Hubble diagrams. Because of this, the calibration of $\langle M(\max)\rangle_{\text{SNeIa}}$ is expected to lead to a definitive value of the Hubble constant independent of all other distance indicator methods, circumventing many of the problems centered on the local velocity field. SNe Ia are observed at redshifts well beyond local streaming motions (i.e., to $v_0 > 30{,}000$ km s^{-1}) and also beyond the local deceleration of the expansion caused by the Virgo complex for redshifts smaller than 3000 km s^{-1}.

All other photometric indicators have, demonstrably, the considerably larger intrinsic dispersions of $\sigma(M) > 0.7$ mag (Sandage & Tammann 1996; Sandage 1988, 1995, 1996) in their absolute magnitudes versus the particular indicator

[1] Affiliated to the Astrophysics Division, Space Sciences Department of ESA.

(line width, PN and globular cluster luminosity functions, surface brightness fluctuations, luminosity classes, etc.). Hence, the SNe Ia method of distance determination is by far the most precise extant photometric method known, even accounting for a putative variation of peak brightness with decay rate first suggested by Pskovskii (1977, 1984) and brought forth again by Phillips (1993), but with four times too large a slope with its consequent exaggerated effect on H_0 (Tammann & Sandage 1995).

Earlier Papers in this series gave Cepheid distances for IC 4182, parent galaxy to SN 1937C (Sandage et al. 1992; Saha et al. 1994), and NGC 5253, parent galaxy of SN 1895 B and SN 1972E (Sandage et al. 1994; Saha et al. 1995). In the present Paper we report the discovery of Cepheids in NGC 4536, parent galaxy to the prototypical Branch normal SN Ia 1981B. The observations were made with the *Hubble Space Telescope* (*HST*) in cycle 4, after repair.

NGC 4536 is of type and luminosity class Sbc(s) I–II. It is in the very busy region often called the "Southern Extension" of the Virgo complex. Its position is R.A.(1950) = $12^h31^m54^s$ and decl.(1950) = $+02°27'.7$ ($l = 293°$, $b = +65°$). Its association, if at all, with the elliptical-rich A and B double cores of the Virgo Cluster itself (Binggeli et al. 1985, 1987) is unknown. But such is irrelevant for the present SNe calibration experiment. We make no use of any putative connection of NGC 4536 either with a possible Virgo complex membership, or any information considering the *range* of distances within the complex itself, or of any velocity data either for NGC 4536 or for the Virgo complex relative to the microwave background. For this experiment we need only the Cepheid distance to the parent galaxy to calculate the absolute peak luminosity of SN 1981B. It is this advantage that the SN method has for the determination of the Hubble constant over all other photometric methods. We read the SNe Hubble diagrams at very large redshifts.

Seventy-three Cepheids have been discovered in the northwest outer arm of NGC 4536 using *HST*, based on 17 epochs in F555W and 5 epochs in F814W, taken over a 67 day interval between 1994 June and August. The periods of the Cepheids range from 5.4 to 65 days. The mean V magnitudes (integrated as intensities over the light curve) range from 24.5 to 27.6.

The plan of the paper is to discuss in § 2 the techniques used to handle images, given data which undersample the telescope point spread function. The method used for photometry, essentially a variant of the DoPHOT program, is described in § 3, again emphasizing the special circumstances presented by the undersampling. The route from instrumental magnitudes to calibrated standard magnitudes is also laid out.

The identification, classification, light curves in V and I, and final adopted periods and mean magnitudes of the variables are set out in § 4. The P-L relation for different quality classes of the data, and for different positions of the Cepheids relative to the spiral arm of NGC 4536, are discussed in § 5, leading to the adopted true distance modulus of NGC 4536. The resulting peak absolute luminosity of SN 1981B is presented in § 6. A comparison is made in § 7 of the adopted absolute magnitudes of SN 1981B with the M_B(max) and M_V(max) values for SNe 1895B, 1937C, and 1972E from the previous experiments in this series, leading to a new interim value of H_0. Proof that the large range in the measured ($\langle V\rangle - \langle I\rangle$) colors of the Cepheids is not due to differential reddening but probably due to observational errors is given in the Appendix. The brightest resolved stars are also discussed there.

2. OBSERVATIONS AND PRELIMINARY PROCESSING

2.1. *The Data*

Repeat images were obtained using the WFPC2 (Holtzman et al. 1995a) of the *Hubble Space Telescope* of a field in NGC 4536 that includes almost all of the northwest spiral arm. The field is shown in Figure 1 (Plate 1), overlaid on a ground-based image. These images show that the field has several tens of thousands of resolved stars, well-suited to finding Cepheids.

There are 17 discrete epochs in the F555W passband, and 5 epochs in the F814W passband. The epochs were spaced strategically (Saha 1996 for the method) over a two-month period to provide maximum leverage on detecting and finding periods of Cepheid variables over the period range 10–60 days. The two-month period is constrained by the time window during which this target can be observed with *HST* without altering the field orientation, while at the same time keeping the spacecraft orientation with respect to the Sun within allowed limits. Each epoch in each filter is made of 2 subexposures taken back to back on successive orbits of the spacecraft. This allows the removal of cosmic rays by an anticoincidence technique. The images from various epochs are co-aligned to within 3–4 pixels on the scale of the PC, except for the very first epoch, where the displacement is about 25 pixels in each direction on the PC. The journal of observations is given in Table 1.

The images were processed through the regular calibration pipeline, including bias subtraction and field flattening. During the first few months after deployment, the WFPC2 CCDs were cooled to −76° C. This was later altered, and the chips were cooled to −88° C to reduce adverse signatures from charge transfer anomalies in these chips. All the data for NGC 4536 in this paper were taken after the change over to the operating temperature of −88° C which minimizes the charge transfer problems

TABLE 1

JOURNAL OF OBSERVATIONS

Data Archive Designation	HJD at Midexposure	Filter	Exposure Time (s)
U2690I01T + ...02T	2,449,506.80033	F555W	4000
U2690J01T + ...02T	2,449,520.68030	F555W	4000
U2690J03T + ...04T	2,449,520.81153	F814W	4000
U2690K01T + ...02T	2,449,521.95448	F555W	4000
U2690L01T + ...02T	2,449,526.64569	F555W	4000
U2690M01T + ...02T.....	2,449,528.65592	F555W	4000
U2690N01T + ...02T	2,449,531.87297	F555W	4000
U2690N03T + ...04T	2,449,532.00420	F814W	4000
U2690O01T + ...02T	2,449,533.41448	F555W	4000
U2690P01T + ...02T	2,449,536.76624	F555W	4000
U2690T01T + ...02T	2,449,545.95008	F555W	4000
U2690T03T + ...04T	2,449,546.08062	F814W	4000
U2690U01T + ...02T	2,449,550.97739	F555W	4000
U2690W01T + ...02T.....	2,449,559.89117	F555W	4000
U2690W03T + ...04T.....	2,449,560.02171	F814W	4000
U2690Q01T + ...02T	2,449,562.97424	F555W	4000
U2690V01T + ...02T	2,449,564.64632	F555W	4000
U2690V03T + ...04T	2,449,564.78033	F814W	4000
U2690X01T + ...02T	2,449,566.66073	F555W	4000
U2690S01T + ...02T.....	2,449,569.61050	F555W	4000
U2690R01T + ...02T	2,449,571.75547	F555W	4000
U2690Y01T + ...02T	2,449,573.69977	F555W	4000

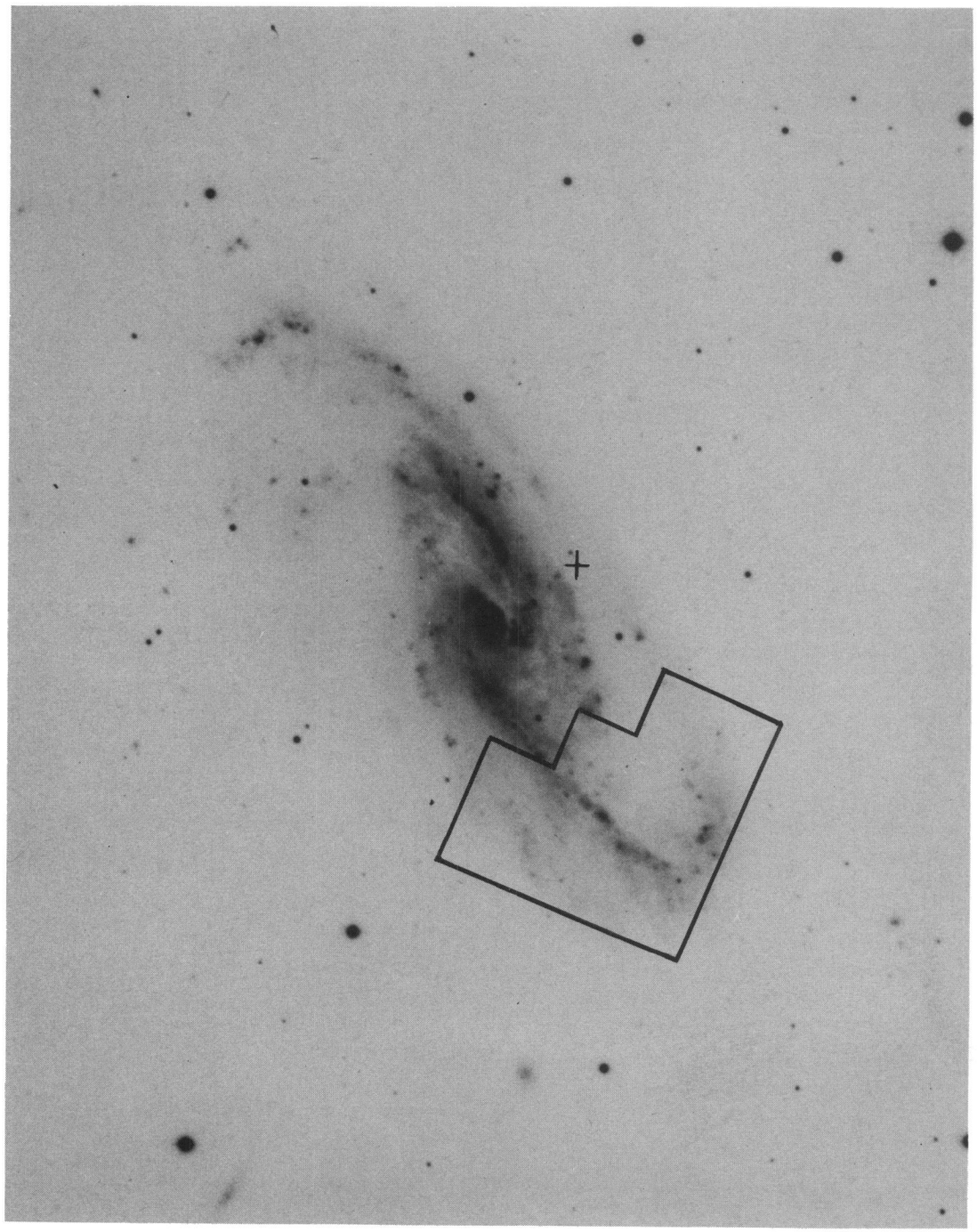

FIG. 1.—Ground-based image of NGC 4536 obtained on 1982 March 22–23 with the du Pont 2.5 m Telescope at Las Campanas. Emulsion 103a0 (blue), no filter (Carnegie Atlas, Panel 174). Position of the *HST* field is superposed. Approximate position of SN 1981B is marked. East is up; north is to the right.

inherent to the chips used in the WFPC2. The results from the photometric analysis (next section) show that the instrument and device response did not change noticeably during the 67 day window spanned by the data epochs.

2.2. *Removal of Cosmic Rays*

Pairs of back to back exposures described above were used to eliminate cosmic ray events at the 4–5 σ level relative to a noise model that includes photon statistics and device readout noise. Due to the extreme spatial undersampling[2] in the images (particularly in the Wide Field modules), small subpixel changes in registration of the images and/or changes in jitter in the spacecraft guiding, the signal in the pixels near peaks of bright stars can change significantly. For this reason, the usual simple anticoincidence technique of removing cosmic ray hits for a pair of images will detect spurious events in the centers of bright stars.

A special alogrithm was designed to work around this problem. This procedure takes a pair of images that have been aligned to within an integer pixel, coadds them, and identifies pixels that are anticoincident at the n σ level. When checking for anticoincidence, exposure time differences between the pair of exposures are scaled, and an additional offset in the overall background level (due to differences in sky brightness, scattered light, etc.) is allowed for. Consider a pixel in image A, that is flagged as being too high compared to its counterpart in image B. To ensure that altering this pixel would not truncate the peak of a bona fide star, the following steps are taken:

1. Find the pixel with the maximum signal in a 3 × 3 pixel region in image B, centered about the pixel that corresponds to the alleged high pixel in image A. Let this value be $f_b^{\max}$. Denote the value of the alleged high pixel in image A by f_a. Let the exposure times for images A and B be t_a and t_b respectively.
2. Calculate q_a and q_b, which denote the first 20th percentile value of a 5 × 5 region around the pixels in question on images A and B, respectively. These quantities measure the "local background" around these pixels.
3. Calculate the quantity $R = [(f_a - q_a) \times t_b]/[(f_b^{\max} - q_b) \times t_a]$. If R is not sufficiently larger than unity, the difference in pixel values may be caused by peaks of stars moved around by registration differences or by changes in spacecraft jitter. The critical value of R above which such a procedure never truncates the peak of a bright star is found empirically by experimentation, and denoted by r.
4. The alleged pixel in image A is judged to be a cosmic-ray hit only if R is greater than r, in which case the pixel value f_a is "corrected" by replacing it with $q_a + [(f_b^{\max} - q_b)t_a/t_b]$. Alternatively one can replace it by a mask value that ensures that the pixel is not used in any further processing.

Values of $n = 4$ and $r = 2$ (as used above) were found to be optimal. Note that this procedure is biased: while cosmic rays are removed efficiently in the spaces between stars, weak cosmic-ray hits on top of cores of stars will not be removed. However, these hits are unremovable anyway, and must be considered an inherent shortcoming of the data. The net result is that some objects will be mismeasured as too bright at any given epoch due to cosmic ray hits on the cores of the stellar point spread function (PSF).[3]

The method can also be used to combine images from several epochs to make a deep *master frame*, provided the images are co-aligned to within a few pixels to begin with (otherwise geometrical distortions in the WFPC2 field will necessitate rebinning the images: not wise for photometry).

3. PHOTOMETRY

The extremely undersampled data from WFPC2 pose interesting challenges in the way of extracting maximum information of faint stars in crowded fields. There is also the great paucity of calibration standards and data to tie observations to a standard photometric system. A self-consistent approach to cope with this situation was developed as part of this project. Since the veracity of the final results depends critically on photometric methods, the procedure begs description.

3.1. *Relative Photometry from PSV Fitting*

A special variant of the PSF photometry program DoPHOT (Schechter, Mateo, & Saha 1993) was created, optimized to the vagaries of undersampled *HST* WFPC2 data. Two aspects of this variant are noteworthy: (1) the form of the analytic point spread function is more flexible, to deal better with the tight cores but flared (near-Lorentzian) wings of the WFPC2 images, and (2) a tighter discrimination between stars and cosmic rays or hot pixels inherent in the individual CCD chips that remain unremoved (particularly faint ones, and those that appear in the residuals of stellar cores after PSV subtraction) is implemented, since in these undersampled images, their separation is harder than what standard DoPHOT was originally designed to effect. Hereafter in this paper the term DoPHOT will refer to this variant program, and not to the standard version.

Images from 8 epochs in F555W were combined to make a deep reference image. DoPHOT was then run on these deep images to produce a catalog list of objects. DoPHOT was then independently run on the images taken at each epoch. Several hundred of the brightest available bona fide stars (as classified by DoPHOT) were then cross-matched to the deep image and the geometrical transformation from the deep image to the images at each separate epoch were derived. For each epoch, the catalog list of objects from the deep image were thus transformed to the position system for that epoch. DoPHOT was run again at each epoch, but this time with the object list from the deep image as input, and also in a mode where the positions were not allowed to move (i.e., it was asserted that the position of the object is predetermined). This rather tedious process is very rewarding in terms of photometric reproducibility for the following reasons:

1. The object positions are better determined from the deep image, both because of better S/N, and because the

[2] The telescope delivers images with FWHM of 0".04. This is more than a factor of 2 smaller than the pixel size of the detector at 0".1 for the "Wide Field" chips 2, 3, and 4, and slightly smaller than the 0".05 pixel size for the "Planetary" chip 1.

[3] On exposures as long as those used here, about 5%–10% of the pixels on a chip are affected by cosmic rays. By combining two back to back exposures, even in an ideal process, 1% of the pixels will be affected by CRs on *both* subexposures.

co-addition of the images from various epochs is tantamount to co-adding "dithered" images: the unknown intrinsic subpixel profile of the PSF core in the deep image approaches a Gaussian, and DoPHOT is able to center stellar positions much better. This is particularly true for faint objects, where the wings are imperceptible in the individual epochs, and position determination is difficult to better than 0.2 pixels or so.

2. Since several hundred stars are used to derive the transformation (linear if position shift was within 3–4 pixels on the PC, cubic otherwise) from the deep image to the individual epochs, the systemic transformation is very well defined. The predicted positions of the objects from the deep list scatter by less than 0.07 pixel from the independently measured positions of the objects defining the systemic transformation.

3. The fitted brightness correlates with the fitted centroid position of the star. For such undersampled images, this can introduce scatter in the photometry merely due to uncertainty in centering, which, as mentioned above, is an acute problem for the faint stars. Thus by predetermining the positions as best as possible, the scatter in photometry from this source is minimized.

Thus for each image there is a fitted magnitude from DoPHOT, which gives the *relative* brightness of all the objects in that image. Actually, the PSF core varies slightly from one part of each CCD chip to another, and so the fitted magnitudes have a small positional dependence. In the following subsection we describe how to compensate for this and put all measurements on an internally consistent instrumental magnitude system. Note that the observations in F814W are treated identically: a separate and independent object list is obtained from the deep frame in that passband, and then processed as described above

3.2. *Tying to a Partial-Aperture Instrumental System.*

The PSF of stellar cores (within 2 pixels of star center in the wide field chips and within 4 pixels of the planetary camera chip PC1) is seen to vary slightly over the field of each CCD detector. This is believed to be an unavoidable effect from the re-imaging optics (Holtzman et al. 1995a). The effect is subtle, but definitely present. The low-level flared wings of the PSF outside the core is caused by microroughness of the primary mirror, or residual spherical aberration, and are *not noticeably variable* over the field area of the WFPC2. Thus aperture photometry with aperture radii of 5 pixels or larger are expected to be invariant over the field of the WFPC2. Such an aperture thus measures a constant fraction of a star's light, irrespective of where the star is placed in the field of a given CCD. Further, PSF changes from one epoch to another (if any) due to guiding jitter or focus changes, affect primarily the inner core of the stellar image, so such an aperture measure is stable against these changes. It is only time dependent then, to the extent of real sensitivity drifts in the detector. However, these magnitudes are not optimally extracted in S/N terms, and are severely vulnerable to object crowding.

The *fitted* magnitudes, which rely on the core of the PSF, *are* optimally extracted with respect to S/N considerations, and are also the best approach in the face of object crowding. By forcing a PSF that does not vary with field position, the fitted magnitudes are systematically mismeasured as a slowly varying function of position. The PSF variation is *not* sufficient to affect the object classification (which includes false object and cosmic-ray rejection) algorithms of DoPHOT. The photometric effect, which is really a field dependent aperture correction, is less than 0.15 mag peak to peak, and worst in the corners of each CCD field. By using bright isolated stars where the S/N is adequate for the aperture measurement, the field dependence in the fitted magnitude can be mapped as a slowly varying function of position on each CCD chip by comparing the aperture photometry with the fitted magnitudes. Denoting the fitted and partial aperture magnitude (described above) by $m_{\rm fit}$ and $m_{\rm ap}$ respectively, we can write (for any given chip and filter)

$$m_{\rm ap} = m_{\rm fit} + C + f(x, y)\,, \qquad (1)$$

where C is a constant, and $f(x, y)$ is a slowly varying function of chip position x, y that has value zero at the origin. A quadratic function in each of x and y is deemed adequate.

In principle, C and $f(x, y)$ should be evaluated for each image. However, this is impossible in practice, since to obtain a stable nondiverging solution for $f(x, y)$ many well-exposed and isolated stars are needed, and they must be scattered uniformly all over the field. We make the assumption that $f(x, y)$ is constant over time for the same chip and filter, while allowing C to be adjusted to account for changes in jitter and focus. In broad terms, this means that we assert that the core-to-halo ratio does not change for small changes in focus or jitter, and that changes in these can be absorbed by C as in the usual application of the aperture correction.

In order to derive $f(x, y)$, images of the dwarf spheroidal galaxy Leo I taken in the same filters and instrument configuration were examined. These images, which were taken as part of a different science program (Mateo et al. 1996), have hundreds of well-exposed isolated stars in each CCD chip area. As part of its process, DoPHOT reports aperture magnitudes (in this case we forced all apertures to be a 9×9 square) of the bright isolated objects that have a high signal-to-noise ratio. The equation above was fitted using reported $m_{\rm ap}$, $m_{\rm fit}$, x, and y values and using a bivariate quadratic polynomial for $f(x, y) + C$. Only stars with reported errors in fitted and aperture magnitudes of better than 0.05 mag (several hundred in each chip and filter) were used to map this function. The value of C and the coefficients of $f(x, y)$ were determined independently for each chip and filter.

In each chip area of the images of NGC 4536, DoPHOT is able to report $m_{\rm ap}$ for between 10 and 50 stars, where the reported errors in both fitted and aperture magnitude is less than 0.05 mag. Note that DoPHOT obtains aperture magnitudes in isolation, i.e., after neighboring objects have been subtracted. Using the coefficients in $f(x, y)$ derived from the Leo I data, one can use these values of $m_{\rm ap}$ to determine C appropriate to each individual image (and in each chip and filter). We find these determinations of C to be within 0.05 mag of those determined for the Leo I data, and similarly consistent from one epoch to another. This degree of consistency provides confidence in our assumptions. It also attests to the uniform quality of the images from the instrument and telescope, and to the lack of temporal drifts in sensitivity over the time span of observations.

Once C and $f(x, y)$ are known for any chip and filter, all the $m_{\rm fit}$ magnitudes can be converted to the system of $m_{\rm ap}$, where the effects from the field dependence of the PSF have been removed. We call these converted instrumental magni-

tudes m_{inst} which, as argued above, are expected to be invariant from one image to another except for real changes in instrument sensitivity. They combine maximum signal-to-noise ratio with systemic stability.

3.3. *Calibrating Instrumental to Standard Magnitudes*

The final part of the problem is to tie the instrumental magnitudes to a standard photometric system. The calibration from count rates to standard magnitudes for the *HST* WFPC2 has been done by Holtzman et al. (1995b). They give a prescription where first an instrumental magnitude is measured using an aperture of 0".5 on the sky. These are called "flight system" magnitudes, and are essentially just count rates. In their Table 6, they present transformations that tie these to "ground system" magnitudes, which are normalized so that "stars with zero color on the *UBVRI* system have zero color on the WFPC2 system." Note that the F555W and F814W ground system magnitudes defined by Holtzman et al. (1995b) are not defined the same way as by Harris et al. (1993). Magnitudes on the F555W and F814W system used in this paper refer to the ground system magnitudes as defined by Holtzman et al. (1995b). To transform to Johnson V and Kron-Cousins I magnitudes, the color equations given in Table 3 of Holtzman et al. (1995b) are to be used (cf. our eqs. [2] and [3] in § 4).

The m_{inst} system described in the previous subsection is similar, but not identical to the Holtzman flight magnitude system. The two systems differ by the size of the measuring aperture, and so by a constant offset in magnitude for each filter and each chip. This offset can be measured (separately and independently for each chip and filter) empirically, by comparing measurements made with Holtzman's prescription on bright isolated stars with m_{ap} or m_{inst}. This was done on the images of Leo I, and archive images of the globular clusters ω Cen and Pal 4. The derived differences are very robust (to better than 0.01 mag). This allows us to tie the m_{inst} values to the F555W and F814W ground systems and so to V and I as explained above.

In practice, rather than converting m_{inst} to the standard system for each epoch individually, only one selected epoch (where the scatter in fitting equation [1] is smallest) is converted. The values of m_{inst} for the remaining epochs are then offset by a constant such that the ensemble average of thousands of the relatively brighter stars are zeroed against the standard magnitudes of the corresponding stars of the selected epoch. Had there been a sensitivity drift with epoch, this procedure would have taken it out, as long as the calibrations for the "selected" epoch were well established. However, as it happens, sensitivity drift is not a problem in the data used here, but we followed the procedure as a matter of consistent practice.

Geometrical distortions in the field can lead to uncorrected position-dependent effects in the photometry at the 0.02 magnitude level. The charge transfer problem can lead to systematic errors in the photometry as a function of the position of a star in a given CCD chip. Charge transfer inefficiency will have a stronger effect when the charge must be passed through a large number of pixels before being read off. For the WFPC2 with chips operating at $-88°$ C, the effect is that the stars are measured systematically fainter with increase in the y coordinate of the CCD chips by up to 0.05 mags (Holtzman et al. 1995b) peak to peak. The procedure we follow does not correct explicitly for these effects, but is adjusted to be correct *in the mean*. So individual stars may have position-dependent systematic errors of up to 0.025 mag—amounts that are not significant (for our goals) at the star by star level. We have assumed in the above that the flat fields have been cross-normalized across the various chips so that the photometry of stars through an aperture comes out correct. Although this is not *strictly* the case, the effective errors from this assumption are smaller than from geometrical distortions within each chip (Holtzman et al. 1995a; Holtzman 1995). Thus peak to peak position-dependent effects over the entire WFPC2 field should be within 0.05 mag, with rms value less than 0.02 mag.

There is an additional issue with the photometric zero-points that has been seen, but is not well understood at the time of writing of this paper. The effect, which was first noticed by Peter Stetson (1995), is that observations with exposures over a thousand seconds long have a higher count rate in the stars than on exposures that are less than a hundred seconds long. This was noticed while comparing exposures of different duration of identical fields in the globular clusters Pal 4 and NGC 2419. By comparing to ground based photometry of stars in these objects, Stetson found that the "short" exposures are in accordance with the Holtzman et al. (1995b) calibration, but that the "long" exposures result in magnitudes that are too bright by 0.05 mag (in both F555W and F814W) if the Holtzman et al. (1995b) calibration is used. This is consistent with the fact that the data used by Holtzman et al. (1995b) are "short" exposures, few tens of seconds long. Stetson kindly made the data on Pal 4 and NGC 2419 available to us. The anomaly he finds has been independently confirmed using the DoPHOT-based reduction procedure.

Unfortunately the data necessary to explore this further are not available at this time, and a more complete evaluation of this "effect" is not possible. If this is a nonlinearity problem, the effect is at the 0.015 mag per mag level. If it has to do with charge transfer related effects, the effect may be more complicated. Under the circumstances the best we can do is present the photometry on the basis of the Holtzman et al. (1995b) calibration. Since all our observations have exposure times that are "long," the adjustment by 0.05 mag is made in § 6. This step may require revision once a better understanding and quantification of this "long versus short exposure" effect is well understood. Therefore, we have chosen to apply it only as a final step rather than propagate it all the way through, so that future adjustment can be done easily.

4. IDENTIFICATION AND CLASSIFICATION OF THE VARIABLE STARS

Armed with measured magnitudes and reported errors at all available epochs for each star in the object list, the method described in Saha & Hoessel (1990) was used to identify variable stars. In essence it uses a χ^2 test for variability followed by a "periodicity" test based on the Lafler & Kinman (1965) algorithm using the Λ statistic (as implemented in Saha & Hoessel 1990). All objects with $\chi^2 \geq 10$ were visually examined on the images, whether or not they appear periodic. All objects which have a formal χ^2 probability greater than 0.999 of being variable, and $\Lambda \geq 3.0$ were also examined visually. Visual confirmation of variability was mandatory for inclusion in the final list of variables. This is still the most efficacious way of eliminating

specious detections due to variable "warm" pixels (they are pixels that wander in value over time; unlike "hot" pixels that take on saturated values and do not change, warm pixels come and go, and can be mistaken for variable stars), extreme blending of objects, or unremoved cosmic-ray hits. This inspection procedure of all candidate variables was performed independently by several of us.

The photometry for the final list of 106 variable stars is presented in Table 2, for each epoch and in each filter. The objects are identified in Figure 2 (Plates 2–5).

The periods were determined with the Lafler-Kinman algorithm (1965), using the F555W passband data only. Aliasing is not a serious problem for periods between 10 and 67 days, since the observing strategy incorporated a timing scheme between epochs that minimizes aliasing problems (Saha 1996). The resulting light curves in the F555W passband, along with periods and mean magnitudes (phase-weighted intensity average, as in Saha & Hoessel 1990) are shown in Figure 3 in descending order of period. Note that the period of 80 days of object C2-V32 is a guess,

TABLE 2

PHOTOMETRY OF VARIABLE STARS: MAGNITUDES AND ERROR ESTIMATES

HJD	C1-V1	C1-V2	C1-V3	C1-V4	C1-V5	C1-V6	C1-V7	C1-V8
				F555W				
2449506.8003	—	26.63 0.15	25.85 0.08	26.55 0.16	25.18 0.05	25.53 0.07	27.07 0.25	—
2449520.6803	27.45 0.34	25.67 0.08	26.44 0.15	26.38 0.13	25.98 0.08	26.07 0.11	—	27.83 0.47
2449521.9545	27.59 0.31	25.67 0.06	26.64 0.14	26.33 0.12	26.13 0.10	26.08 0.11	28.17 0.44	27.34 0.30
2449526.6457	27.60 0.31	25.68 0.06	26.65 0.14	26.34 0.12	26.14 0.10	26.09 0.11	28.18 0.44	27.35 0.30
2449528.6559	27.80 0.50	26.21 0.09	26.43 0.16	26.35 0.15	26.16 0.09	26.41 0.15	26.63 0.13	27.08 0.22
2449531.8730	26.90 0.21	26.42 0.12	25.89 0.08	25.81 0.08	26.33 0.13	26.24 0.16	27.15 0.21	27.63 0.32
2449533.4145	26.46 0.16	26.40 0.12	25.61 0.08	25.81 0.07	26.55 0.12	25.91 0.09	27.21 0.22	27.80 0.42
2449536.7662	26.84 0.23	26.66 0.16	25.86 0.10	26.05 0.09	25.69 0.07	25.75 0.08	27.81 0.38	27.41 0.27
2449545.9501	26.97 0.24	25.50 0.08	26.15 0.13	26.21 0.13	25.53 0.06	26.00 0.08	26.98 0.17	26.88 0.19
2449550.9774	27.45 0.35	25.99 0.12	26.43 0.17	26.55 0.17	25.80 0.10	26.34 0.14	27.59 0.43	27.03 0.27
2449559.8912	27.45 0.34	26.89 0.23	26.41 0.13	26.05 0.11	26.15 0.13	26.47 0.14	26.63 0.13	27.42 0.38
2449562.9742	27.64 0.41	26.95 0.36	25.70 0.10	26.35 0.13	26.39 0.11	26.51 0.15	26.99 0.17	—
2449564.6463	27.33 0.34	26.69 0.21	25.58 0.08	26.26 0.11	26.45 0.11	26.55 0.14	27.16 0.22	27.68 0.41
2449566.6607	—	26.51 0.16	25.80 0.11	26.35 0.14	26.08 0.14	25.72 0.08	27.74 0.41	27.95 0.44
2449569.6105	—	25.69 0.10	25.92 0.12	26.76 0.22	25.36 0.07	25.06 0.07	27.60 0.37	27.68 0.42
2449571.7555	27.21 0.42	25.45 0.08	25.99 0.13	26.18 0.16	25.02 0.05	25.38 0.07	27.09 0.27	26.26 0.19
2449573.6998	27.19 0.31	25.88 0.10	26.02 0.09	25.69 0.08	25.25 0.07	0.00 0.00	26.38 0.16	26.80 0.31
				F814W				
2449520.8115	26.02 0.32	—	25.08 0.12	25.53 0.18	24.65 0.07	24.69 0.12	26.08 0.30	—
2449532.0042	25.47 0.17	—	24.80 0.09	24.98 0.12	25.25 0.15	24.83 0.10	25.65 0.15	—
2449546.0806	25.72 0.22	24.47 0.10	25.35 0.17	—	24.50 0.08	24.40 0.10	25.60 0.15	—
2449560.0217	25.64 0.22	24.96 0.13	25.26 0.17	25.27 0.19	24.83 0.09	24.68 0.08	25.68 0.15	—
2449564.7803	25.80 0.28	—	24.75 0.12	25.58 0.18	24.85 0.11	24.88 0.11	25.70 0.19	—

HJD	C1-V9	C1-V10	C2-V1	C2-V2	C2-V3	C2-V4	C2-V5	C2-V6
				F555W				
2449506.8003	27.23 0.22	25.28 0.06	26.25 0.14	28.00 0.56	26.18 0.11	26.33 0.17	25.41 0.10	26.08 0.13
2449520.6803	27.49 0.31	25.88 0.08	26.14 0.12	28.61 0.94	25.47 0.06	25.38 0.08	25.53 0.10	26.65 0.19
2449521.9545	—	25.76 0.06	25.93 0.12	27.57 0.39	26.13 0.11	25.83 0.13	25.56 0.10	26.41 0.18
2449526.6457	—	25.77 0.06	26.45 0.15	27.07 0.26	26.69 0.16	25.88 0.14	25.83 0.12	25.47 0.08
2449528.6559	27.82 0.44	26.23 0.11	26.71 0.18	27.45 0.39	26.38 0.16	26.01 0.13	25.90 0.13	25.89 0.09
2449531.8730	26.91 0.21	25.81 0.09	26.71 0.22	27.80 0.49	26.61 0.21	26.25 0.15	25.90 0.14	25.71 0.09
2449533.4145	27.73 0.39	25.13 0.05	26.18 0.11	28.07 0.58	26.60 0.19	26.66 0.21	25.65 0.11	25.82 0.09
2449536.7662	27.05 0.22	24.80 0.04	25.82 0.09	26.41 0.18	25.55 0.07	26.61 0.20	25.39 0.09	25.98 0.09
2449545.9501	27.44 0.26	25.16 0.06	26.63 0.18	27.89 0.56	26.83 0.21	25.35 0.08	25.35 0.09	26.85 0.28
2449550.9774	27.77 0.31	25.48 0.07	26.19 0.14	—	26.55 0.18	25.67 0.08	25.58 0.11	25.88 0.10
2449559.8912	27.17 0.26	25.90 0.09	26.41 0.17	26.69 0.21	26.23 0.14	26.41 0.18	25.91 0.12	26.14 0.12
2449562.9742	27.74 0.37	25.85 0.07	25.93 0.14	27.57 0.41	26.46 0.22	26.55 0.22	25.80 0.13	26.02 0.14
2449564.6463	26.56 0.17	26.07 0.10	26.08 0.12	—	26.28 0.17	26.31 0.18	26.08 0.15	26.19 0.16
2449566.6607	27.81 0.47	25.98 0.10	26.47 0.18	27.78 0.61	26.61 0.24	26.85 0.34	25.40 0.10	26.41 0.18
2449569.6105	27.16 0.24	25.88 0.12	26.32 0.17	—	26.83 0.26	26.63 0.29	25.27 0.10	26.49 0.18
2449571.7555	27.39 0.31	25.05 0.05	—	27.59 0.56	25.60 0.11	25.07 0.07	25.32 0.09	26.53 0.19
2449573.6998	27.68 0.42	24.90 0.05	26.53 0.22	26.99 0.35	25.85 0.10	25.32 0.10	25.38 0.09	26.73 0.29
				F814W				
2449520.8115	26.61 0.41	24.61 0.09	25.39 0.14	—	24.68 0.11	25.00 0.13	24.66 0.10	25.68 0.19
2449532.0042	26.84 0.44	24.65 0.08	25.85 0.19	—	25.18 0.12	25.09 0.15	25.22 0.13	25.14 0.20
2449546.0806	25.86 0.22	24.22 0.05	26.11 0.28	—	25.24 0.18	24.65 0.09	24.84 0.09	26.24 0.29
2449560.0217	26.64 0.41	24.55 0.10	25.96 0.23	—	25.08 0.12	25.06 0.13	25.23 0.16	25.22 0.17
2449564.7803	26.48 0.41	24.67 0.10	25.24 0.13	—	25.33 0.14	25.71 0.22	24.86 0.12	25.56 0.21

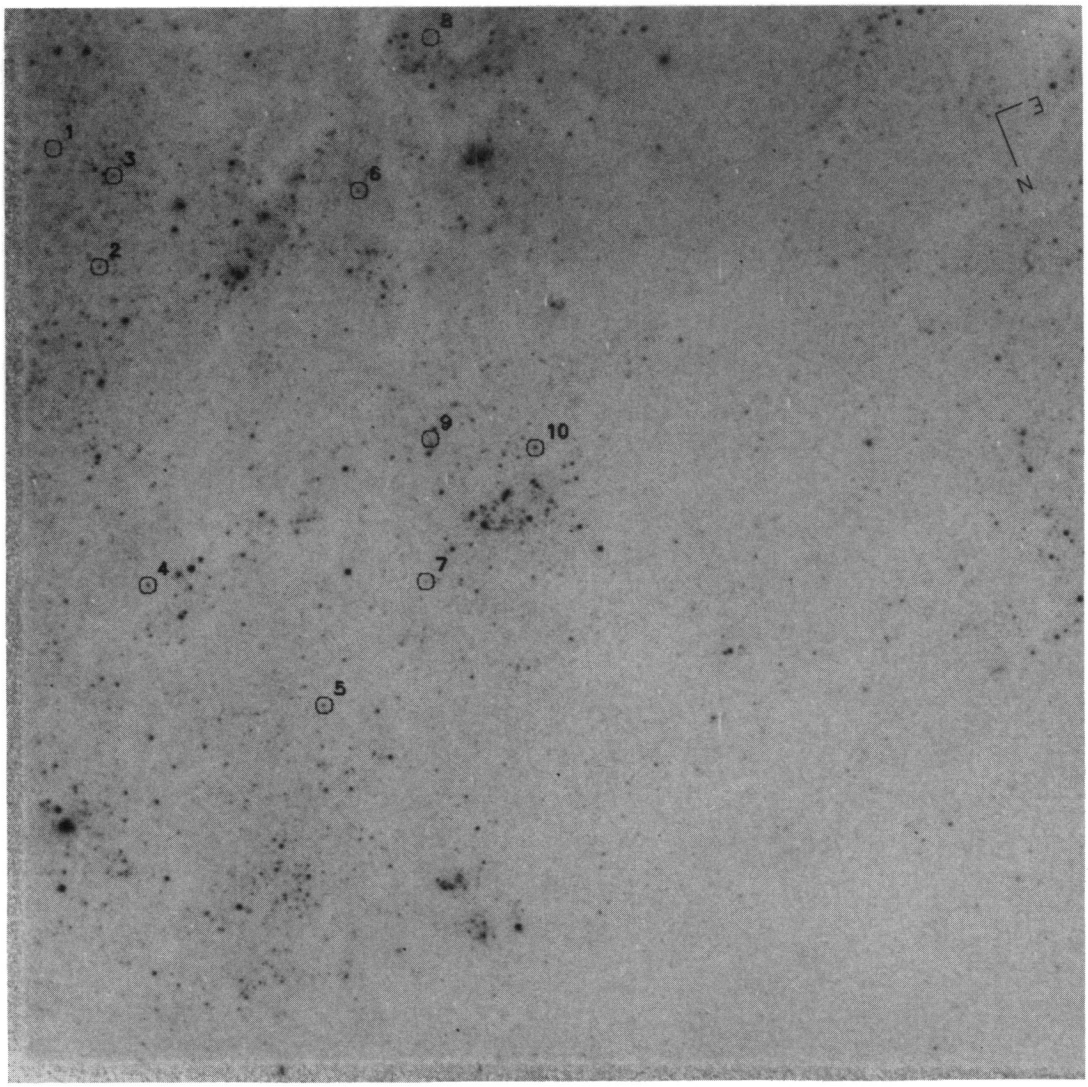

FIG. 2a

FIG. 2.—Finding charts for the variables found with *HST* in the northwest arm of NGC 4536. Variables are numbered according to the CCD chip number, followed by the variable number within that chip. An example is C1-V1 for variable number 1 on Chip 1. Figures 2*a*, 2*b*, 2*c*, and 2*d* here refer to Chips 1, 2, 3, and 4 respectively. Orientation on the sky is shown for each chip area. See Fig. 9 for a composite of the four chips.

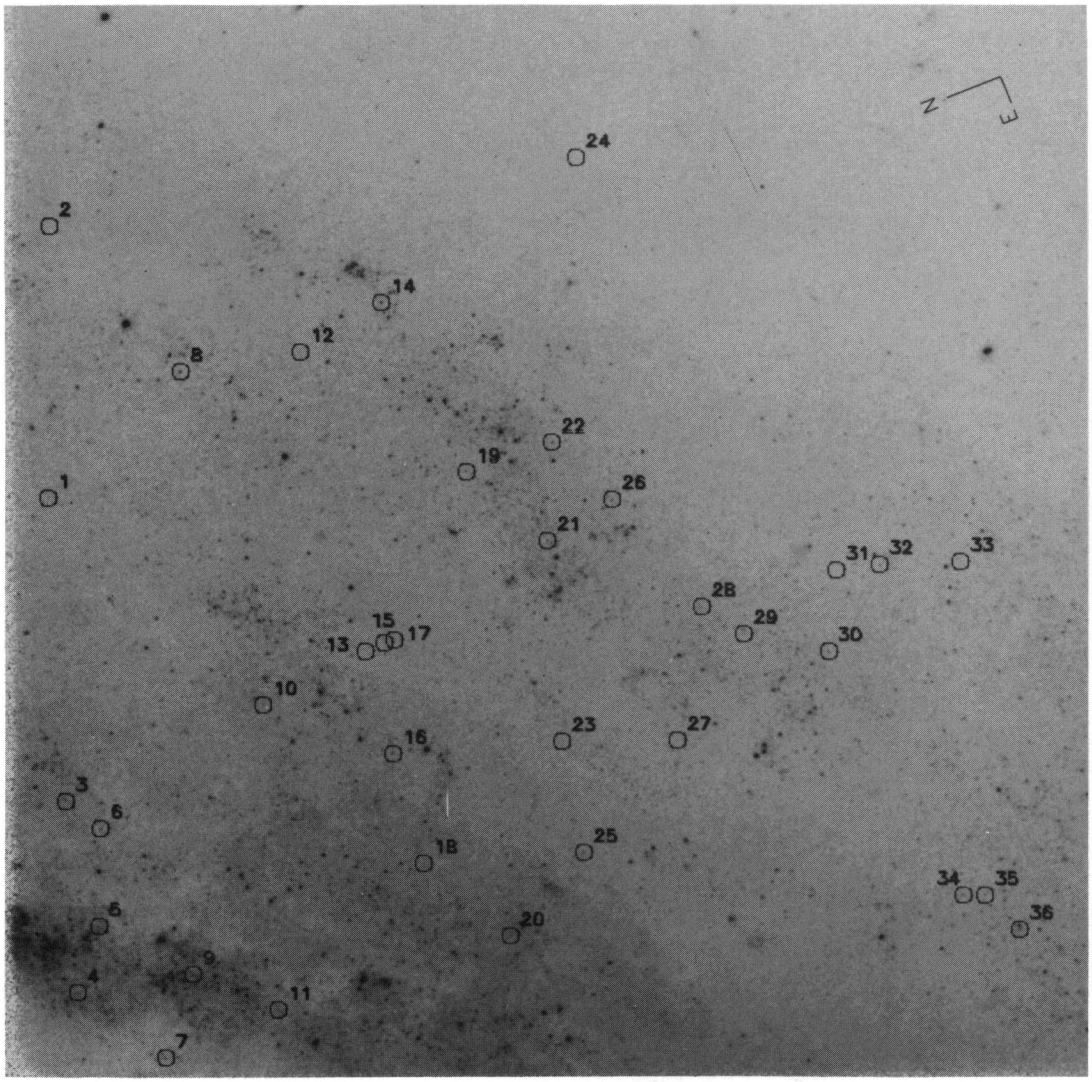

FIG. 2*b*

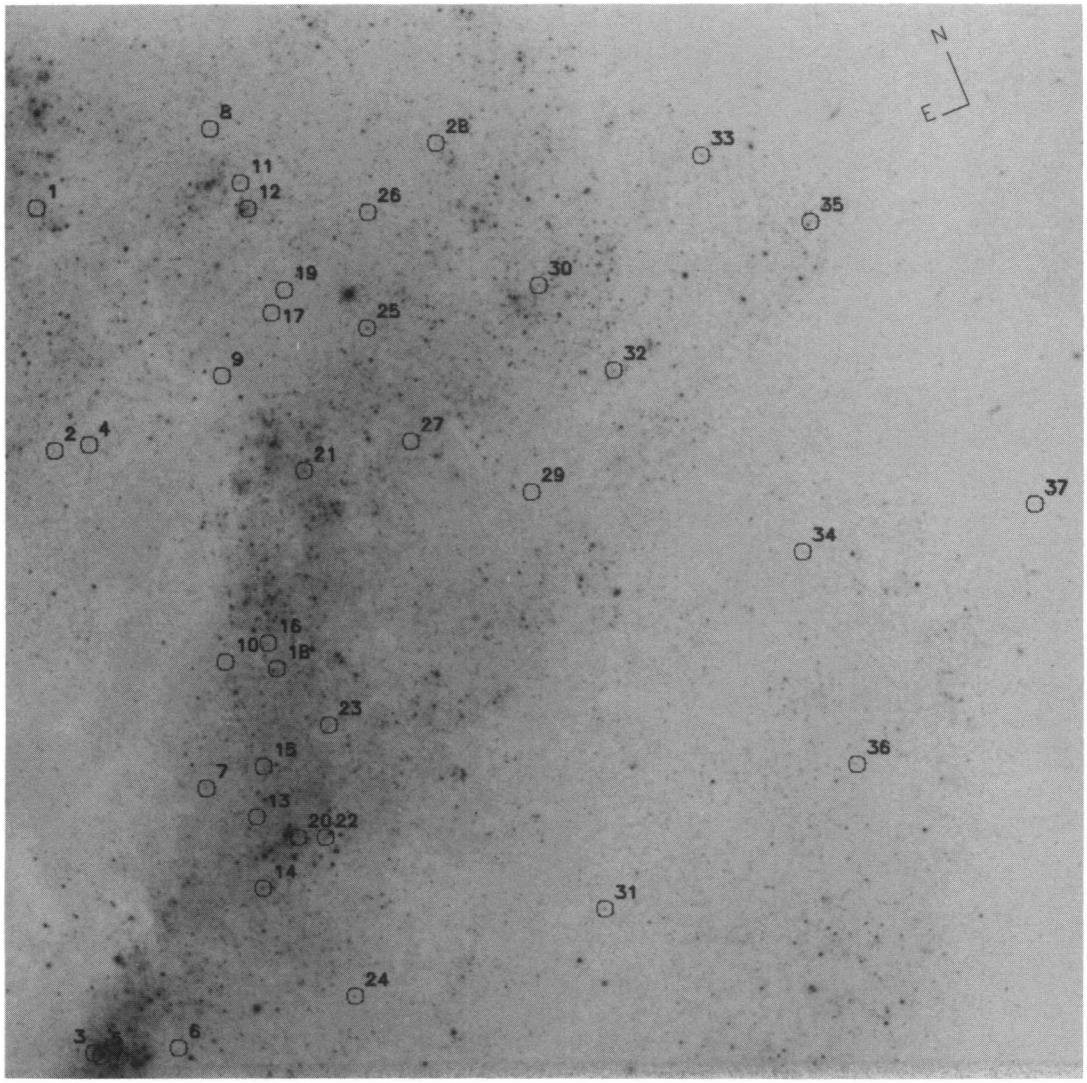

FIG. 2*c*

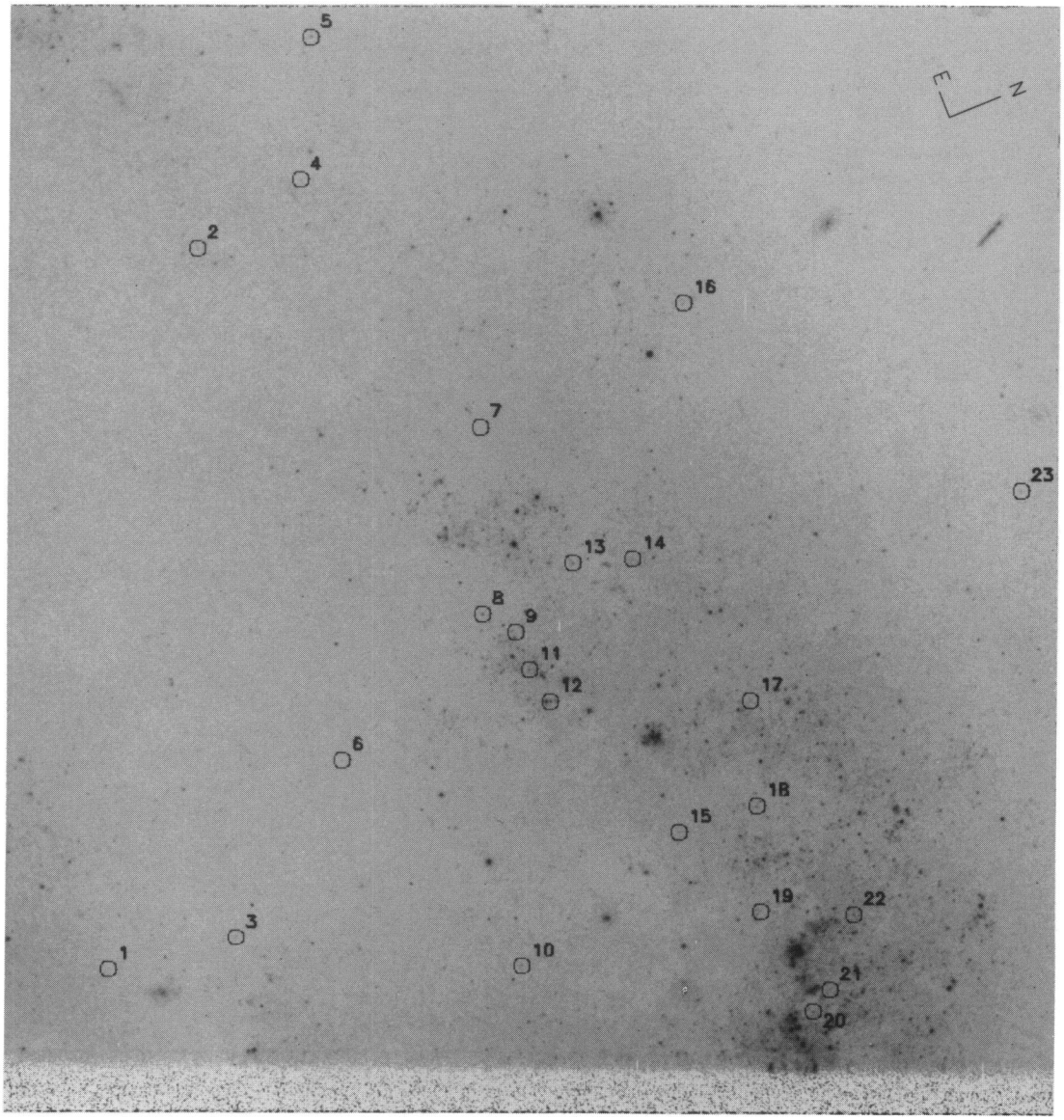

FIG. 2*d*

SAHA et al. (see 466, 60)

TABLE 2—*Continued*

HJD	C2-V7	C2-V8	C2-V9	C2-V10	C2-V11	C2-V12	C2-V13	C2-V14
				F555W				
2449506.8003	25.84 0.13	24.96 0.05	25.65 0.11	26.58 0.14	26.06 0.10	27.28 0.25	—	25.73 0.08
2449520.6803	25.94 0.16	25.39 0.06	25.64 0.12	26.06 0.11	25.97 0.13	26.89 0.21	—	24.72 0.04
2449521.9545	25.36 0.09	25.30 0.06	25.78 0.13	26.42 0.14	26.23 0.10	26.51 0.17	27.68 0.40	24.75 0.04
2449526.6457	25.35 0.09	25.31 0.06	25.60 0.12	26.98 0.21	26.34 0.15	27.09 0.28	27.43 0.37	24.98 0.06
2449528.6559	25.38 0.08	25.11 0.06	25.55 0.11	27.80 0.60	26.55 0.16	26.45 0.13	28.30 0.69	24.77 0.04
2449531.8730	25.41 0.10	24.67 0.04	25.08 0.08	26.67 0.21	26.44 0.16	26.96 0.23	27.03 0.25	24.97 0.05
2449533.4145	25.67 0.12	24.43 0.03	24.98 0.08	26.45 0.13	26.51 0.29	27.45 0.31	28.05 0.58	25.28 0.07
2449536.7662	25.63 0.11	24.33 0.04	25.06 0.08	26.10 0.12	25.88 0.08	26.86 0.18	27.27 0.29	25.06 0.05
2449545.9501	25.72 0.12	24.45 0.04	25.24 0.09	27.00 0.24	26.71 0.24	26.61 0.14	—	25.21 0.05
2449550.9774	26.39 0.21	24.61 0.04	25.22 0.08	26.35 0.14	26.11 0.12	27.24 0.32	28.23 0.77	25.88 0.13
2449559.8912	26.33 0.21	24.81 0.04	25.68 0.13	26.13 0.18	26.98 0.32	27.30 0.42	27.56 0.46	25.60 0.07
2449562.9742	25.50 0.11	24.63 0.04	25.61 0.14	27.71 0.64	26.56 0.23	27.06 0.30	28.07 0.78	25.53 0.08
2449564.6463	25.35 0.10	24.99 0.05	25.63 0.13	27.09 0.32	25.74 0.12	26.80 0.24	28.26 0.82	25.45 0.06
2449566.6607	25.28 0.10	24.94 0.06	25.82 0.20	27.22 0.40	25.93 0.12	26.67 0.18	26.64 0.22	25.18 0.06
2449569.6105	25.59 0.14	25.14 0.06	25.63 0.14	26.17 0.16	26.18 0.17	26.85 0.21	28.39 0.95	24.74 0.04
2449571.7555	25.67 0.13	25.14 0.06	25.89 0.18	26.02 0.16	26.40 0.21	26.91 0.28	27.53 0.56	24.72 0.05
2449573.6998	25.41 0.12	25.21 0.08	25.89 0.17	26.47 0.20	27.03 0.43	26.45 0.17	—	24.81 0.05
				F814W				
2449520.8115	—	24.13 0.05	24.77 0.12	25.50 0.17	24.77 0.10	25.98 0.19	26.66 0.41	23.86 0.06
2449532.0042	—	23.83 0.05	24.21 0.06	25.90 0.25	25.03 0.14	26.26 0.30	26.43 0.39	23.99 0.05
2449546.0806	—	23.67 0.05	24.28 0.07	25.73 0.22	25.19 0.13	26.42 0.36	26.69 0.35	24.13 0.05
2449560.0217	—	23.86 0.05	24.66 0.10	25.96 0.27	25.28 0.17	26.07 0.31	26.55 0.43	24.85 0.12
2449564.7803	—	23.93 0.05	24.42 0.20	26.05 0.28	24.95 0.12	25.89 0.25	25.84 0.26	24.68 0.13

HJD	C2-V15	C2-V16	C2-V17	C2-V18	C2-V19	C2-V20	C2-V21	C2-V22
				F555W				
2449506.8003	27.48 0.35	25.57 0.07	28.40 0.77	26.63 0.22	25.82 0.09	25.51 0.09	26.80 0.26	25.39 0.07
2449520.6803	28.66 0.94	25.07 0.06	26.59 0.19	26.71 0.20	25.56 0.06	27.70 0.45	26.30 0.14	26.05 0.10
2449521.9545	27.25 0.28	25.02 0.06	26.99 0.25	26.39 0.14	25.72 0.07	26.84 0.21	26.80 0.21	26.01 0.10
2449526.6457	28.07 0.63	25.09 0.05	28.02 0.54	26.77 0.19	26.05 0.11	26.83 0.25	26.43 0.12	25.99 0.09
2449528.6559	26.72 0.19	25.18 0.06	27.36 0.25	26.69 0.19	26.03 0.11	25.63 0.10	25.76 0.11	26.14 0.13
2449531.8730	28.31 0.70	25.27 0.07	—	26.11 0.11	26.38 0.15	—	25.65 0.08	25.63 0.07
2449533.4145	26.63 0.28	25.30 0.06	27.80 0.55	26.07 0.12	26.42 0.13	25.75 0.09	25.72 0.08	25.57 0.07
2449536.7662	28.03 0.59	25.75 0.16	27.57 0.38	26.34 0.15	26.44 0.14	26.38 0.15	26.05 0.10	25.25 0.08
2449545.9501	28.16 0.64	25.67 0.09	28.41 0.85	25.99 0.14	26.11 0.12	26.93 0.25	26.27 0.14	25.33 0.07
2449550.9774	27.48 0.45	25.39 0.10	28.27 0.71	26.38 0.15	26.28 0.16	25.57 0.09	25.88 0.12	25.44 0.07
2449559.8912	27.99 0.74	25.13 0.08	28.18 0.73	26.01 0.11	25.21 0.08	26.76 0.25	26.18 0.12	26.40 0.24
2449562.9742	28.13 0.69	25.13 0.11	27.63 0.48	26.39 0.15	25.81 0.13	26.84 0.30	26.28 0.15	25.95 0.13
2449564.6463	28.38 0.89	25.20 0.06	28.13 0.61	26.49 0.26	25.94 0.13	26.97 0.30	26.42 0.19	26.03 0.10
2449566.6607	27.45 0.47	25.46 0.16	—	26.81 0.34	26.02 0.12	27.18 0.37	25.40 0.08	26.28 0.16
2449569.6105	27.86 0.80	25.39 0.08	27.28 0.37	26.65 0.20	26.31 0.16	26.09 0.15	25.61 0.10	26.23 0.14
2449571.7555	27.83 0.65	25.66 0.11	27.80 0.78	26.60 0.21	26.58 0.26	25.55 0.11	25.97 0.13	26.15 0.13
2449573.6998	27.48 0.42	25.61 0.12	27.36 0.49	26.31 0.21	26.46 0.20	25.85 0.13	26.30 0.22	25.88 0.14
				F814W				
2449520.8115	—	24.26 0.07	—	25.64 0.19	24.67 0.07	25.57 0.17	25.56 0.15	25.24 0.16
2449532.0042	25.99 0.26	24.30 0.06	—	25.53 0.15	25.25 0.13	25.01 0.10	25.28 0.11	25.43 0.18
2449546.0806	—	24.67 0.07	—	24.93 0.17	25.03 0.11	25.92 0.22	25.96 0.24	24.58 0.09
2449560.0217	—	24.31 0.07	—	25.52 0.16	24.77 0.08	25.32 0.17	26.08 0.22	24.84 0.11
2449564.7803	—	24.48 0.08	—	25.72 0.22	25.13 0.15	26.15 0.34	26.09 0.24	25.06 0.12

since the total observing span cannot fully cover periods in excess of 67 days. An inspection of Figure 3 shows that only a small fraction of the objects have light curves that are inconsistent with that of a Cephied variable.

The available data for variables in F814W were then folded with the ephemerides derived above using the F555W data. The mean magnitudes in F814W were then obtained, also using the individual F814W measurements and the ephemerides from the F555W observations, using the procedure of Labhardt, Sandage, & Tammann (1996) to convert F814W magnitudes at randomly sampled phases to ⟨F814W⟩ using magnitude amplitude and phase information from the more complete F555W light curves. Note that each available observation in F814W can be used independently to derive a mean magnitude, so the scatter of these values is an external measure of the uncertainty in determining ⟨F814W⟩. However, with only at most five epochs in F814W, the ⟨F814W⟩ values are generally more uncertain than the ⟨F555W⟩ values.

The light curves in F814W are shown in Figure 4 for all objects where at least one measurement in F814W is available. Since there are at most 5 measured epochs for any star

TABLE 2—*Continued*

HJD	C2-V23	C2-V24	C2-V25	C2-V26	C2-V27	C2-V28	C2-V29	C2-V30
				F555W				
2449506.8003	27.30 0.31	28.03 0.49	25.73 0.09	25.67 0.09	27.91 0.44	27.52 0.38	26.77 0.18	25.35 0.07
2449520.6803	27.38 0.37	27.94 0.48	25.69 0.07	25.39 0.06	28.44 0.72	27.22 0.26	26.32 0.13	25.86 0.11
2449521.9545	28.25 0.67	28.49 0.74	25.80 0.08	25.55 0.07	28.75 0.94	26.88 0.21	26.20 0.12	26.18 0.10
2449526.6457	27.39 0.38	28.43 0.60	26.22 0.13	25.74 0.06	27.96 0.54	27.63 0.42	26.44 0.13	26.16 0.12
2449528.6559	27.61 0.44	27.77 0.37	26.23 0.11	25.89 0.10	27.61 0.32	27.63 0.36	26.63 0.14	25.74 0.11
2449531.8730	27.17 0.34	27.18 0.22	26.32 0.13	26.10 0.13	—	26.75 0.20	26.53 0.14	25.92 0.10
2449533.4145	27.85 0.47	26.80 0.18	26.22 0.14	26.32 0.13	—	26.78 0.21	26.75 0.19	25.55 0.08
2449536.7662	26.55 0.20	27.46 0.34	25.59 0.08	26.38 0.13	27.49 0.37	27.13 0.27	26.42 0.13	25.33 0.09
2449545.9501	27.83 0.56	28.23 0.58	26.32 0.14	25.80 0.09	27.27 0.31	27.51 0.39	25.83 0.11	25.75 0.11
2449550.9774	28.30 0.75	28.50 0.77	25.61 0.12	26.30 0.14	27.10 0.24	27.08 0.29	26.25 0.12	25.93 0.12
2449559.8912	27.38 0.38	28.40 0.73	26.71 0.23	25.32 0.09	27.70 0.47	27.61 0.50	26.75 0.16	26.33 0.15
2449562.9742	27.81 0.57	28.45 0.80	26.26 0.17	25.43 0.07	26.53 0.17	27.71 0.50	26.76 0.17	26.09 0.14
2449564.6463	26.83 0.28	—	25.86 0.11	25.59 0.09	—	27.15 0.27	27.23 0.23	25.41 0.08
2449566.6607	—	—	25.80 0.12	26.00 0.12	—	26.09 0.13	26.74 0.21	25.32 0.07
2449569.6105	28.09 0.67	—	26.10 0.16	26.06 0.13	28.19 0.90	27.01 0.29	25.63 0.12	25.55 0.10
2449571.7555	27.20 0.48	—	26.15 0.14	26.22 0.17	27.90 0.84	27.40 0.44	25.63 0.10	25.69 0.11
2449573.6998	27.71 0.71	27.38 0.45	26.75 0.24	26.55 0.17	—	27.41 0.41	25.72 0.12	25.76 0.12
				F814W				
2449520.8115	25.86 0.22	26.46 0.24	—	25.20 0.13	26.65 0.40	25.65 0.18	25.16 0.12	25.05 0.09
2449532.0042	25.91 0.21	26.97 0.46	25.19 0.16	25.34 0.11	27.02 0.58	25.46 0.14	25.57 0.16	24.95 0.09
2449546.0806	25.81 0.22	27.17 0.54	25.82 0.20	25.19 0.11	27.30 0.90	25.53 0.17	24.95 0.10	24.77 0.08
2449560.0217	26.25 0.31	26.42 0.34	25.50 0.18	25.02 0.09	26.80 0.50	25.67 0.18	25.99 0.38	25.19 0.13
2449564.7803	26.09 0.25	26.58 0.46	25.22 0.17	24.93 0.10	27.05 0.69	25.76 0.26	25.92 0.16	24.76 0.09

HJD	C2-V31	C3-V32	C2-V33	C2-V34	C2-V35	C2-V36	C3-V1	C3-V2
				F555W				
2449506.8003	28.23 0.63	25.76 0.08	28.01 0.52	25.69 0.09	25.48 0.07	25.43 0.07	26.30 0.13	26.31 0.14
2449520.6803	27.42 0.38	25.89 0.09	26.67 0.20	26.23 0.13	26.44 0.16	25.84 0.09	26.05 0.10	25.83 0.09
2449521.9545	28.25 0.74	25.94 0.09	26.64 0.17	26.44 0.15	26.47 0.15	25.46 0.08	25.93 0.09	25.98 0.11
2449526.6457	—	26.10 0.09	27.64 0.38	26.65 0.21	26.50 0.15	24.77 0.06	26.63 0.18	26.59 0.15
2449528.6559	27.08 0.24	26.05 0.14	28.07 0.60	25.72 0.09	27.02 0.48	24.83 0.05	26.63 0.19	26.57 0.18
2449531.8730	28.73 0.81	26.09 0.09	27.46 0.35	25.34 0.08	26.30 0.16	24.92 0.06	26.30 0.16	27.27 0.31
2449533.4145	28.64 0.88	25.97 0.09	28.05 0.63	25.53 0.08	26.70 0.19	25.05 0.06	26.10 0.11	27.01 0.26
2449536.7662	27.78 0.41	26.01 0.09	26.94 0.20	25.97 0.16	26.18 0.14	25.07 0.07	25.74 0.10	25.73 0.08
2449545.9501	27.11 0.29	26.43 0.20	28.24 0.69	26.23 0.13	26.18 0.14	25.63 0.07	26.60 0.19	27.46 0.26
2449550.9774	27.91 0.61	26.09 0.10	27.50 0.38	26.61 0.22	26.11 0.12	25.89 0.10	26.55 0.19	27.03 0.25
2449559.8912	27.84 0.51	26.00 0.11	27.74 0.40	25.38 0.10	26.51 0.21	24.77 0.05	26.48 0.18	26.75 0.15
2449562.9742	26.94 0.21	25.97 0.13	27.00 0.27	25.31 0.08	26.63 0.28	24.73 0.06	26.73 0.23	27.28 0.31
2449564.6463	27.82 0.41	25.80 0.09	27.57 0.38	25.53 0.10	26.39 0.19	25.03 0.07	26.64 0.21	26.78 0.21
2449566.6607	28.20 0.83	25.72 0.10	—	—	26.94 0.36	24.93 0.05	26.36 0.16	26.63 0.16
2449569.6105	27.36 0.38	25.69 0.09	27.55 0.41	26.13 0.17	26.44 0.19	25.26 0.07	26.10 0.14	26.17 0.14
2449571.7555	—	25.75 0.10	27.71 0.65	26.09 0.16	26.01 0.13	25.13 0.09	25.95 0.14	26.45 0.21
2449573.6998	—	25.59 0.10	26.74 0.21	25.75 0.11	25.91 0.13	25.31 0.07	26.02 0.14	26.72 0.25
				F814W				
2449520.8115	—	24.83 0.09	26.57 0.49	25.28 0.14	25.16 0.14	24.69 0.21	25.35 0.14	25.01 0.12
2449532.0042	—	25.27 0.11	26.06 0.27	24.80 0.09	24.99 0.13	24.39 0.08	25.47 0.19	25.64 0.22
2449546.0806	—	25.33 0.11	26.11 0.27	25.05 0.11	25.23 0.15	24.80 0.10	25.56 0.23	25.65 0.20
2449560.0217	—	25.05 0.09	26.74 0.40	24.99 0.11	25.19 0.16	24.53 0.09	25.66 0.20	25.46 0.17
2449564.7803	—	24.98 0.10	26.70 0.50	24.83 0.08	25.47 0.18	24.55 0.09	25.63 0.19	25.94 0.27

in this passband, the figures are sketchy at best. In the most encouraging cases, the characteristic shape of a Cepheid's light curve is recovered, and the F814W observations are also in phase with the one from F555W. In some cases the observations in F814W sample the phase very poorly, and no definite conclusion is possible. There are also clear cases where F814W data are out of phase with the F555W light curve, or show little if any variation, even through the critical phases. This last can happen for two main reasons: (1) the object is not a Cepheid even though its F555W light curve looks like it is, and/or (2) crowding problems have led to confusion noise, particularly severe in the redder passband.

From visual inspection of the light curves, a quality index was assigned to each putative Cepheid in the range 0 to 6 based on: (1) the quality of the F555W light curve (2 points), (2) the phase coverage of the F814W observations, given the derived period (2 points), and (3) the amplitude and phase coherence of the F814W observations compared to the F555W light curve (3 points). Thus an object with quality index 6 is a perfect example of what is considered a Cepheid on the basis of its light curves in both passbands, whereas a

TABLE 2—*Continued*

HJD	C3-V3	C3-V4	C3-V5	C3-V6	C3-V7	C3-V8	C3-V9	C3-V10
				F555W				
2449506.8003	24.85 0.12	26.88 0.21	24.49 0.10	27.30 0.41	26.05 0.11	26.57 0.16	27.38 0.32	27.60 0.38
2449520.6803	24.46 0.10	26.52 0.18	24.13 0.08	27.50 0.47	25.39 0.06	26.57 0.17	26.90 0.25	27.13 0.34
2449521.9545	24.55 0.11	26.70 0.18	24.28 0.08	28.32 0.81	25.66 0.09	26.38 0.13	27.38 0.31	27.46 0.43
2449526.6457	24.77 0.13	26.84 0.17	24.13 0.08	26.95 0.25	25.85 0.09	25.98 0.10	26.64 0.18	27.69 0.46
2449528.6559	24.73 0.13	27.07 0.28	24.59 0.11	27.91 0.78	26.13 0.10	26.26 0.15	27.89 0.49	28.49 0.97
2449531.8730	24.70 0.13	27.02 0.25	24.13 0.10	27.24 0.35	26.51 0.16	26.64 0.20	27.05 0.24	26.34 0.18
2449533.4145	24.85 0.14	26.90 0.19	24.23 0.09	27.09 0.35	26.47 0.16	26.81 0.18	27.48 0.31	27.75 0.61
2449536.7662	24.92 0.16	26.08 0.12	24.16 0.09	27.58 0.40	26.68 0.17	26.46 0.14	27.48 0.30	27.85 0.54
2449545.9501	24.78 0.13	26.99 0.25	24.43 0.10	27.71 0.55	25.63 0.08	26.65 0.19	28.47 0.92	28.33 0.85
2449550.9774	25.05 0.14	26.94 0.24	24.46 0.11	26.72 0.21	26.32 0.16	26.06 0.11	27.25 0.26	26.68 0.21
2449559.8912	25.24 0.16	26.53 0.17	24.25 0.09	26.14 0.22	26.61 0.20	26.88 0.23	26.81 0.29	26.75 0.20
2449562.9742	25.23 0.16	27.06 0.25	24.28 0.10	27.33 0.48	26.43 0.18	26.42 0.20	27.81 0.50	28.34 0.89
2449564.6463	25.28 0.16	26.74 0.19	24.66 0.10	27.30 0.41	25.65 0.08	25.77 0.11	27.94 0.65	27.30 0.32
2449566.6607	25.03 0.14	27.01 0.23	24.35 0.09	27.94 0.84	25.60 0.10	25.99 0.12	27.16 0.35	26.85 0.25
2449569.6105	25.03 0.14	27.28 0.37	24.71 0.14	26.80 0.30	25.88 0.13	26.55 0.21	27.98 0.62	27.64 0.64
2449571.7555	24.84 0.14	26.74 0.26	24.39 0.10	27.50 0.68	26.00 0.12	27.21 0.35	26.76 0.25	27.98 0.84
2449573.6998	24.71 0.13	26.51 0.19	24.13 0.09	27.56 0.71	26.25 0.15	26.81 0.28	27.38 0.48	27.15 0.36
				F814W				
2449520.8115	23.89 0.11	25.49 0.17	23.88 0.13	—	24.68 0.10	25.49 0.16	—	26.13 0.34
2449532.0042	23.95 0.13	25.44 0.18	23.88 0.14	—	25.05 0.14	25.71 0.22	25.95 0.33	25.47 0.20
2449546.0806	24.06 0.12	25.55 0.22	23.88 0.12	—	24.74 0.09	25.44 0.15	26.35 0.42	26.06 0.33
2449560.0217	24.28 0.16	25.23 0.17	24.03 0.19	—	25.05 0.11	25.72 0.31	25.95 0.25	25.64 0.20
2449564.7803	24.26 0.16	24.99 0.17	24.05 0.21	—	24.81 0.10	25.08 0.15	25.91 0.31	25.55 0.24

HJD	C3-V11	C3-V12	C3-V13	C3-V14	C3-V15	C3-V16	C3-V17	C3-V18
				F555W				
2449506.8003	24.95 0.05	25.73 0.09	27.91 0.52	24.63 0.06	27.08 0.28	26.33 0.14	27.05 0.25	25.63 0.08
2449520.6803	26.15 0.13	24.97 0.06	28.15 0.73	24.84 0.09	27.25 0.35	25.50 0.08	26.55 0.14	26.42 0.19
2449521.9545	26.02 0.11	25.01 0.05	27.88 0.55	24.83 0.09	26.40 0.16	25.32 0.06	26.56 0.13	26.20 0.17
2449526.6457	26.00 0.10	25.27 0.07	26.76 0.22	24.34 0.06	27.47 0.40	25.57 0.08	26.47 0.17	26.09 0.18
2449528.6559	25.97 0.13	25.47 0.13	27.76 0.59	24.49 0.06	27.99 0.61	25.78 0.11	26.55 0.18	26.21 0.30
2449531.8730	24.84 0.08	25.50 0.10	28.25 0.93	24.49 0.06	27.38 0.34	25.97 0.11	27.53 0.65	25.45 0.10
2449533.4145	24.96 0.06	25.65 0.11	28.13 0.72	24.51 0.07	26.80 0.26	26.05 0.11	27.01 0.21	25.71 0.11
2449536.7662	25.33 0.08	25.49 0.08	27.40 0.40	24.58 0.06	27.18 0.32	26.22 0.14	26.65 0.14	25.91 0.15
2449545.9501	25.93 0.10	25.11 0.07	—	24.81 0.08	26.63 0.21	26.25 0.16	26.30 0.12	26.05 0.11
2449550.9774	25.97 0.13	25.68 0.11	27.98 0.78	24.46 0.07	28.30 0.89	25.38 0.08	26.67 0.15	26.34 0.13
2449559.8912	25.14 0.06	25.49 0.12	—	24.49 0.07	27.02 0.33	25.88 0.12	26.81 0.24	25.84 0.12
2449562.9742	25.50 0.09	24.70 0.06	26.46 0.24	24.63 0.09	27.38 0.41	26.13 0.15	26.72 0.22	26.13 0.15
2449564.6463	25.51 0.10	24.88 0.06	27.86 0.74	24.70 0.08	27.77 0.60	26.20 0.14	26.26 0.14	26.07 0.13
2449566.6607	25.63 0.11	24.91 0.06	27.31 0.38	24.84 0.07	27.50 0.59	26.20 0.19	26.33 0.18	26.03 0.16
2449569.6105	25.97 0.16	25.18 0.12	28.14 0.85	24.80 0.10	26.93 0.31	26.22 0.17	26.34 0.14	26.16 0.17
2449571.7555	26.06 0.13	25.22 0.09	27.31 0.46	24.92 0.08	26.83 0.32	26.17 0.19	26.40 0.24	26.60 0.26
2449573.6998	26.26 0.19	25.30 0.08	26.92 0.28	24.91 0.13	27.23 0.38	26.34 0.19	27.18 0.40	26.56 0.22
				F814W				
2449520.8115	24.89 0.12	24.31 0.08	—	24.23 0.07	25.27 0.15	24.09 0.08	26.13 0.31	25.32 0.21
2449532.0042	24.44 0.11	24.47 0.09	—	23.90 0.07	25.56 0.23	24.13 0.08	25.82 0.27	24.83 0.13
2449546.0806	24.89 0.13	24.27 0.10	—	23.97 0.07	—	24.59 0.11	26.55 0.46	25.05 0.13
2449560.0217	24.51 0.10	24.67 0.14	25.73 0.27	23.95 0.07	—	24.13 0.08	26.16 0.35	24.93 0.14
2449564.7803	24.59 0.12	24.21 0.11	—	24.06 0.07	—	24.28 0.11	25.96 0.31	25.23 0.22

quality index of 2 or 3 indicates some essential deficiency, e.g., muted amplitudes in one or both passbands, insufficient phase coverage in F814W. A quality index below 2 indicates fatal flaws such as apparent phase incoherence of variations in the two passbands.

Table 3 lists the characteristics of each variable star that can conceivably be classified as a Cepheid on the basis of the light curve in F555W alone, and where at least two observations are available in F814W. The stringent application of these conditions leads to the rejection of 32 out of the 106 variables identified in Figure 2. In addition we also exclude the variable C2-V32, whose period of 80 days has only been guessed at, and which in any case is too long to fall on the linear calibrated part of the *P-L* relation. The mean magnitudes $\langle$F555W$\rangle$ and $\langle$F814W$\rangle$ are converted to $\langle V\rangle$ and $\langle I\rangle$, using the equations

$$V = \mathrm{F555W} - 0.045(\mathrm{F555W} - \mathrm{F814W}) + 0.027(\mathrm{F555W} - \mathrm{F814W})^2 , \quad (2)$$

$$I = \mathrm{F814W} - 0.067(\mathrm{F555W} - \mathrm{F814W}) + 0.025(\mathrm{F555W} - \mathrm{F814W})^2 , \quad (3)$$

TABLE 2—*Continued*

HJD	C3-V19	C3-V20	C3-V21	C3-V22	C3-V23	C3-V24	C3-V25	C3-V26
				F555W				
2449506.8003	26.47 0.14	25.49 0.09	25.50 0.09	25.75 0.11	25.89 0.12	25.90 0.10	24.61 0.04	25.44 0.06
2449520.6803	26.26 0.17	26.38 0.14	25.53 0.07	24.81 0.07	26.88 0.22	25.32 0.07	24.93 0.06	25.65 0.08
2449521.9545	25.98 0.13	26.31 0.14	25.44 0.09	24.88 0.07	26.84 0.24	25.47 0.07	24.95 0.07	25.64 0.09
2449526.6457	26.78 0.22	26.65 0.20	24.75 0.06	25.11 0.10	26.86 0.20	25.68 0.09	25.16 0.10	25.86 0.13
2449528.6559	26.82 0.19	26.27 0.15	24.86 0.09	25.23 0.09	26.10 0.12	25.67 0.08	24.86 0.05	25.85 0.09
2449531.8730	26.23 0.13	25.42 0.10	24.64 0.05	25.28 0.09	25.93 0.12	25.77 0.09	24.53 0.05	25.94 0.10
2449533.4145	26.28 0.17	25.43 0.10	24.60 0.04	25.50 0.09	26.17 0.13	25.89 0.09	24.27 0.05	25.91 0.10
2449536.7662	26.02 0.13	25.53 0.09	24.71 0.05	25.61 0.09	26.45 0.17	25.99 0.09	24.21 0.05	25.81 0.09
2449545.9501	26.48 0.16	26.53 0.22	25.21 0.08	25.94 0.19	27.13 0.27	25.13 0.06	24.23 0.04	25.72 0.11
2449550.9774	25.86 0.13	26.32 0.21	25.13 0.05	25.82 0.12	26.39 0.17	25.34 0.06	24.34 0.04	25.59 0.10
2449559.8912	26.49 0.17	25.34 0.10	25.32 0.06	25.05 0.08	26.78 0.25	25.84 0.09	24.48 0.06	25.63 0.09
2449562.9742	25.92 0.12	25.60 0.15	25.31 0.08	25.10 0.09	27.19 0.37	26.13 0.14	24.56 0.06	25.71 0.08
2449564.6463	25.92 0.13	25.85 0.14	25.47 0.17	25.23 0.09	26.93 0.24	26.19 0.14	24.63 0.06	25.89 0.08
2449566.6607	26.20 0.13	26.24 0.19	25.55 0.08	25.18 0.08	27.02 0.26	25.88 0.10	24.64 0.05	25.94 0.10
2449569.6105	26.31 0.14	26.17 0.19	25.89 0.11	—	27.33 0.44	25.86 0.11	24.65 0.04	25.94 0.11
2449571.7555	26.61 0.23	26.21 0.18	—	25.32 0.10	27.01 0.30	24.98 0.05	24.73 0.06	25.97 0.09
2449573.6998	27.18 0.34	26.30 0.18	25.49 0.08	25.55 0.13	26.40 0.21	25.20 0.06	24.82 0.07	26.02 0.13
				F814W				
2449520.8115	25.27 0.16	24.97 0.19	24.11 0.06	24.22 0.07	—	24.03 0.05	23.69 0.06	24.42 0.10
2449532.0042	25.13 0.13	24.60 0.11	23.55 0.05	24.39 0.13	—	24.26 0.07	23.41 0.05	24.73 0.10
2449546.0806	25.56 0.21	—	23.69 0.06	24.68 0.12	—	23.89 0.05	23.15 0.05	24.39 0.11
2449560.0217	25.41 0.21	24.60 0.12	23.90 0.05	24.25 0.08	—	24.19 0.06	23.28 0.05	24.34 0.07
2449564.7803	24.80 0.13	24.95 0.18	23.89 0.06	24.23 0.11	—	24.16 0.10	23.27 0.05	24.47 0.09

HJD	C3-V27	C3-V28	C3-V29	C3-V30	C3-V31	C3-V32	C3-V33	C3-V34
				F555W				
2449506.8003	27.19 0.28	26.02 0.12	27.73 0.37	26.07 0.18	25.71 0.08	26.08 0.09	25.94 0.07	27.23 0.38
2449520.6803	28.43 0.87	25.73 0.08	26.91 0.20	25.91 0.12	25.63 0.09	25.18 0.05	26.05 0.08	26.58 0.16
2449521.9545	27.51 0.38	26.14 0.09	27.20 0.49	26.01 0.14	25.55 0.06	25.24 0.05	26.11 0.12	26.50 0.17
2449526.6457	26.86 0.22	26.50 0.15	27.22 0.24	26.20 0.11	25.50 0.07	25.39 0.06	25.93 0.10	27.05 0.21
2449528.6559	27.67 0.41	26.75 0.20	26.76 0.20	26.14 0.10	25.45 0.07	25.58 0.06	25.56 0.08	26.67 0.14
2449531.8730	27.55 0.38	26.50 0.17	26.51 0.16	25.68 0.09	25.65 0.07	25.63 0.06	25.66 0.09	26.39 0.13
2449533.4145	27.94 0.63	25.93 0.09	26.96 0.20	25.58 0.09	25.68 0.08	25.64 0.07	25.63 0.10	25.76 0.07
2449536.7662	27.35 0.32	26.23 0.12	27.18 0.25	25.89 0.09	25.57 0.08	25.88 0.08	25.96 0.09	26.09 0.11
2449545.9501	28.03 0.61	26.68 0.20	27.57 0.55	26.32 0.13	25.65 0.07	26.19 0.10	25.91 0.11	26.57 0.13
2449550.9774	—	26.21 0.14	27.76 0.47	25.56 0.08	25.41 0.07	25.72 0.06	25.49 0.08	26.71 0.18
2449559.8912	—	26.65 0.20	26.73 0.21	26.05 0.15	25.53 0.06	25.19 0.05	25.86 0.10	26.45 0.14
2449562.9742	27.85 0.57	25.82 0.09	26.65 0.22	26.13 0.12	25.63 0.07	25.39 0.06	26.10 0.11	26.63 0.19
2449564.6463	27.58 0.42	25.94 0.12	26.60 0.18	25.92 0.12	25.76 0.07	25.34 0.06	25.80 0.10	27.13 0.31
2449566.6607	27.89 0.78	26.27 0.18	26.85 0.27	25.67 0.08	25.80 0.11	25.51 0.08	25.85 0.12	26.74 0.18
2449569.6105	26.70 0.22	26.69 0.25	27.00 0.29	25.61 0.09	26.03 0.18	25.59 0.07	25.51 0.08	26.61 0.17
2449571.7555	28.13 0.69	26.64 0.21	27.63 0.52	25.78 0.13	25.92 0.17	25.71 0.12	25.67 0.10	26.80 0.28
2449573.6998	—	—	27.34 0.40	25.96 0.15	25.74 0.12	25.69 0.11	25.64 0.09	25.82 0.10
				F814W				
2449520.8115	25.14 0.12	25.25 0.17	25.96 0.28	25.00 0.22	25.05 0.13	24.25 0.06	25.31 0.16	25.55 0.19
2449532.0042	24.95 0.13	25.44 0.20	25.71 0.24	24.90 0.11	25.31 0.14	24.43 0.07	24.83 0.09	25.73 0.19
2449546.0806	25.02 0.13	—	26.09 0.32	25.07 0.13	25.17 0.13	24.88 0.10	25.07 0.10	25.39 0.21
2449560.0217	25.05 0.16	—	25.47 0.19	25.15 0.13	25.49 0.17	24.35 0.08	24.98 0.11	25.61 0.21
2449564.7803	25.09 0.13	25.42 0.22	25.80 0.28	25.07 0.16	25.26 0.15	24.21 0.07	24.95 0.14	—

which are practically identical to the transformations given by Holtzman et al. (1995b).[4] The $\sigma(\langle V\rangle)$ and $\sigma(\langle I\rangle)$ columns in Table 3 are uncertainties in the mean V and I magnitudes based on the measured errors in the photometry of the individual epochs. The quality index discussed above is also listed in this table.

Table 4 contains the summary information of those 32 variable stars that are not classified as Cepheids. From the remarks given in column 5 it is obvious that the lack of F814W observations is the main reason for nonacceptance of Cepheid-like objects.

[4] These differ only in the fact that the color term $(V-I)$ in the right hand sides of these equations has been replaced by (F555W − F814W), thus eliminating the need for an iterative solution. The resulting difference is negligible.

5. PERIOD-LUMINOSITY RELATION AND THE DISTANCE MODULUS

5.1. *The P-L Diagram in V*

The *P-L* relation for all definite, possible, and Cepheid-like objects is shown in Figure 5. We adopt the *P-L* relation

TABLE 2—*Continued*

HJD	C3-V35	C3-V36	C3-V37	C4-V1	C4-V2	C4-V3	C4-V4	C4-V5
				F555W				
2449506.8003	26.33 0.13	26.84 0.18	26.68 0.14	27.16 0.27	27.53 0.37	26.07 0.14	27.52 0.29	25.95 0.09
2449520.6803	26.46 0.12	26.57 0.13	27.40 0.30	26.74 0.18	27.80 0.45	27.10 0.30	27.21 0.22	25.65 0.06
2449521.9545	26.46 0.12	26.72 0.21	27.36 0.32	27.59 0.46	25.69 0.13	26.47 0.17	27.26 0.27	25.72 0.09
2449526.6457	26.38 0.11	26.66 0.19	27.01 0.22	27.27 0.34	27.17 0.30	26.47 0.14	26.45 0.15	25.97 0.10
2449528.6559	25.84 0.08	26.76 0.19	27.31 0.27	—	26.77 0.20	26.86 0.20	27.09 0.26	26.01 0.15
2449531.8730	25.63 0.06	26.41 0.16	27.67 0.34	27.08 0.33	—	26.57 0.17	27.01 0.24	25.90 0.11
2449533.4145	25.82 0.12	25.90 0.12	—	—	—	26.22 0.12	26.94 0.19	25.75 0.09
2449536.7662	26.06 0.09	26.20 0.14	26.81 0.16	27.13 0.23	26.92 0.21	26.52 0.14	27.01 0.38	25.05 0.05
2449545.9501	26.33 0.11	26.64 0.17	27.20 0.25	27.22 0.28	27.44 0.36	26.89 0.21	27.21 0.30	25.61 0.07
2449550.9774	25.71 0.09	26.89 0.20	27.43 0.33	—	26.55 0.13	26.51 0.16	26.49 0.16	25.99 0.12
2449559.8912	26.36 0.13	26.16 0.11	27.63 0.40	27.38 0.40	—	26.48 0.14	27.05 0.25	24.99 0.06
2449562.9742	26.39 0.14	26.63 0.18	26.30 0.17	26.86 0.32	27.42 0.45	26.77 0.24	27.36 0.47	25.07 0.06
2449564.6463	26.16 0.13	26.58 0.18	27.02 0.24	—	27.55 0.44	26.99 0.23	27.42 0.44	25.28 0.07
2449566.6607	25.83 0.09	26.80 0.19	—	—	27.60 0.37	26.34 0.13	26.56 0.19	25.34 0.08
2449569.6105	25.71 0.09	26.93 0.22	26.76 0.19	—	—	26.80 0.23	—	25.24 0.07
2449571.7555	25.94 0.19	26.51 0.17	26.39 0.15	—	—	26.83 0.27	27.25 0.37	25.68 0.10
2449573.6998	25.78 0.10	26.44 0.18	26.58 0.21	26.41 0.24	26.90 0.31	26.43 0.16	26.83 0.30	25.92 0.11
				F814W				
2449520.8115	25.88 0.38	25.65 0.25	26.13 0.34	—	—	25.61 0.16	25.72 0.20	24.71 0.08
2449532.0042	24.88 0.09	25.50 0.17	26.67 0.38	26.34 0.40	—	25.90 0.18	25.56 0.17	25.23 0.12
2449546.0806	25.49 0.13	25.84 0.23	25.65 0.17	26.41 0.40	—	25.99 0.26	25.86 0.20	24.65 0.09
2449560.0217	25.59 0.25	25.47 0.17	26.41 0.39	26.06 0.30	—	25.70 0.23	25.71 0.21	24.57 0.07
2449564.7803	25.98 0.23	25.13 0.15	25.34 0.16	26.34 0.50	—	26.58 0.38	25.99 0.33	24.69 0.22

HJD	C4-V6	C4-V7	C4-V8	C4-V9	C4-V10	C4-V11	C4-V12	C4-V13
				F555W				
2449506.8003	27.23 0.31	—	25.65 0.09	—	25.98 0.12	25.72 0.07	25.15 0.05	25.19 0.05
2449520.6803	26.68 0.20	—	24.95 0.05	—	25.71 0.12	26.13 0.11	25.13 0.04	25.43 0.06
2449521.9545	27.10 0.26	27.89 0.47	24.96 0.04	27.41 0.31	25.66 0.10	25.89 0.09	25.08 0.05	25.53 0.07
2449526.6457	26.42 0.13	26.65 0.18	25.13 0.05	27.71 0.32	26.07 0.18	25.51 0.06	24.63 0.04	25.59 0.06
2449528.6559	27.18 0.26	27.64 0.35	25.26 0.05	27.93 0.38	26.09 0.15	25.63 0.08	24.67 0.04	25.69 0.08
2449531.8730	26.69 0.21	27.63 0.41	25.34 0.06	27.31 0.27	26.32 0.16	25.90 0.08	25.05 0.05	25.72 0.08
2449533.4145	27.23 0.28	28.09 0.49	25.32 0.06	27.45 0.38	26.09 0.17	25.96 0.08	24.89 0.05	25.75 0.08
2449536.7662	26.85 0.17	—	25.42 0.06	—	25.59 0.08	26.10 0.11	24.94 0.04	25.84 0.09
2449545.9501	26.59 0.14	27.31 0.30	25.71 0.08	—	26.27 0.15	25.53 0.07	24.84 0.04	25.75 0.07
2449550.9774	26.80 0.22	27.73 0.49	25.88 0.10	—	26.25 0.17	25.69 0.09	—	—
2449559.8912	27.34 0.41	—	25.45 0.09	—	25.92 0.10	25.92 0.12	24.82 0.04	24.99 0.05
2449562.9742	27.22 0.28	—	25.00 0.05	26.80 0.21	26.26 0.16	26.00 0.12	24.86 0.05	24.95 0.04
2449564.6463	27.42 0.38	—	24.91 0.06	—	26.30 0.15	25.69 0.10	24.91 0.05	25.02 0.05
2449566.6607	26.88 0.20	—	24.92 0.04	—	26.40 0.15	25.70 0.10	24.68 0.04	25.19 0.06
2449569.6105	27.08 0.29	26.65 0.21	24.94 0.05	—	25.93 0.13	25.56 0.08	24.70 0.05	25.14 0.05
2449571.7555	26.95 0.28	—	25.00 0.05	—	25.34 0.09	25.88 0.12	24.90 0.04	25.23 0.09
2449573.6998	27.33 0.41	27.21 0.39	25.01 0.05	—	25.59 0.09	26.11 0.15	24.85 0.05	25.30 0.07
				F814W				
2449520.8115	25.66 0.23	25.78 0.29	23.92 0.05	—	25.10 0.15	25.09 0.11	22.64 0.05	24.05 0.05
2449532.0042	25.48 0.17	25.48 0.21	24.21 0.07	—	25.69 0.30	24.80 0.11	22.60 0.05	24.27 0.06
2449546.0806	25.61 0.17	25.65 0.17	24.50 0.10	—	25.67 0.23	24.81 0.11	22.32 0.05	24.43 0.06
2449560.0217	25.43 0.17	25.65 0.22	24.27 0.08	—	25.33 0.15	24.78 0.10	22.52 0.05	23.90 0.05
2449564.7803	25.61 0.19	25.70 0.28	24.05 0.09	—	25.75 0.24	24.85 0.13	22.56 0.05	23.94 0.05

in V from Madore & Freedman (1991)

$$M_V = -2.76 \log P - 1.40 , \quad (4)$$

whose companion relation in I is

$$M_I = -3.06 \log P - 1.81 . \quad (5)$$

The M_V calibration is identical within 0.05 mag to those given earlier by Sandage & Tammann (1968) and by Feast & Walker (1987).

The continuous line in Figure 5 shows the fit that forces the slope from equation (4), implying (first cut) an apparent distance modulus in V of $\mu_V = 31.16$. The dashed lines drawn 0.4 mags above and below indicate the expected scatter about the mean fit ridge line due to the intrinsic width of the Cepheid P-L relation (Sandage & Tammann 1968). Note the agreement of this fit over nearly the entire range of periods, with the expected bias at the very faint end for periods shorter than 10 days, due to the magnitude limit encountered in the discovery of the Cepheids. Some points spill out past the instability strip boundaries, which could be for two reasons: (1) errors in measurement are large, and (2) the presence of significant differential extinction from Cepheid to Cepheid. As we shall show in § 5.4 and in the Appendix, the primary cause is the measurement errors, and

TABLE 2—*Continued*

HJD	C4-V14	C4-V15	C4-V16	C4-V17	C4-V18	C4-V19	C4-V20	C4-V21
				F555W				
2449506.8003	26.13 0.11	26.68 0.15	26.35 0.12	26.43 0.15	26.74 0.21	26.55 0.15	25.00 0.07	26.53 0.15
2449520.6803	25.94 0.10	26.48 0.15	26.09 0.09	26.89 0.19	26.66 0.19	26.81 0.22	25.20 0.07	26.30 0.13
2449521.9545	26.08 0.11	26.45 0.12	26.10 0.12	26.89 0.25	26.82 0.19	26.08 0.11	25.21 0.07	26.23 0.13
2449526.6457	26.18 0.14	26.46 0.15	26.44 0.14	26.22 0.11	26.44 0.15	26.26 0.16	25.24 0.07	26.61 0.15
2449528.6559	26.20 0.13	26.01 0.09	26.60 0.15	26.39 0.16	25.97 0.11	26.65 0.18	25.30 0.06	27.05 0.27
2449531.8730	26.20 0.12	26.31 0.11	26.27 0.14	26.76 0.22	26.19 0.09	26.52 0.16	25.38 0.08	26.94 0.26
2449533.4145	25.35 0.08	26.28 0.13	25.67 0.08	26.53 0.16	26.48 0.12	26.76 0.22	25.53 0.10	26.24 0.14
2449536.7662	25.39 0.08	26.41 0.16	25.99 0.10	26.02 0.13	26.74 0.18	26.89 0.22	25.52 0.09	25.99 0.09
2449545.9501	25.89 0.11	26.02 0.12	26.58 0.17	26.25 0.12	25.98 0.09	26.36 0.15	25.63 0.09	26.70 0.25
2449550.9774	26.30 0.12	26.38 0.15	—	26.56 0.19	26.56 0.16	26.59 0.17	25.85 0.12	27.02 0.35
2449559.8912	25.36 0.09	26.40 0.16	26.48 0.18	26.50 0.16	26.38 0.14	26.63 0.16	25.14 0.06	26.05 0.15
2449562.9742	25.51 0.11	26.02 0.10	26.38 0.17	26.64 0.19	—	26.97 0.27	25.10 0.11	26.68 0.23
2449564.6463	25.44 0.09	26.38 0.15	26.42 0.19	27.02 0.25	25.94 0.13	27.13 0.36	24.92 0.05	27.35 0.42
2449566.6607	25.92 0.11	26.43 0.17	26.03 0.12	26.28 0.12	—	26.40 0.17	25.01 0.07	26.84 0.27
2449569.6105	25.99 0.11	26.51 0.20	25.55 0.08	26.57 0.21	26.61 0.19	26.38 0.17	25.17 0.08	—
2449571.7555	26.10 0.19	27.00 0.26	26.05 0.12	26.65 0.19	26.65 0.23	26.40 0.17	25.10 0.06	26.84 0.32
2449573.6998	26.09 0.14	27.11 0.37	26.21 0.17	26.90 0.29	26.84 0.28	26.63 0.24	24.99 0.07	25.85 0.13
				F814W				
2449520.8115	24.84 0.12	25.52 0.18	25.32 0.11	25.72 0.18	25.47 0.16	25.06 0.11	23.33 0.05	25.32 0.17
2449532.0042	25.13 0.13	25.30 0.15	25.82 0.20	25.77 0.26	24.94 0.08	25.06 0.12	23.33 0.07	25.89 0.26
2449546.0806	24.92 0.11	24.95 0.10	25.55 0.17	25.73 0.20	24.90 0.13	24.73 0.12	23.39 0.05	25.77 0.25
2449560.0217	24.55 0.10	25.27 0.17	25.69 0.22	25.77 0.18	25.30 0.14	24.78 0.10	23.24 0.05	25.58 0.17
2449564.7803	24.53 0.09	25.13 0.13	25.39 0.17	26.07 0.25	24.92 0.14	24.96 0.13	23.14 0.05	25.83 0.29

HJD	C4-V22	C4-V23
2449506.8003	24.59 0.05	26.85 0.17
2449520.6803	25.25 0.06	26.93 0.19
2449521.9545	25.32 0.06	26.98 0.20
2449526.6457	25.38 0.05	25.76 0.09
2449528.6559	25.45 0.08	25.98 0.10
2449531.8730	25.63 0.10	26.33 0.12
2449533.4145	25.51 0.08	26.71 0.14
2449536.7662	25.64 0.09	26.70 0.17
2449545.9501	24.80 0.05	26.05 0.10
2449550.9774	24.64 0.04	26.51 0.12
2449559.8912	25.17 0.13	26.52 0.14
2449562.9742	25.24 0.06	25.78 0.12
2449564.6463	25.34 0.09	26.21 0.17
2449566.6607	25.24 0.08	26.41 0.15
2449569.6105	25.40 0.10	26.38 0.18
2449571.7555	25.80 0.13	26.74 0.25
2449573.6998	25.53 0.10	26.68 0.24
2449520.8115	24.01 0.05	26.15 0.30
2449532.0042	24.32 0.05	25.45 0.16
2449546.0806	23.96 0.05	25.30 0.13
2449560.0217	24.05 0.05	25.56 0.22
2449564.7803	24.07 0.08	25.17 0.17

any differential extinction is smaller than what we can measure.

5.2. *P-L Diagram in I*

In Figure 6, we show the *P-L* relation for the same objects in $\langle I \rangle$. The continuous line shows the mean relation from equation (5), and using for the first cut, $\mu_V = 31.16$, as if the extinction and reddening is zero. The instability strip envelope lines are drawn with dashed lines 0.32 mags above and below, as appropriate for this passband due to the intrinsic width of the instability strip, and assuming zero measurement errors. The presence of overall reddening should make these lines appear too faint relative to the data.

Some problems are immediately obvious:

1. The observed data for periods shorter than $\log P = 1.3$ define an apparent slope that is too shallow compared to the canonical slope in the *P-L* relation defined by equation (5). This effect is not noticeable in the *V* data, indicating that the fainter objects may be systematically mismeasured in *I*. We must examine this possibility more critically in § 5.3.

2. Irrespective of how one moves the *P-L* relation band relative to the data points (for example, to account for

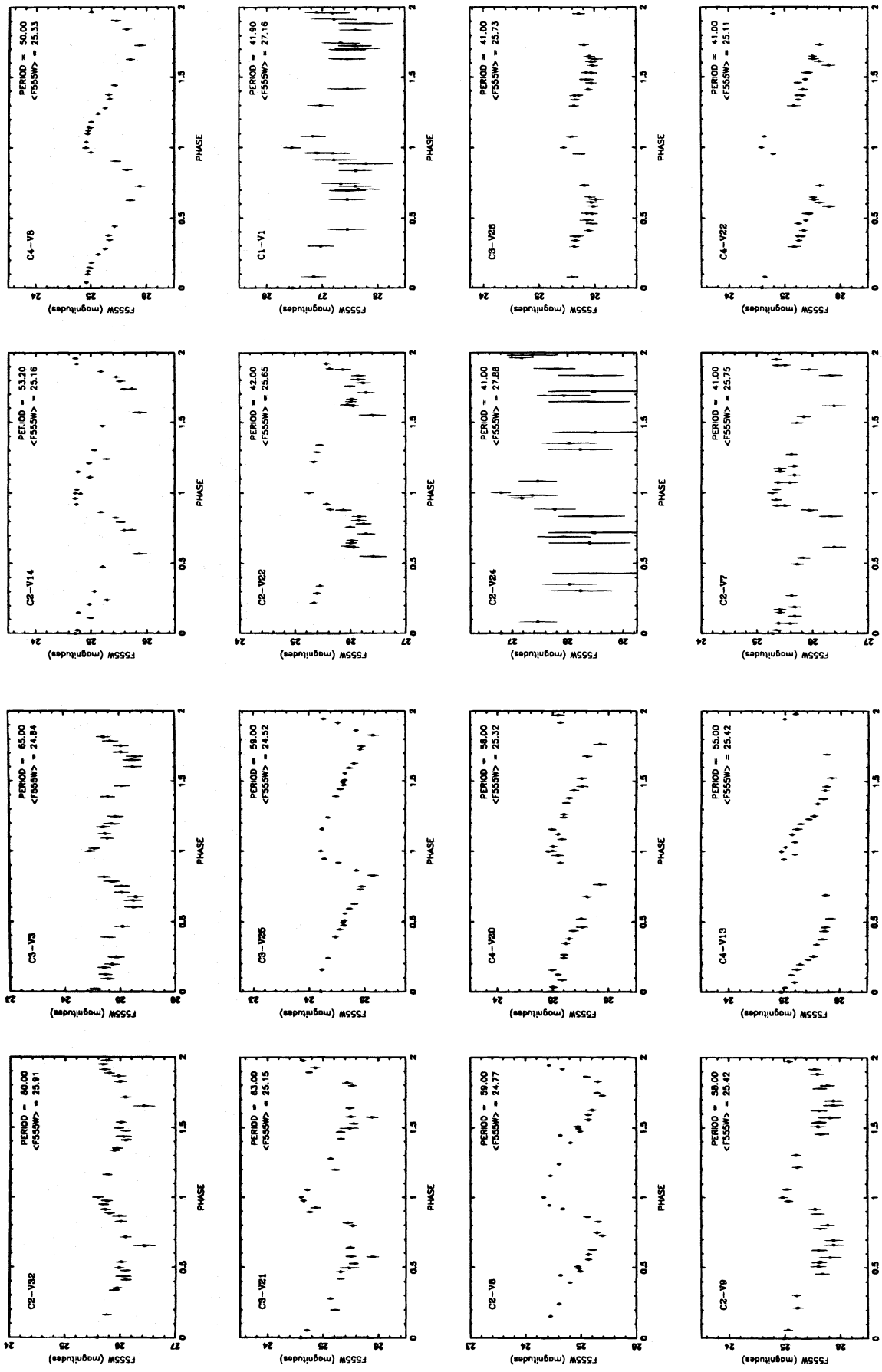

FIG. 3.—Light curves in the F555W passband ground system. All calibrations except color transformation to standard V and I and the 0.05 mag offset due to the short/long calibration problem (§ 3.3) have been applied. The adopted periods and mean F555W magnitudes (uncorrected for the 0.05 mag effect), averaged over the light curve, are marked at the upper right.

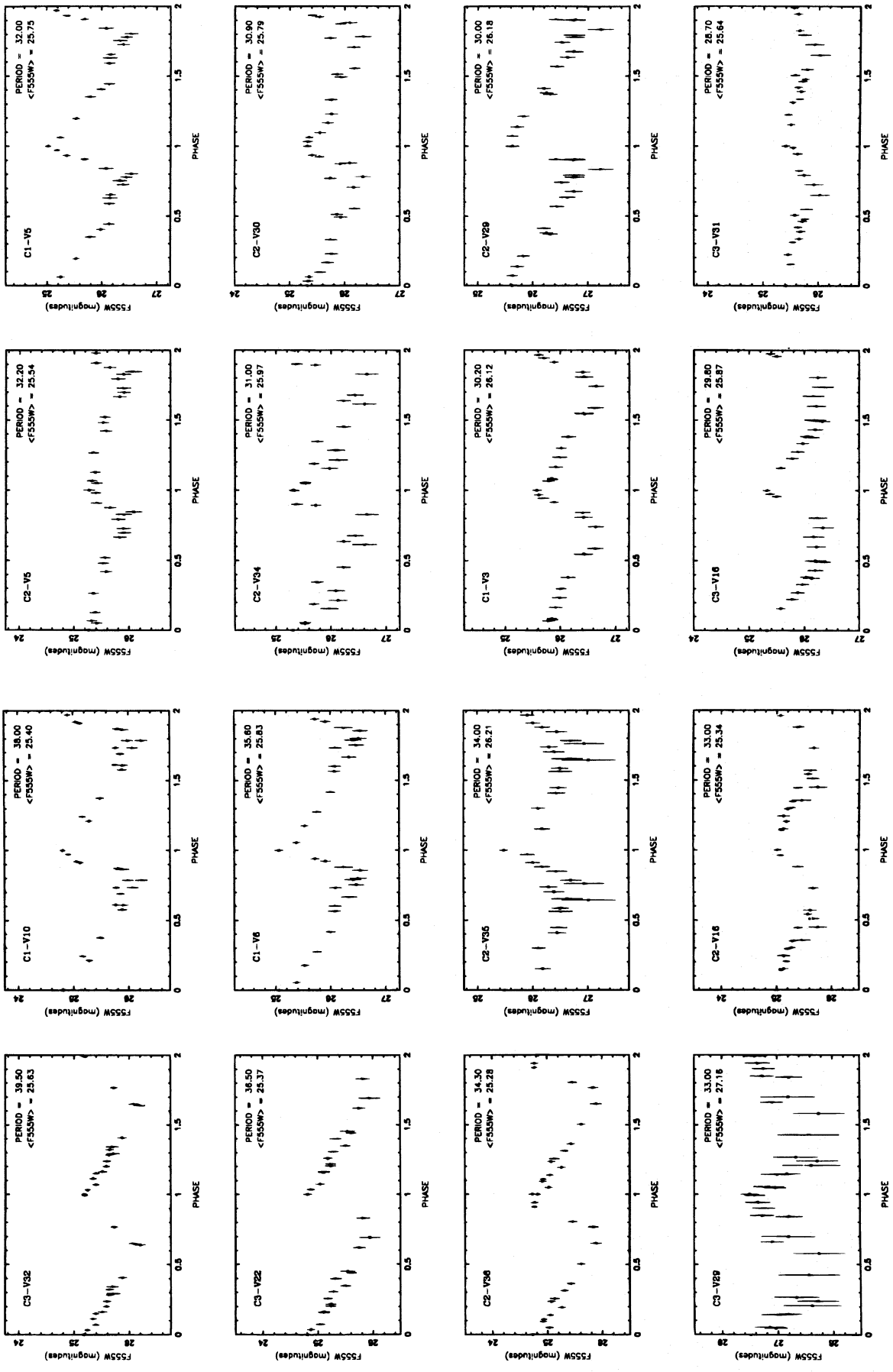

FIG. 3.—*Continued*

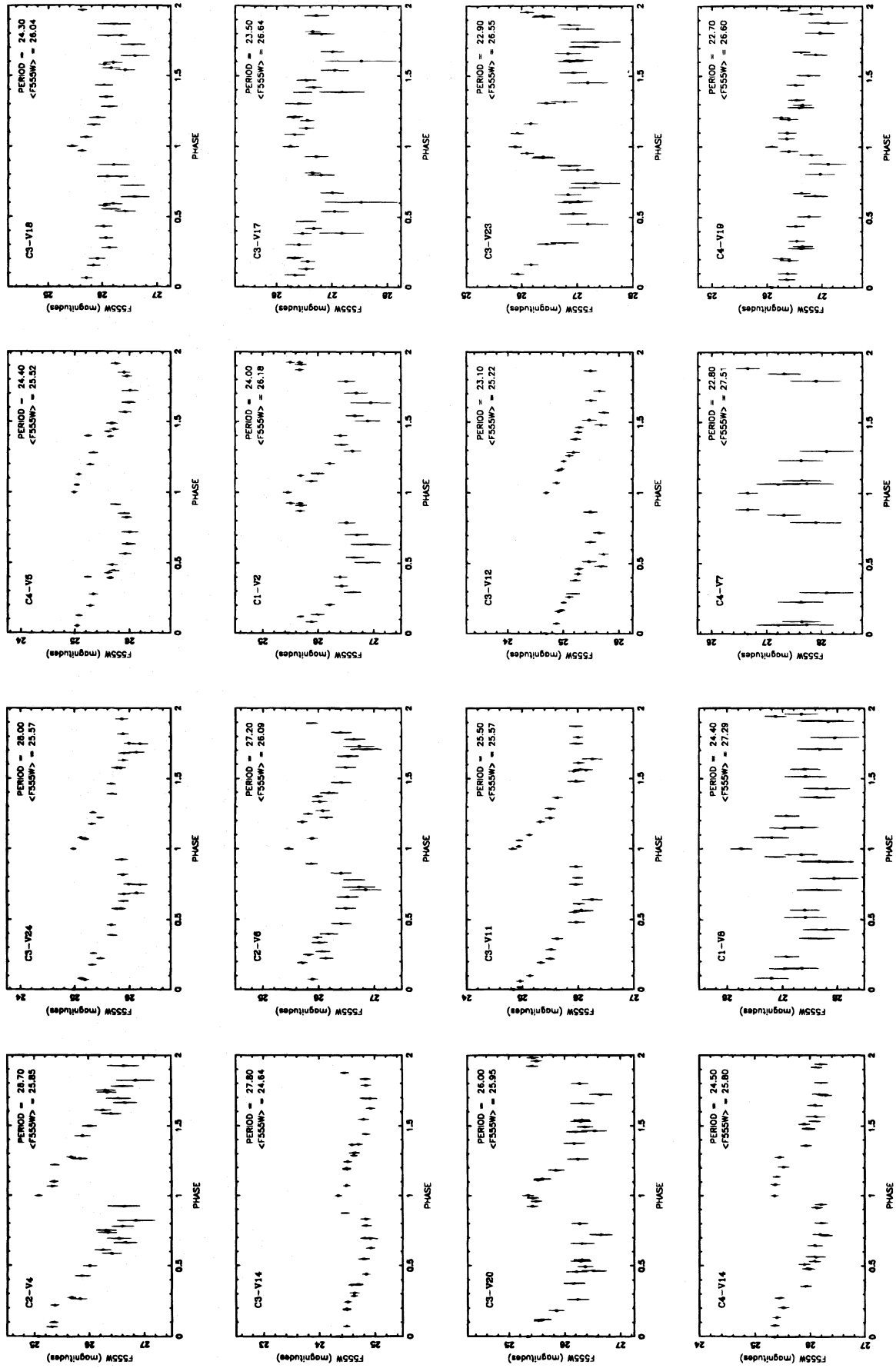

FIG. 3.—*Continued*

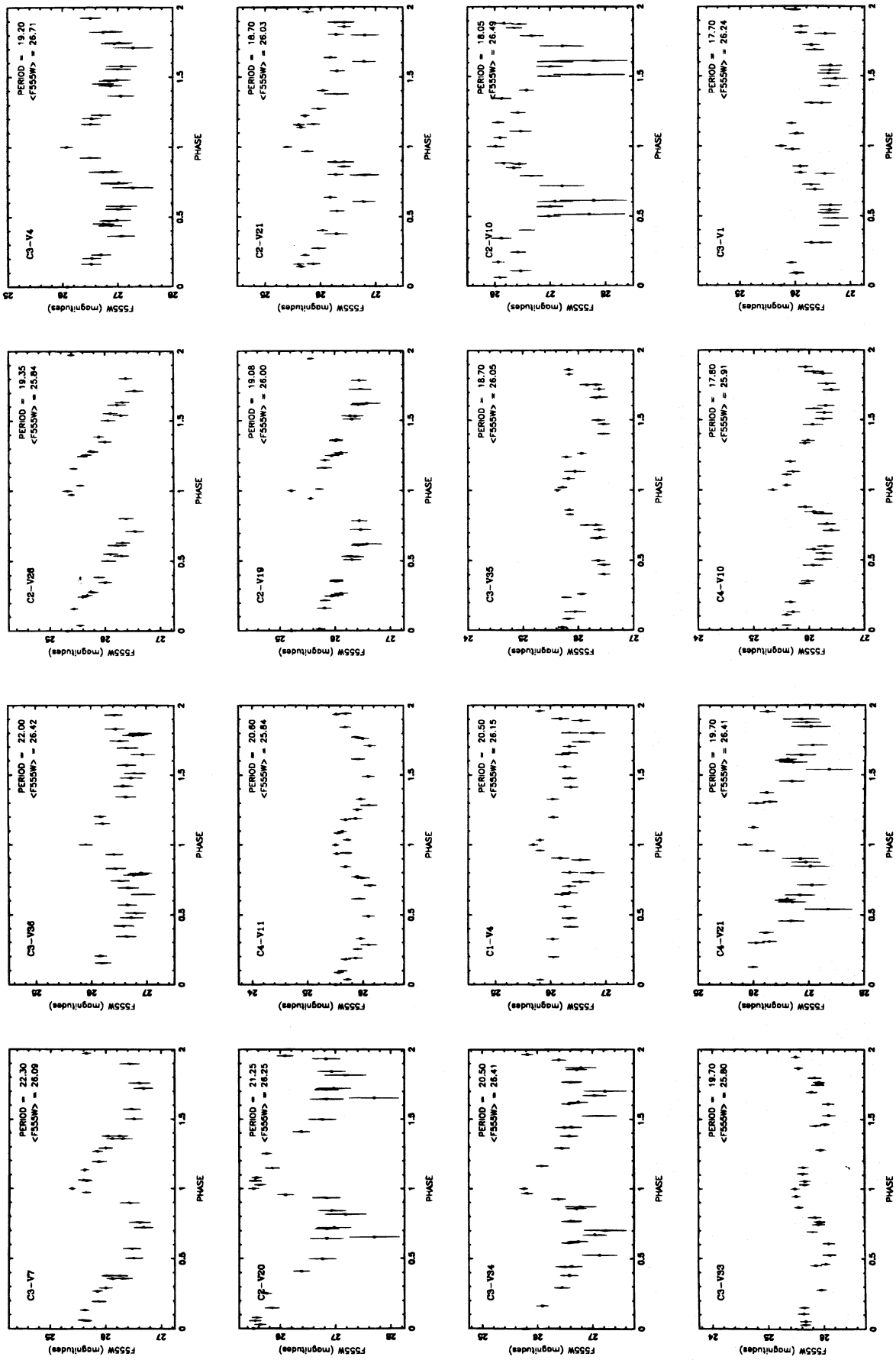

FIG. 3.—*Continued*

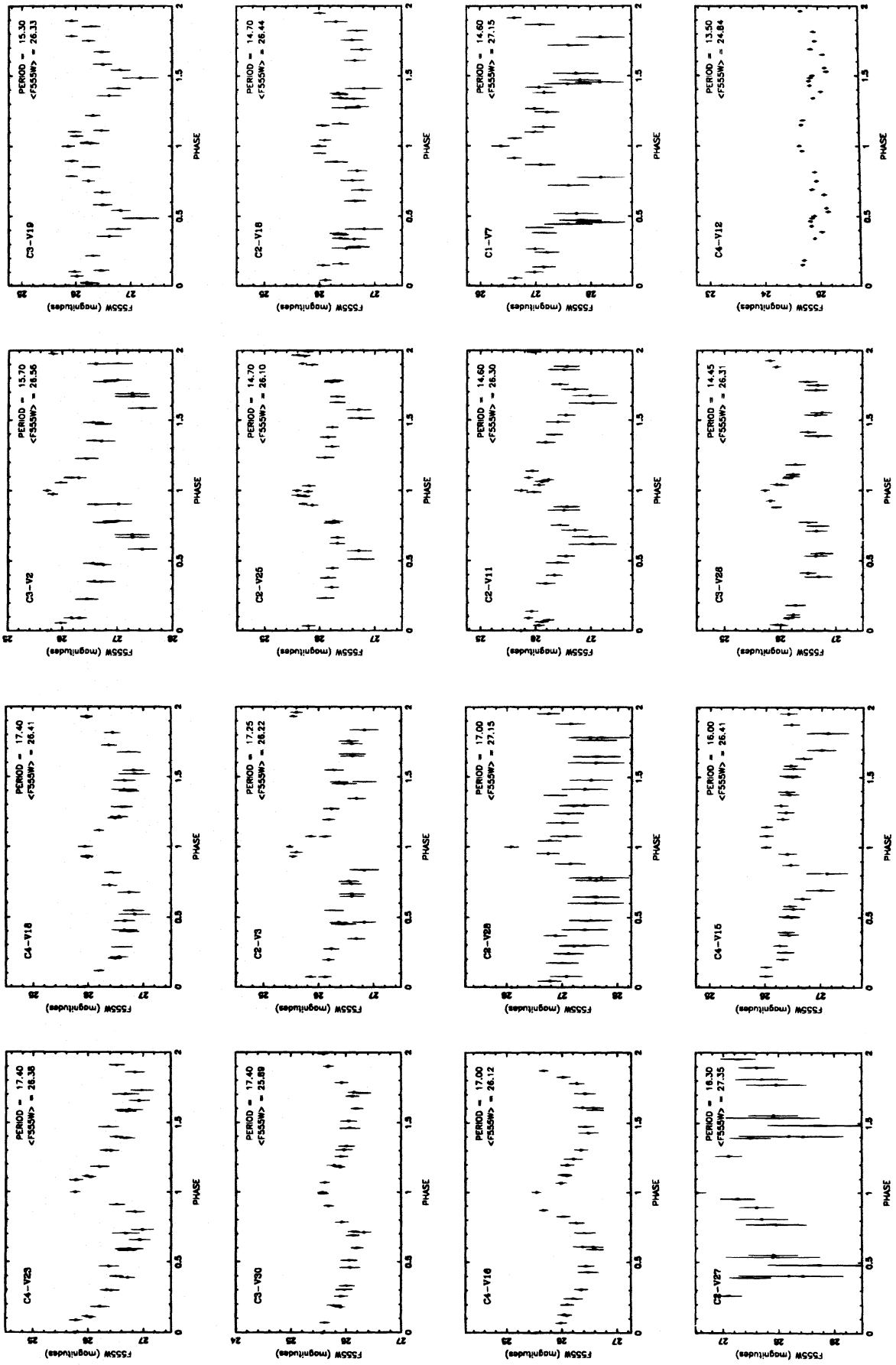

FIG. 3.—*Continued*

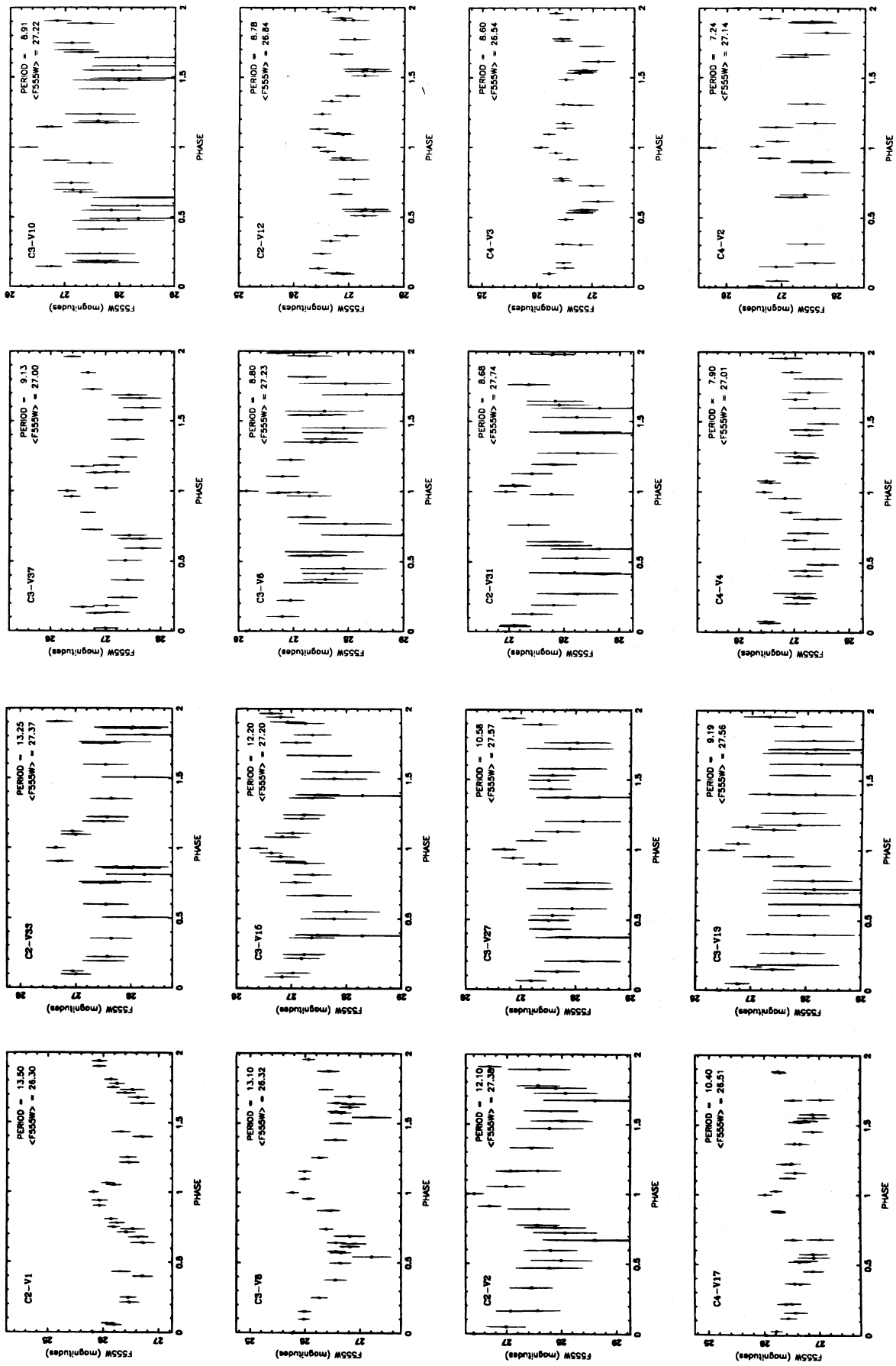

FIG. 3.—*Continued*

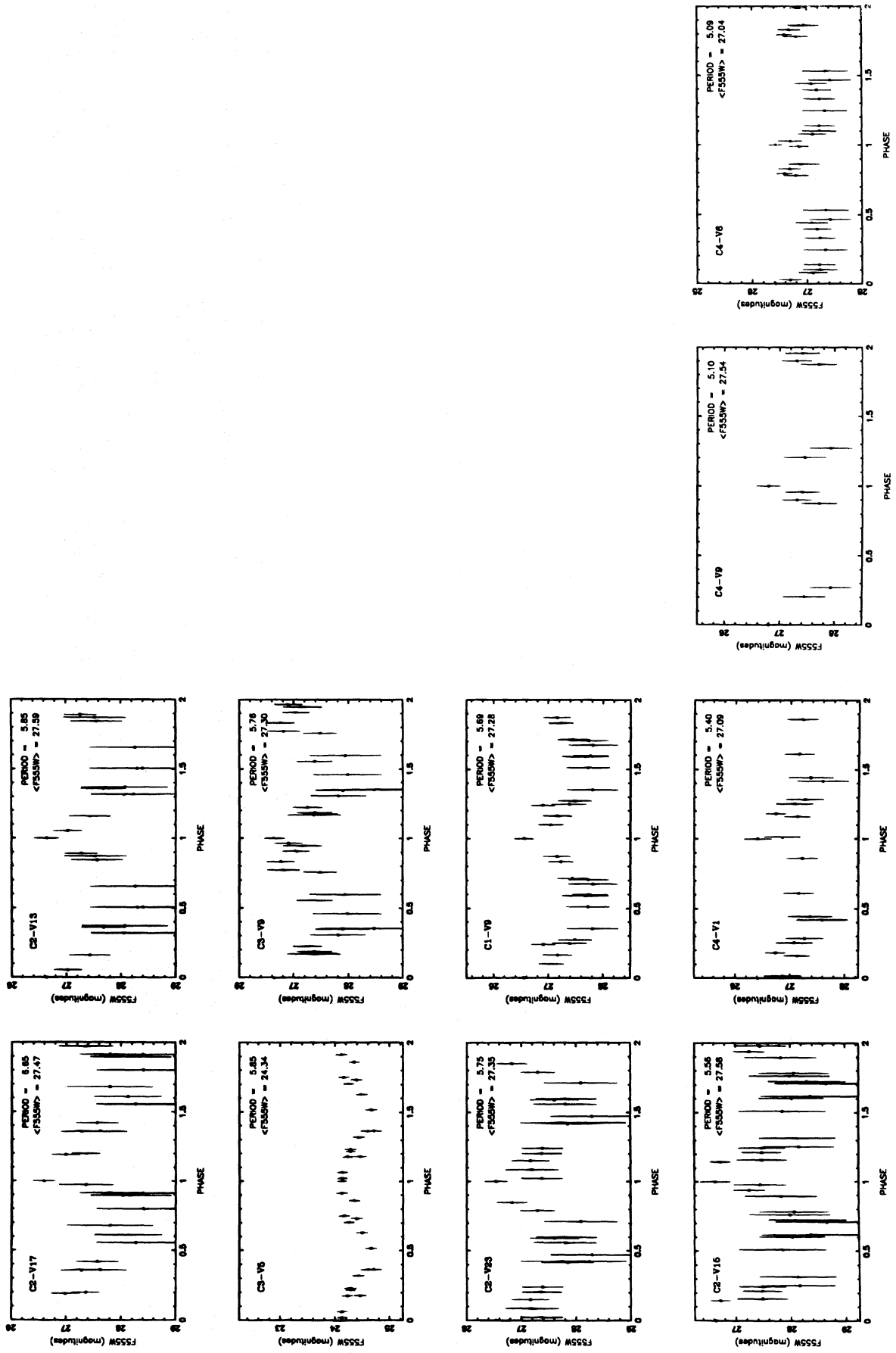

FIG. 3.—*Continued*

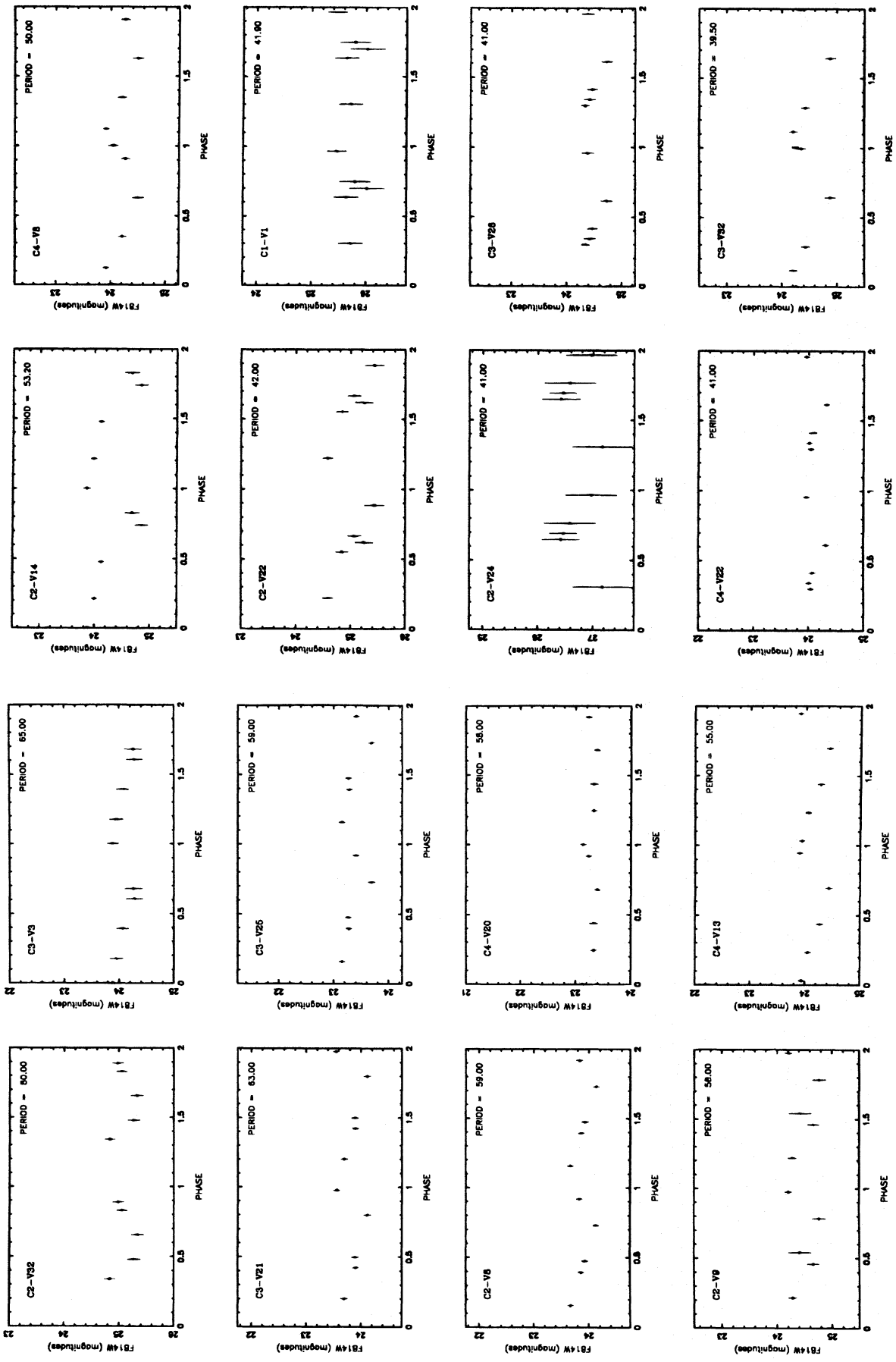

FIG. 4.—Partial light curves in F814W for the five available epochs. Phasing is that of the more complete F555W light curves in Fig. 3.

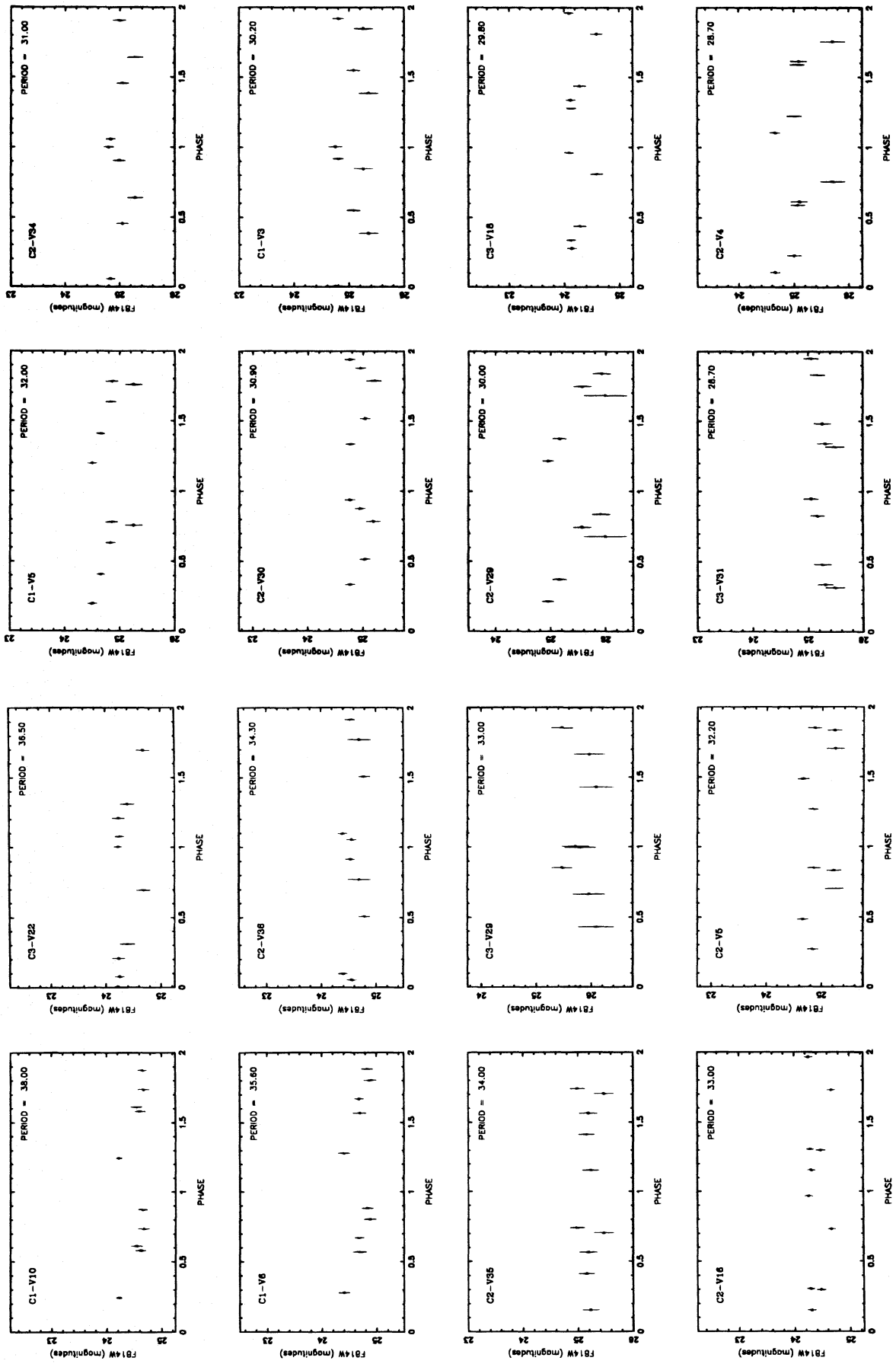

FIG. 4.—*Continued*

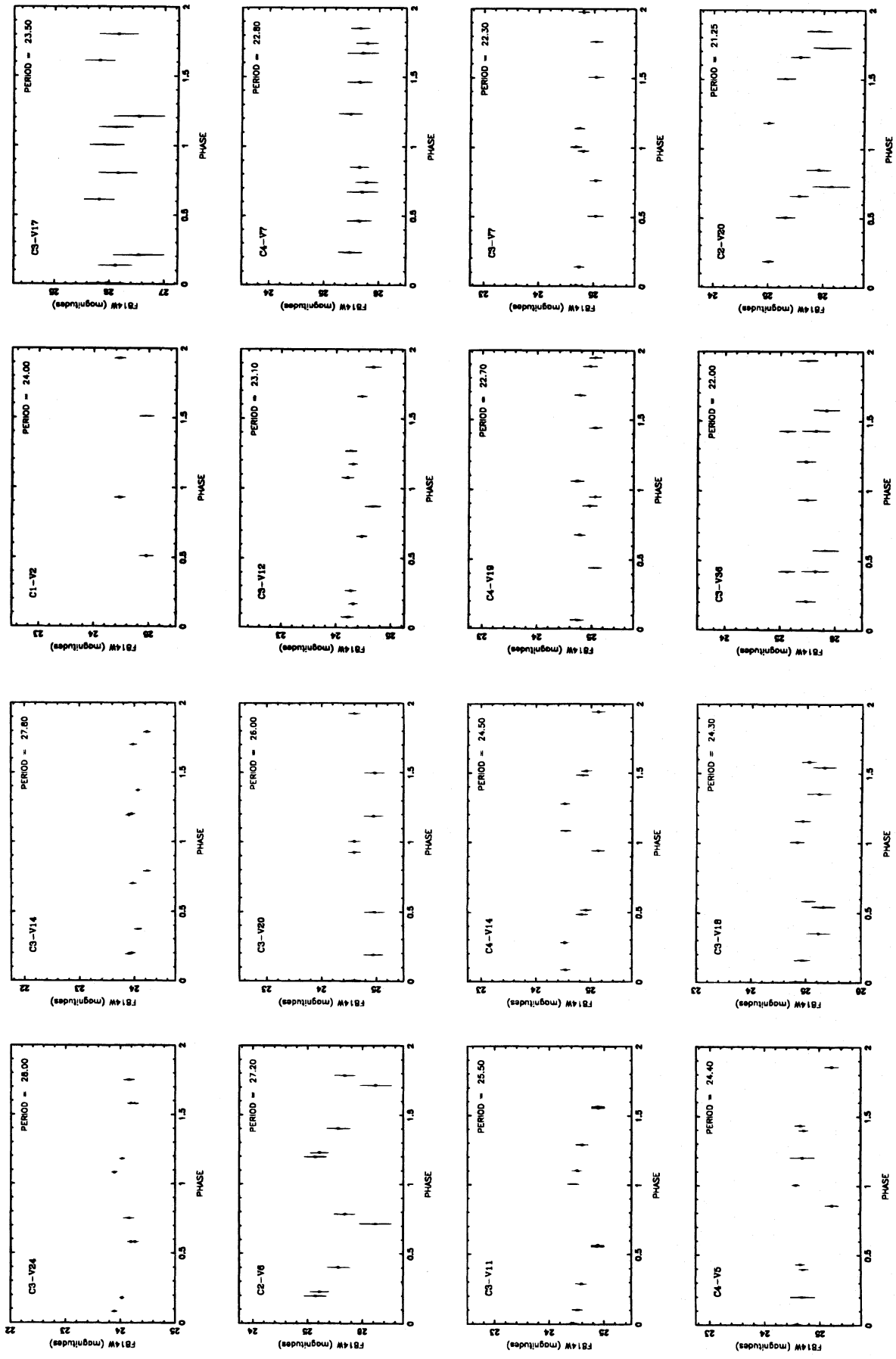

FIG. 4.—*Continued*

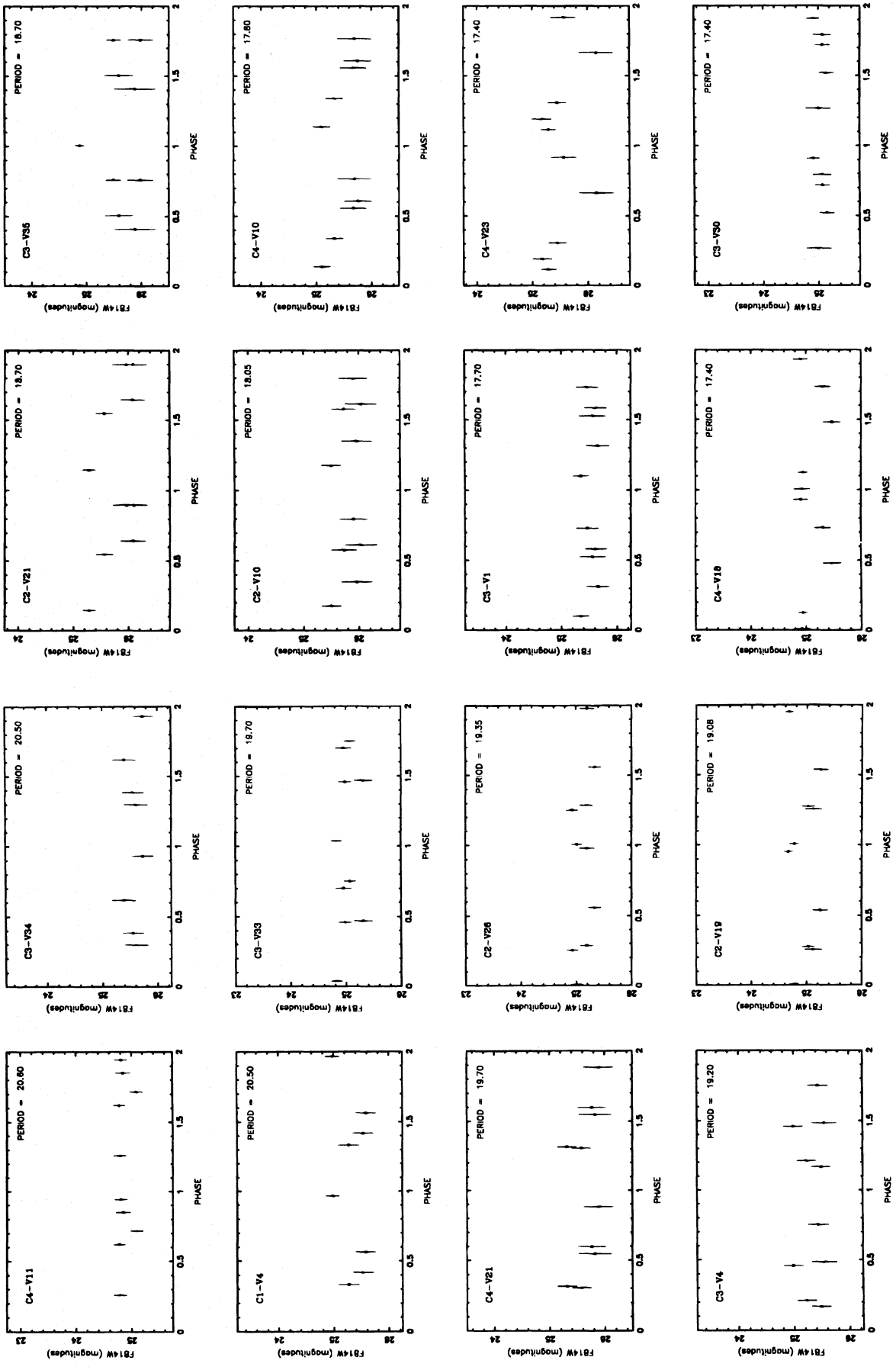

FIG. 4.—*Continued*

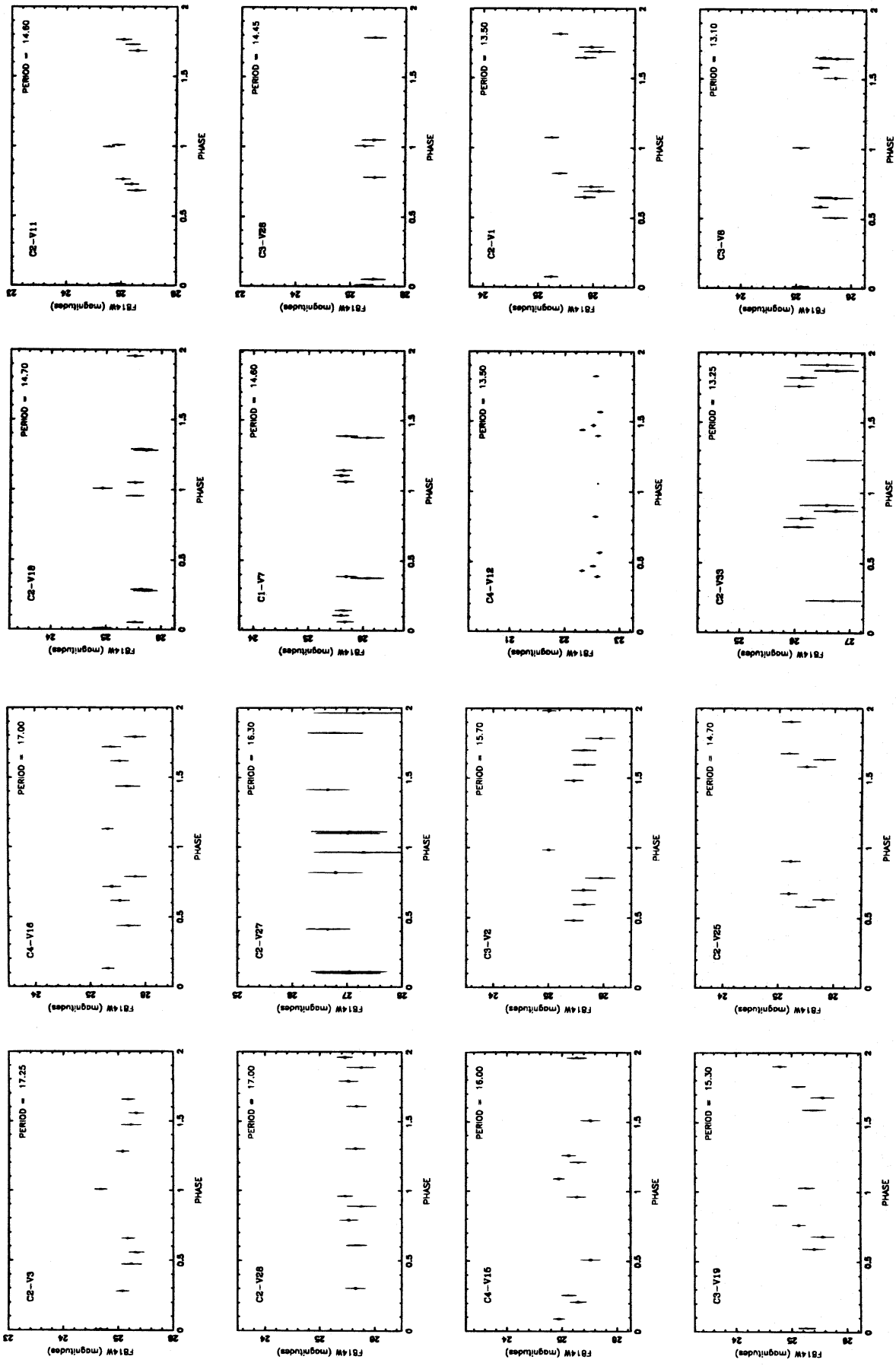

FIG. 4.—*Continued*

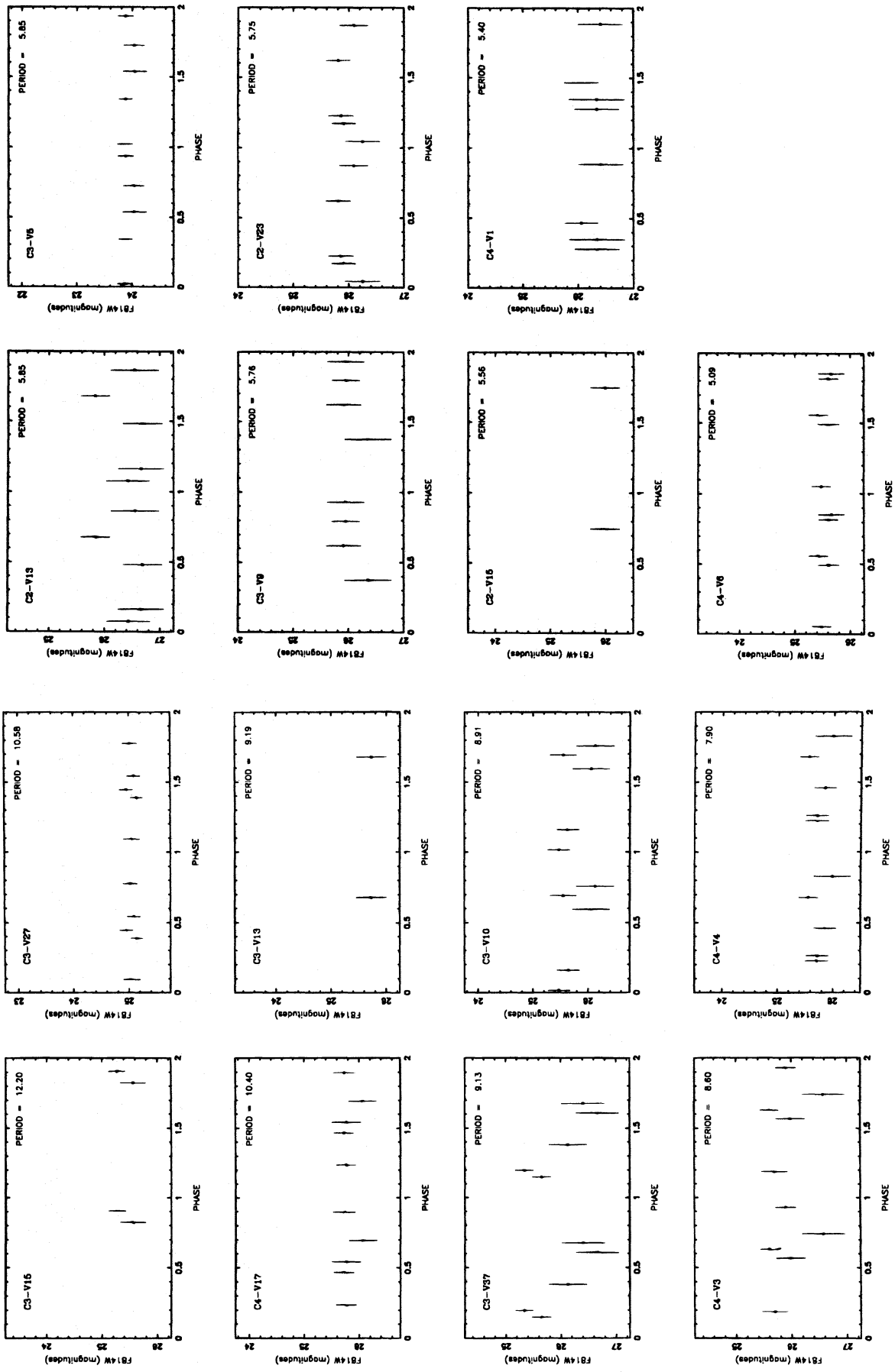

FIG. 4.—*Continued*

TABLE 3

CHARACTERISTICS OF THE CEPHEIDS

Object	Period (days)	$< V >$	$\sigma(< V >)$	$< I >$	$\sigma(< I >)$	Quality Index	Position Index
C1-V1	41.90	27.16	0.31	25.62	0.22	3	4
C1-V2	24.00	26.17	0.17	24.71	0.12	2	3
C1-V3	30.20	26.10	0.12	24.91	0.14	5	4
C1-V4	20.50	26.11	0.12	25.35	0.16	4	3
C1-V5	32.00	25.71	0.09	24.69	0.09	6	1
C1-V6	35.60	25.81	0.10	24.45	0.10	5	3
C1-V10	38.00	25.37	0.07	24.30	0.08	6	1
C2-V1	13.50	26.26	0.16	25.62	0.17	5	1
C2-V3	17.25	26.19	0.17	25.10	0.13	3	3
C2-V4	28.70	25.81	0.18	25.06	0.15	6	4
C2-V6	27.20	26.05	0.16	25.39	0.22	6	3
C2-V8	59.00	24.74	0.05	23.87	0.05	6	1
C2-V9	58.00	25.39	0.12	24.45	0.11	4	4
C2-V11	14.60	26.27	0.21	24.93	0.14	3	4
C2-V13	5.85	27.56	0.60	26.49	0.37	0	1
C2-V14	53.20	25.12	0.07	24.17	0.08	5	2
C2-V16	33.00	25.31	0.09	24.43	0.07	4	1
C2-V18	14.70	26.40	0.21	25.68	0.18	2	3
C2-V19	19.08	25.97	0.14	25.02	0.11	6	1
C2-V20	21.25	26.21	0.22	25.18	0.19	6	3
C2-V21	18.70	26.00	0.15	25.57	0.18	5	2
C2-V22	42.00	25.61	0.13	24.85	0.13	5	2
C2-V23	5.75	27.34	0.47	26.08	0.24	0	1
C2-V25	14.70	26.06	0.15	25.15	0.17	1	1
C2-V26	19.35	25.81	0.11	25.24	0.11	3	1
C2-V28	17.00	27.15	0.35	25.48	0.18	1	1
C2-V29	30.00	26.14	0.14	25.31	0.20	6	1
C2-V30	30.90	25.75	0.11	24.85	0.10	5	1
C2-V34	31.00	25.93	0.15	25.08	0.11	4	1
C2-V35	34.00	26.17	0.18	25.07	0.15	2	1
C2-V36	34.30	25.24	0.07	24.54	0.13	4	1
C3-V2	15.70	26.52	0.21	25.39	0.18	5	1
C3-V3	65.00	24.80	0.13	23.99	0.13	5	4
C3-V4	19.20	26.69	0.23	25.35	0.18	2	1
C3-V7	22.30	26.06	0.14	24.88	0.11	4	3
C3-V8	13.10	26.29	0.18	25.30	0.18	4	1
C3-V9	5.76	27.28	0.46	25.91	0.35	1	1
C3-V10	8.91	27.21	0.53	25.64	0.27	1	4
C3-V11	25.50	25.53	0.11	24.70	0.11	5	3
C3-V12	23.10	25.18	0.09	24.32	0.11	5	4
C3-V15	12.20	27.22	0.43	25.38	0.19	1	4
C3-V16	29.80	25.87	0.14	24.15	0.10	6	4
C3-V18	24.30	26.00	0.18	25.10	0.16	4	4
C3-V20	26.00	25.92	0.16	24.79	0.16	3	4
C3-V21	63.00	25.13	0.08	23.78	0.06	5	4
C3-V22	36.50	25.33	0.11	24.43	0.11	5	4
C3-V24	28.00	25.55	0.09	24.16	0.07	4	1
C3-V25	59.00	24.49	0.06	23.36	0.05	4	2
C3-V28	14.45	26.28	0.17	25.40	0.20	2	2
C3-V30	17.40	25.85	0.12	24.97	0.16	2	2
C3-V31	28.70	25.62	0.10	25.27	0.14	4	1
C3-V32	39.50	25.60	0.07	24.40	0.08	6	1
C3-V33	19.70	25.76	0.10	24.97	0.11	1	1
C3-V34	20.50	26.37	0.19	25.53	0.20	2	1
C3-V35	18.70	26.01	0.11	25.45	0.24	5	2
C3-V36	22.00	26.38	0.17	25.39	0.19	1	1
C3-V37	9.13	26.96	0.26	25.81	0.31	4	1
C4-V1	5.40	27.07	0.31	26.25	0.39	0	1
C4-V3	8.60	26.52	0.19	25.81	0.25	0	1
C4-V4	7.90	27.00	0.31	25.72	0.24	0	1
C4-V5	24.40	25.50	0.09	24.81	0.13	5	1
C4-V8	50.00	25.32	0.07	24.21	0.08	5	1
C4-V10	17.80	25.90	0.13	25.43	0.22	6	1
C4-V13	55.00	25.41	0.07	24.06	0.06	5	1
C4-V14	24.50	25.78	0.11	24.80	0.10	3	1
C4-V15	16.00	26.40	0.19	25.19	0.16	4	1
C4-V16	17.00	26.10	0.14	25.43	0.17	1	1
C4-V17	10.40	26.49	0.18	25.74	0.21	2	2

TABLE 3—*Continued*

Object	Period (days)	$\langle V \rangle$	$\sigma(\langle V \rangle)$	$\langle I \rangle$	$\sigma(\langle I \rangle)$	Quality Index	Position Index
C4-V18	17.40	26.40	0.17	25.15	0.13	5	1
C4-V19	22.70	26.61	0.21	24.90	0.12	2	2
C4-V20	58.00	25.34	0.08	23.27	0.05	3	4
C4-V21	18.70	26.40	0.23	25.74	0.24	4	4
C4-V23	17.40	26.37	0.16	25.33	0.22	4	1

putative overall reddening), there is greater spillage of points outside the I strip boundaries than is the case for the V data. The intrinsic scatter from the mean P-L relation should in fact be smaller in I than in V, both, because the projection of the instability strip on the P-L plane is narrower in I than in V, and also because if the source of the observed spread is differential extinction, the effect will be smaller in I than in V. Again, this leads to the strong suspicion that the scatter is caused by errors in the I measurements rather than by problems in absorption (there is no effect in V).

5.3. *Probing Systematic Effects in the Photometry*

At first sight the data look perfectly self-consistent in V but not in I, and we must try to get some handle on the quality of the I magnitudes. The error estimates reported in the individual photometric measurements are listed in Table 2. They define the uncertainties of the mean magnitudes, $\sigma(\langle V \rangle)$ and $\sigma(\langle I \rangle)$, given in Table 3. However, these values do not accurately reflect the noise from confusion errors due to quasi-resolved objects in the field. It is expected that such noise will be larger in redder passbands (from the nature of the color-magnitude diagram, to be discussed in the Appendix) in such objects. This is further exacerbated by the fact that the WFPC2 has much lower sensitivity in I than in V. The overwhelming effect of confusion noise is to result in an object being mismeasured brighter than it really is, particularly near the faint limit of the data (see Saha & Hoessel 1990 for a detailed discussion and examination of this problem).

The best way to understand such noise is to simulate synthetic stars of known brightness, sprinkle them over the real data, and see what magnitudes are recovered. Unfortunately, the acute undersampling of the instrument makes such a test impossible in principle. This is because we do not really know the PSF structure at the subpixel level. The observed pixellated PSF can be seen to alter with the subpixel location of the star's centroid. This is extremely difficult to model without knowing the true subpixel scale PSF. Thus synthetic stars are difficult to produce, and if done incorrectly will lead to spurious systematic effects that can only mislead.

An alternate way is to look for signatures (1) in the data, or (2) in the position of the Cepheids relative to the dense regions of the spiral arms, each of which can clue us to the problem. In particular, does separating objects by their quality index delineate systematic effects in the photometry? Also, if this is a problem from confusion noise, is there systematic variation within the photometry that depends on the background surface brightness? We look for both these effects in this section. Positional effects are discussed in § 5.4. Differential absorption is addressed in the Appendix.

Let us first define three quantities following precepts in Madore (1982), as follows, which facilitate the probing for systematic effects

$$U_V = 2.76 \log P + 1.40 + \langle V \rangle , \quad (6)$$

$$U_I = 3.06 \log P + 1.81 + \langle I \rangle , \quad (7)$$

$$U_T = U_V - R'_V(U_V - U_I) , \quad (8)$$

where R'_V is the ratio of total to selective absorption $A_V/E(V-I)$. Following Scheffler (1982), who gave $A_V/A_I = 1.7$, $R'_V = 2.43$. The three quantities above can be calculated for each Cepheid from the photometry in Table 3. If the P-L relation had no width, U_V and U_I would correspond to the

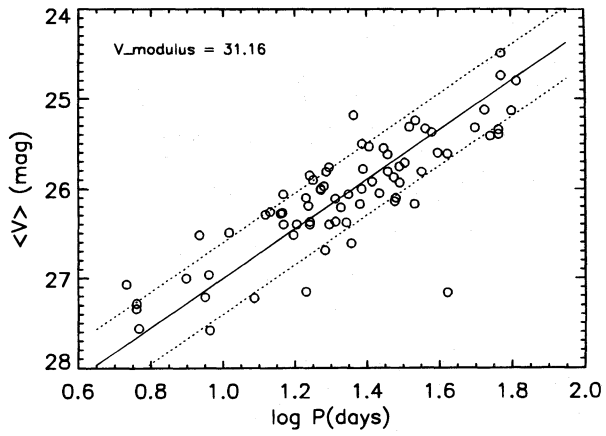

FIG. 5.—P-L relation in standard V (except for the 0.05 mag systematic effect not corrected for) for all Cepheids in Table 3 of all quality classes and all position classes relative to the spiral arms. The ridgeline has the canonical slope of −2.76. Envelope lines are put at ±0.4 mag from the ridgeline. Apparent V distance modulus is $(m - M)_{AV} = 31.16$.

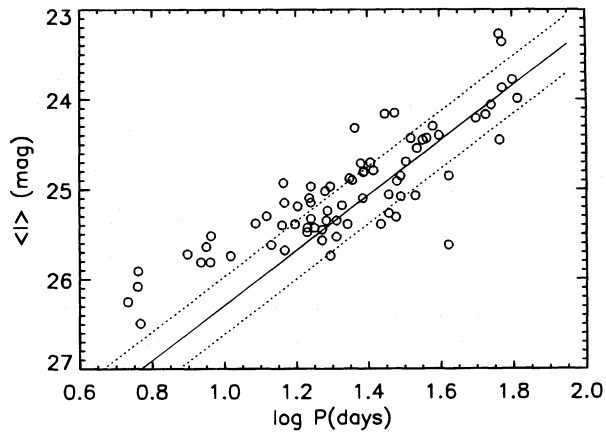

FIG. 6.—P-L relation in fully converted I magnitudes using the data in Table 3 (except for the 0.05 mag offset). The ridge line has the canonical slope of −3.06. Envelope lines are put at ±0.32 mag from the ridge line. Obvious deviation brightward of the ridgeline for log $P < 1.3$ is proved in the Appendix not to be due to differential absorption. We suspect, from the analyses in Figs. 7 and 8 and in the Appendix, that the deviation is due to measuring errors.

TABLE 4

CHARACTERISTICS OF THE VARIABLES NOT CLASSIFIED AS CEPHEIDS

Object	Period (days)	⟨F555W⟩	Type	Remarks
C1-V7	14.60	27.15	Cepheid?	F814W too faint
C1-V8	24.4	27.29	?	no F814W data
C1-V9	5.69	27.28	Cepheid?	inconsistent phasing of F814W data
C2-V2	12.40	27.38	Cepheid?	no F814W data
C2-V5	32.2	25.54	?	affected by hot pixel
C2-V7	41.0	25.70	?	no F814W data
C2-V10	18.1	26.49	Eclipsing?	
C2-V12	8.78	26.84	?	
C2-V15	5.56	27.58	Cepheid?	only one F814W measurement
C2-V17	6.65	27.47	Cepheid?	no F814W data
C2-V24	41:	27.88	?	uncertain period; inconsistent phasing of F814W data
C2-V27	16.3	27.35	?	F814W too faint
C2-V31	8.68	27.74	Cepheid?	no F814W data
C2-V32	>70	25.91	LPV?	period longer than observing window
C2-V33	13.25	27.37	Cepheid?	F814W too faint
C3-V1	17.7	26.24	Eclipsing?	
C3-V5	5.85	24.34	Eclipsing?	
C3-V6	8.80	27.23	Cepheid	no F814W data
C3-V13	9.19	27.56	Cepheid	only one F814W measurement
C3-V14	27.8	24.64	Cepheid?	
C3-V17	23.5	26.64	?	inconsistent phasing of F814W data
C3-V19	15.3	26.33	?	
C3-V23	22.9	26.55	Cepheid?	no F814W data
C3-V26	41.0	25.73	?	
C3-V27	10.58	27.57	?	
C3-V29	30.0	27.16	?	
C4-V2	7.24	27.14	?	no F814W data
C4-V6	5.09	27.04	?	
C4-V7	22.8:	27.51	?	incomplete photometry
C4-V9	5.1:	27.54	?	incomplete photometry, no F814W data
C4-V11	20.6	25.84	?	inconsistent phasing of F814W data
C4-V12	13.50	24.84	?	
C4-V22	41.0:	25.11	Cepheid?	incomplete light curve

apparent distance moduli in V and I respectively in accordance with equations (4) and (5). In reality they give the apparent moduli with the caveat that an individual Cepheid can lie away from the mean ridge line of the P-L relation. U_T is similarly akin to the true modulus, where the effect of reddening/extinction has been removed on an *object-by-object basis*. Thus the effects of any differential extinction would be absent when comparing U_T from one object to another. However, random errors in photometry and the displacement of individual Cepheids from the mean P-L relation contribute to large object-to-object scatter in U_T, further amplified by the R'_V term. Even so, it has two redeeming properties: (1) it is reddening free on an object-by-object basis (but errors in the colors will propagate large uncertainties) and (2) the mean of U_T from an ensemble of Cepheids formally equals the mean true modulus derived from mean apparent moduli in V and I which are used to solve for a mean reddening. When probing for systematic effects object by object, U_T has the advantage that the effects of reddening are already formally removed, so that any subsequent cuts in the data made on the basis of U_T are free from all extinction issues, provided that our adopted value of R'_V is reasonable. Propagating the uncertainties of $\langle V \rangle$ and $\langle I \rangle$ gives the uncertainty $\sigma(T)$ of the reddening-free "T" passband:

$$\sigma^2(T) = (1 - R'_V)^2 \sigma^2(\langle V \rangle) + R'^2_V \sigma^2(\langle I \rangle) . \quad (9)$$

$\sigma(T)$ is the amount by which U_T would scatter about the true distance modulus μ_0 if there were no width of the P-L relation. If we account for this width, and characterize it by rms values ρ_V and ρ_I for the two passbands, the total rms scatter $\sigma_{\rm tot}$ in U_T about μ_0 is:

$$\sigma^2_{\rm tot} = \sigma^2(T) + \sigma^2_{\rm width} , \quad (10)$$

where

$$\sigma^2_{\rm width} = R'^2_V(\rho_V - \rho_I)^2 + \rho^2_V , \quad (11)$$

where the fact that displacement from the mean P-L relation correlates in the two passbands has been accounted for. This quantity is useful if one wants to make a weighted average of U_T to derive the true distance modulus. We adopt $\rho_V = 0.20$ and $\rho_I = 0.16$, so that the 2 σ boundaries come out to 0.40 mag and 0.32 mag on either side of the mean P-L relation in V and I respectively, which gives $\sigma_{\rm width} = 0.22$ mag.

An examination of Figure 7, where various measured (or derived from measurement) quantities for each Cepheid in Table 3 are plotted against the quality index (QI) is very instructive for understanding the systematic effects. The top left panel shows that the QI deteriorates at short periods, but above log $P = 1.2$, all but the very worst quality light curves are present. U_V shows very little if any systematic dependence on the QI (not very surprising since the objects were selected on the basis of the V data, which are also of superior quality than the I data), but U_I does. The sense of the variation is as we had suspected: poorer QI shows brighter recovered magnitudes as would be the case if the source is confusion noise, or objects against the faint detection limit. The most telltale dependence is the variation of U_T, which indicates almost continuous trend upward with

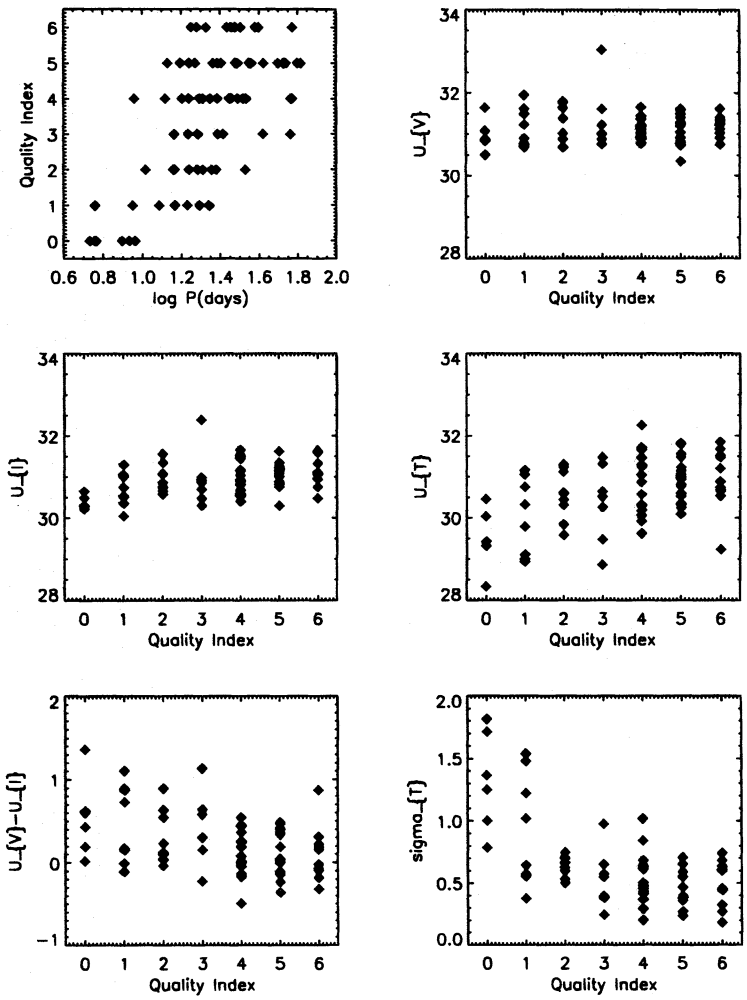

FIG. 7.—Various tests for possible correlations of the period, the apparent distance moduli in V and in I, and the measured (total) sigma of the combined V and I photometry with the "quality index" for individual Cepheids in Table 3, attempting to identify the cause of the deviation of the I points from the ridgeline in Fig. 6 at short period.

increasing QI. The lower envelope of U_T changes rapidly from QI values 3–6, though the upper envelope is more nearly constant. The bottom right panel shows the expected strong dependence between QI and $\sigma(T)$.

Even at the longest periods, objects with QI as low as 3 are present. Thus a cut that discards objects with short periods (which in itself introduces no bias with respect to deriving a reddening free distance) is inadequate for removing all systematic effects.

The first four panels in Figure 8 show how QI, U_T, σ_T and the color of the object correlate against the background value (in pixel data numbers on the co-added F814W image) near the object. This is a test to see if object confusion (which should increase with background level) is the source of photometry problems. Objects in the PC chip are not included in these plots, since the background values as well as resolution are quite different for it. We see no definite trends in any of the quantities plotted, except that the very reddest objects prefer higher values of background. However, the background surface brightness is not by itself a clear indicator of any problems.

The lower left panel of Figure 8 may, at first, seem extremely surprising. It shows a strong correlation of the *extinction corrected* modulus U_T with color, covering a range of 1.5 mags in color. Only objects with $\log P \geq 1.3$ are plotted, so that faint-end selection bias (see Figures 5 and 6) is eliminated. If reddening were the cause of the entire color range, there should be *no* correlation in this diagram. There may be small effects at the reddest and bluest colors due to the finite width of the instability strip, but the range of U_T should still stay within an an rms range of 1.2 mag. The conclusion is that the observed range of $(\langle V\rangle - \langle I\rangle)$ cannot be due to differential extinction alone. The dominant contribution is from observational errors. The point is made more explicity in the Appendix.

The bottom right panel of Figure 8 shows the regression of $(\langle V\rangle - \langle I\rangle)$ on $\sigma_{\rm tot}$, which has been defined in equations (9)–(11), from which it is clear that all $(\langle V\rangle - \langle I\rangle)$ values occur at all values of $\sigma_{\rm tot}$. Thus the colors do not seem to be related to any *accountable* errors. Of the sources of unaccounted for errors, confusion noise is the most suspect, but again we have seen no trends with surface brightness. The occurrence of warm and hot pixels on the CCDs can be mapped (from the lists posted in the STScI data archive) to check if they coincide with objects of extreme color. This does not result in anything interesting, and nor do we expect it to, since why would it then preferentially affect the I data?

We have learned from Figure 6, that the I magnitudes for short period Cepheids are biased. Thus in what follows, we use only objects for which $\log P$ is 1.3 or larger, where at least there is no definite problem of the slope of the

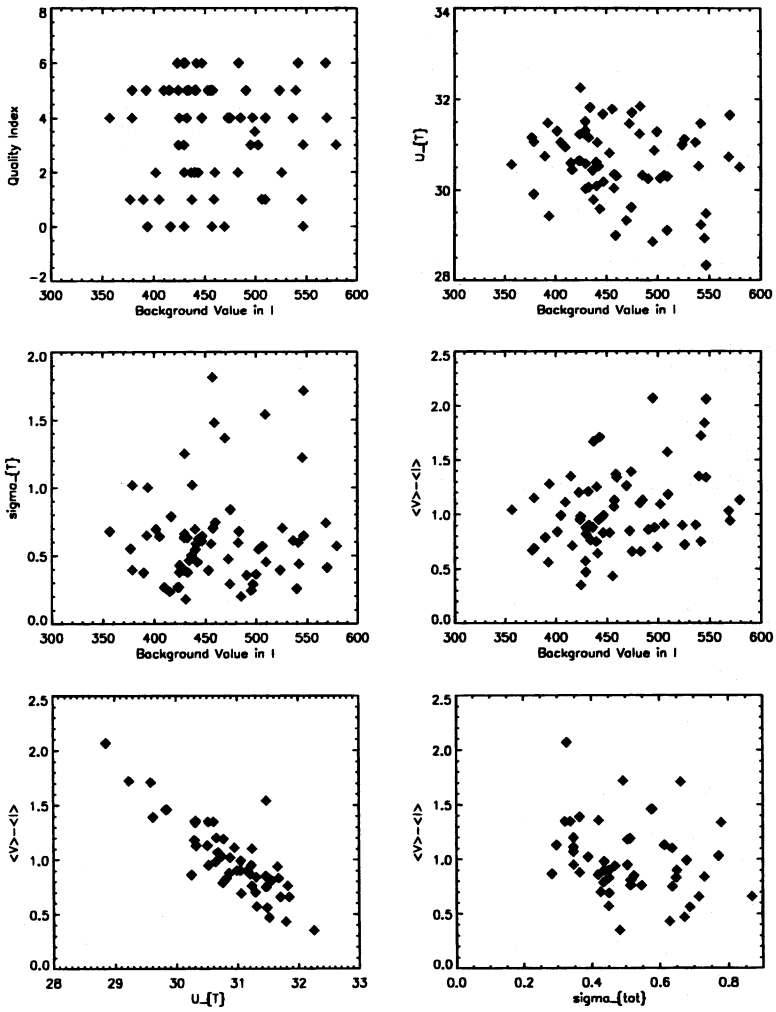

FIG. 8.—Similar to Fig. 7 but using the measured background level, the "quality index," and the ($\langle V\rangle - \langle I\rangle$) color correlations with each other. Strong correlation of color with "true" distance modulus in the lower left panel is a clue that the spread in colors is *not* due to differential absorption, as discussed in the text.

observed *P-L* relation with respect to the canonical one from Madore & Freedman (1991). In addition, we reject those objects for which we have assessed *QI* to be less than 4. For this sample of 36 Cepheids, the apparent distance modulus in V is $\mu_V \equiv (m-M)_V = \langle U_V\rangle = 31.18 \pm 0.05$ mag; similarly the apparent distance modulus in I is $\mu_I = 31.11 \pm 0.06$, and the dereddened modulus $\mu_0 = \langle U_T\rangle = 31.00 \pm 0.11$ mag. The average reddening is $E(V-I) = 0.07$ mag. Note that the cuts in period and *QI* are perfectly unbiased with respect to distance derivation. This cut, which selects objects with relatively better data, does, in effect, reject all but one object with $V-I > 1.4$. The one that remains is C3-V16, which has $V-I = 1.72$ with $QI = 6$. If we reject C3-V16 for its color excess, we get $\mu_V = 31.18 \pm 0.05$, $\mu_I = 31.13 \pm 0.05$, and $\mu_0 = 31.06 \pm 0.10$ mag. If we include only objects with $QI \geq 5$, and also reject C3-V16, we again get from a smaller (but better *QI*) sample $\mu_V = 31.18 \pm 0.06$, $\mu_I = 31.13 \pm 0.06$, and $\mu_0 = 31.06 \pm 0.10$ mag.

In an alternate approach, we start with only a period cut, including periods where $\log P \geq 1.3$, and allowing objects even with *QI* as low as 0. We then calculate the quantity $\langle U_T\rangle$, reject objects whose U_T deviates from this mean by more than 2 $\sigma_{\rm tot}$ and iterate. This rejects objects where the internal accounting for errors is inadequate at the 2 σ level. When this procedure converges (in this case in 2 iterations) we take the *weighted* mean for $\langle U_T\rangle$, using $1/\sigma^2_{\rm tot}$ as weights. This gives $\mu_0 = \langle U_T\rangle = 31.05 \pm 0.13$ mag. A starting sample of 49 objects was pared to 42 accepted objects. If we begin with an initial cut demanding $QI \geq 3$, the process converges in one step, with 37 final objects, and $\mu_0 = 31.07 \pm 0.14$ mag.

In the end it is satisfying to note that these several reasonable but different starting assumption and/or convergence procedures arrive at essentially the same answer for the true modulus. Moreover, μ_V is essentially insensitive to almost any cut. In light of the above exercises, we adopt:

$$\mu_V = 31.18 \pm 0.05 \quad (12)$$

$$\mu_0 = 31.05 \pm 0.13 \quad (13)$$

This implies a formal total mean reddening of $E(V-I) = 0.05 \pm 0.04$ mag, or equivalently $E(B-V) = 0.04 \pm 0.04$ mag, as well as

$$\mu_B = 31.22 \pm 0.05\,. \quad (14)$$

Note that the values in equations (12)–(14) do not include the +0.05 effect for "long" exposures (cf. §§ 3.3 and 6.2). In the next subsection we treat the data with a different approach, segregating the Cepheid data by position relative to the spiral arm and relative to background and crowding. We retain the quality index criterion but determine the distance modulus and mean reddening separately in four posi-

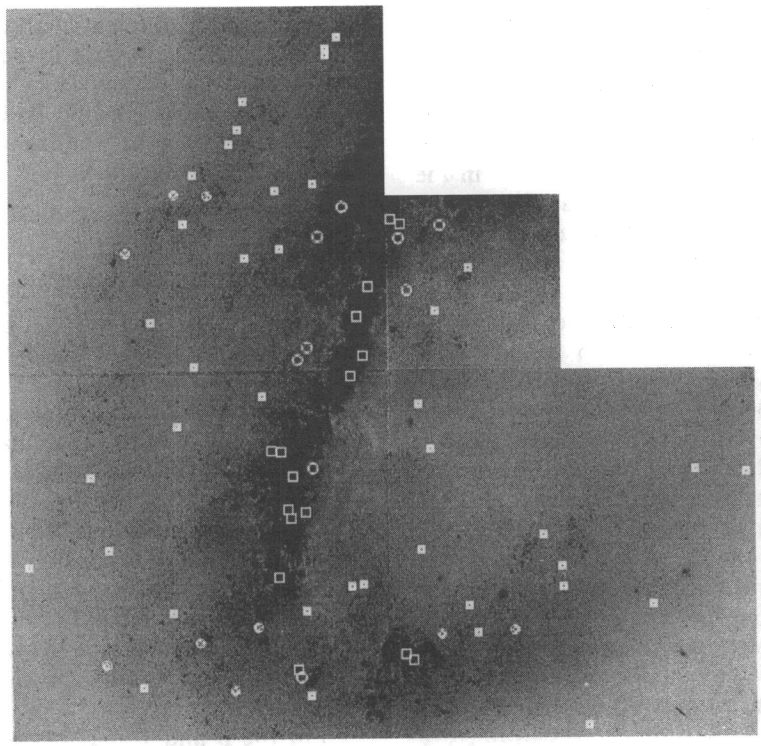

FIG. 9.—Positions of the Cepheids in Table 3 are plotted in a mosaic of the four chips, showing the relation of the variables to the spiral arm (compared also with Figs. 1 and 2). Symbol shapes refer to the position indices 1 (*filled squares*), 2 (*filled circles*), 3 (*open circles*), 4 (*open squares*) of Table 3.

tions. The results are closely the same as in equations (12)–(14).

5.4. *Cepheid P-L Relations Discussed Separately for Different Regions of NGC 4536*

The Cepheids are spread over the entire face of the northwest section of NGC 4536 in both the interarm areas and the area *within* the evident principle arm. Figure 9 is a mosaic of the four *HST* CCD chips marked with all the 73 Cepheids that are in Table 3.

We have searched for differences in the *P-L* relation, in the color distribution, in the period distribution, and in the apparent V and I distance moduli in and out of the obvious spiral arm region. To facilitate the search we have assigned four position classes to the Cepheid sample, listed in the final column of Table 3. Cepheids in position class 1 are in the cleanest, lowest background areas of the field, well away from any part of the spiral arm. Cepheids in position class 4 are well into the densest parts of the arm, often along its ridge line as seen in Figure 9. Positions 2 and 3 are intermediate. The position-class identifications are shown in Figure 9 and can be seen more clearly by collating the listings in the final column of Table 3 with the detailed identification of each variable in the higher resolution maps of Figures 2*a*–2*d*.

5.4.1. *Search for Color and Period Differences with Position*

We first looked for a color variation with position by binning the color distributions separately for each of the four position classes, with and without the restriction of log $P > 1.3$. *The color distributions prove to be nearly identical for all four position classes when the data are restricted to quality class 4 and above.* The colors range between $(\langle V\rangle - \langle I\rangle)$ of 0.6 to 1.4 with a mean of 0.95 for color variations in all four positions. However, when the quality classes 0 to 3 were binned, the *reddest* $(\langle V\rangle - \langle I\rangle)$ colors were found in position class 4, whereas the color distribution, and the mean color as well, in position classes 1–3, even for quality class 0–3, are the same as in the first binning that restricted the sample to the higher quality data. Clearly then, the observed extreme red colors for the *poorest* quality class data in position class 4 are due to observational errors, not to differential extinction (i.e., position class 4 Cepheids of quality class 4, 5, and 6 are not redder than the average in the interarm region). This absence of differential reddening was, to be sure, proved by the lower left diagram in Figure 8 and also by the equivalent argument in the Appendix, but is confirmed here by this color distribution analysis.

We next looked for a difference in the distribution of period with position. Such a difference could be suspected because the youngest Cepheids are expected to be in the arms where the most recent star formation has occurred. Such Cepheids should have the longest periods because of the age-period relation for Cepheids in general (Kippenhahn & Smith 1969; Tammann 1970).

The distributions of period with position in the four position bins are not greatly different. Periods greater than 50 days occur in position classes 1, 2, and 4. While it is true that only 10% of the Cepheids in position class 1 (the truly interarm region) have periods greater than 50 days compared with 24% of the Cepheids in position class 4, yet such young long-period variables do occur over the entire region, *including* the interarm position class 1. Our data are too sparse to gauge if this slight difference in the period distribution between position classes 1 and 4 is real. Nevertheless, what is certain is that the longest period Cepheids are not confined entirely to the spiral arms. Significant star formation is occurring outside the arms. Massey et al. (1996) have shown that the same is true in M33 where a significant fraction of the massive young OB stars are now forming outside the evident associations.

5.4.2. *Search for Differences in the P-L Relations With Position*

For the purposes of this paper, the most important difference to be expected would be in the apparent *P-L* relations in V and I between position classes 4 and 1. Such a difference, if found, would most reasonably be explained by differential absorption, the absorption being strongest in the arm region. Limits on any putative differential absorption, are, of course, of crucial importance in determining the "best" value of the distance modulus from the data in Table 3.

In view of the obvious problem with the I data for $\log P < 1.3$, seen in Figure 6, and further of quality class 0–3 seen in the correlations in Figures 7 and 8, we have considered only those Cepheids from Table 3 of quality class 4, 5, and 6 with $\log P > 1.3$. Note particularly that we *make no color cut here* (i.e., all colors are accepted) so as not, in this section, to bias against possible differential absorption, the proper size of which we wish to determine now *by position arguments alone.*

We have determined separate distance moduli in V and in I from separate *P-L* relations using equations (4) and (5). The results are shown in Table 5. The data have been variously binned to optimize the small-number statistics because the sample is now cut to only 30 Cepheids by the restrictions in $\log P$ and QI.

Column (1) defines the subsamples by position. Column (2) is the apparent V distance modulus, found from equation (4) and the apparent magnitudes in Table 3 for the relevant Cepheids. Column (3) is the same for the apparent I modulus using equation (5). The number of Cepheids in the subsample is in column (4). Treating the differences between columns (2) and (3) as real gives the "reddening," $E(V-I)$, from which the "absorption" follows as $2.43E(V-I)$ in V and $1.43E(V-I)$ in I. The quoted error on the resulting "true" modulus in column (5) is compounded by the average of the two values, one from the apparent V modulus and the other from the apparent I modulus. The mean color of those Cepheids in the sample, taken from Table 3, is in column (6).

The results are nearly identical with the values adopted in equations (12) and (13) of § 5.3 where all the data were used, but with various analyses of error models, Hence the values in the adopted equations (12)–(14) are clearly robust.

Taken at face value, the difference in the apparent distance moduli between position classes 1 + 2 and 3 + 4 in Table 5 could be interpreted as a differential absorption of 0.10 ± 0.10 mag in V and 0.05 ± 0.10 mag in I. Although hardly significant, the *smallness* of the differential effect in and out of the spiral arm proves beyond doubt that differential absorption is not a problem at more than a generous 0.10 mag level. The same conclusion is proved in another way by using the lower left diagram in Figure 8, and by the equivalent proof in the Appendix.

If indeed the differential absorption between the arm and the interarm region were, in fact, 0.10 mag in V, the predicted mean color difference in the values listed in the final column of Table 5 would be $0.10/2.43 = 0.04 \pm 0.04$ mag, fortuitously close to what is observed, although again not statistically significant.

6. ABSOLUTE PEAK BRIGHTNESS OF SN Ia 1981B

6.1. *Observed Brightness and Color*

The SN 1981B in NGC 4536 was discovered about a week before maximum. Extensive photometric (Leibundgut 1988; Phillips 1993; Schaefer 1995 and references therein) and spectroscopic (Branch et al. 1982, 1983) observations were obtained for the object. All available observations show the object to be a "normal" type Ia supernova. It was not red at maximum like SNe 1986G and 1991bg, its spectrum is Branch normal (Branch et al. 1993), its decay rate of $\Delta m_{15}(B) = 1.10$ (Phillips 1993; Schaefer 1995) is average, and the minimum expansion velocity of 6450 ± 50 km s^{-1} as measured by the red edge of the Ca II H and K lines lies close to the mean value (Fisher et al. 1995). The fact that SN 1981B was a normal type Ia event to all knowledge makes it particularly important for the luminosity calibration of SNe Ia.

For the B and V maxima we adopt the values given by Schaefer (1995)

$$B_{\max} = 12.04 \pm 0.04 , \quad (15)$$

$$V_{\max} = 11.96 \pm 0.04 . \quad (16)$$

The agreement with Phillips (1993; $B_{\max} = 12.03$, $V_{\max} = 11.96$) is excellent. For the above solution Schaefer (1995) has used all data taken up to 20 days after B maximum. His alternative solution using data taken up to 80 days post-maximum is more vulnerable to subtle changes in the light curve morphology, but gives only slightly different results: $B_{\max} = 12.04$ and $V_{\max} = 12.00$. We adopt his 20 day cutoff solution as being a less biased measure of the maximum brightness per se. Thus

$$B_{\max} - V_{\max} = 0.08 \pm 0.06 . \quad (17)$$

We know from Cadonau (1986) and Leibundgut et al. (1991), that the V maximum occurs about 2.5 days after the B maximum and that

$$(B-V)_{B(\max)} = B_{\max} - V_{\max} - 0.02 , \quad (18)$$

which implies that

$$(B-V)_{B(\max)} = 0.06 \pm 0.06 . \quad (19)$$

6.2. *Extinction to SN 1981B and Its Peak Absolute Brightness*

The supernova SN 1981B was situated in a part of the host galaxy that is similar to the region where the Cepheids

TABLE 5

APPARENT DISTANCE MODULI AS A FUNCTION OF POSITION RESTRICTED TO QUALITY INDEX 4, 5, 6, AND $\log P > 1.3$

POSITION (1)	$(m-M)_{AV}$ (2)	$(m-M)_{AI}$ (3)	n (4)	$(m-M)_0$ (5)	$(\langle V\rangle - \langle I\rangle)$ (6)
1	31.19 ± 0.08	31.12 ± 0.09	14	31.02 ± 0.16	0.94 ± 0.08
1 + 2	31.19 ± 0.07	31.13 ± 0.09	17	31.04 ± 0.15	0.94 ± 0.07
3 + 4	31.29 ± 0.07	31.18 ± 0.06	13	31.02 ± 0.12	0.97 ± 0.07
4	31.35 ± 0.09	31.26 ± 0.09	7	31.13 ± 0.18	0.98 ± 0.09
1 + 2 + 3 + 4.....	31.23 ± 0.05	31.15 ± 0.06	30	31.04 ± 0.11	0.96 ± 0.04

were discovered. To zeroth order, we can assume that the mean extinction to the Cepheids [which is small, at $E(B-V) = 0.04$, as shown above] is the same as to SN 1981B. This may in fact be mainly due to Galactic foreground extinction, although Burstein & Heiles (1984) give $A_B = -0.02$ for NGC 4536, because Branch et al. (1983) have detected Ca II H and K absorption in the spectrum of SN 1981B from the Galactic interstellar medium at $v = 0$ km s^{-1}.

Combining equations (12) and (16) *and adding the 0.05 mag correction for "long" exposures* as discussed at the end of § 3.3, gives the peak brightness in V

$$M_V(\max) = -19.27 \pm 0.14 . \quad (20)$$

Using equations (14) and (15), we get the peak brightness in B

$$M_B(\max) = -19.23 \pm 0.15 . \quad (21)$$

Note that the uncertainties from equations (12) and (16) and from (14) and (15) result in internal uncertainties of 0.06 mag for both equations (20) and (21). However, we quote larger values, since in reality the implied assumption made here that SN 1981B had the same extinction as the Cepheids carries some uncertainty, and we use the uncertainty from equation (13) in lieu of (12) or (14).

These absolute magnitudes are derived from the assumption that SN 1981B has the same extinction as the average Cepheids in position classes 1 and 2 (see § 5.4) in NGC 4536. However, there is evidence that the SN suffers *more* absorption than the Cepheids and that therefore the peak luminosities in equations (20) and (21) are too faint. This is discussed in the following.

Direct evidence for additional non-negligible absorption of SN 1981B comes from Branch et al. (1983). They have observed the interstellar K line at the redshift of NGC 4536 with an equivalent width of 139 mÅ and concluded from this that $E(B-V)$ is "perhaps 0.2" mag. The same authors obtained a value of $E(B-V) = 0.12$ from blackbody fits to the optical and infrared spectra at various epochs 10–90 days after maximum. Buta & Turner (1983) suggested an uncertainty in the reddening of $E(B-V) = 0.14$. Schaefer (1995) has shown that the mean color of SNe Ia at B maximum is $(B-V)^0 = 0.00 \pm 0.04$, if it is assumed that all normal SNe Ia have the same intrinsic color. Together with equation (19) this yields

$$E(B-V) = 0.06 \pm 0.07 . \quad (22)$$

These various estimates do not constrain the reddening well, but a value of $E(B-V) = 0.10 \pm 0.05$ is plausible. With $R_B = 4$ and $R_V = 3$, the total absorption of SN 1981B becomes $A_B = 0.40 \pm 0.20$ or equivalently, $A_V = 0.30 \pm 0.15$. This leads to dereddened values of

$$B^0_{\max} = 11.64 \pm 0.20 , \quad (23)$$

and

$$V^0_{\max} = 11.66 \pm 0.16 , \quad (24)$$

implying, from equation (13) plus the 0.05 mag correction for "long" exposures, the intrinsic peak brightness (i.e., using the dereddened modulus)

$$M_B(\max) = -19.46 \pm 0.24 , \quad (25)$$

and

$$M_V(\max) = -19.44 \pm 0.21 . \quad (26)$$

These values are brighter than the results in equations (20) and (21), but carry somewhat larger uncertainties that make the two estimates consistent within the errors. The values are also within the errors of our previous calibration of SNe Ia (Saha et al. 1995) from IC 4182 (SN 1937C) and NGC 5253 (SN 1895B, SN 1972E).

The adopted values of SN 1981B then become

$$M_B(\max) = -19.29 \pm 0.13 , \quad (27)$$

and

$$M_V(\max) = -19.32 \pm 0.12 \quad (28)$$

as the weighted means of equations (20), (21), (25), and (26) and where the estimated errors are more realistic than the internal formal values that are a factor of 2 smaller.

7. THE HUBBLE CONSTANT

It is premature to give a definitive discussion of the state of the calibration of SNe Ia by simply adding this fourth calibration to the three already known from the first two experiments for SN 1895B, SN 1937C, and SN 1972E (Saha et al. 1994, 1995). This is because we have now completed the calibrations in the next two experiments (Saha et al. 1996) for SN 1960F in NGC 4496A and SN 1990N in NGC 4639. A proper discussion must also account for any putative decay rate versus luminosity correlation (Pskovskii 1977, 1984; Phillips 1993), however small, that can begin to be investigated when the values for the six calibrators are known (four with the present result and the two new results in NGC 4496A and NGC 4639). Such an argument is being made in the archive paper for NGC 4639 (Saha et al. 1996), and has already been made in summary form in its Letters announcement (Sandage et al. 1996).

What is important here is to point out that the present result for a SN Ia in an Sbc spiral (NGC 4536) belies the suggestion of Hamuy et al. (1995) that SNe Ia in irregular galaxies, E and S0 galaxies, and/or in dwarfs, may be different than in the regular spirals of the Hubble sequence. There is no such effect in these new data, as was also shown in the wider data divided into spirals and E galaxies in Figure 4 of Tammann & Sandage (1995). The Hubble lines for SNe Ia in spirals and in E/S0's differ by only 0.02 mag in the Hubble diagram set out in this reference.

We take the weighted mean calibration of the four available SNe Ia whose reductions have now been completed (this paper plus Saha et al. 1995, Table 7), but retain the larger of the mean uncertainties from the weighted and unweighted methods, giving

$$\langle M_B(\max) \rangle = -19.48 \pm 0.12 , \quad (29)$$

based on four SNe Ia, and

$$\langle M_V(\max) \rangle = -19.47 \pm 0.10 , \quad (30)$$

based on three SNe Ia.

These values lead to Hubble constants of

$$H_0(B) = 55 \pm 3 \text{ km s}^{-1} \text{ Mpc}^{-1} , \quad (31)$$

and

$$H_0(V) = 58 \pm 3 \text{ km s}^{-1} \text{ Mpc}^{-1} \quad (32)$$

using the ridge line equations of the Hubble diagrams in Tammann and Sandage (1995) and where we have used our adopted values from equations (27) and (28). Had we used the absolute magnitude values for SN 1981B alone from equations (27) and (28) we would have obtained $H_0(B) = 60 \pm 4$ km s^{-1} Mpc^{-1} and $H_0(V) = 62 \pm 4$ km s^{-1} Mpc^{-1}.

We thank the many individuals at the STScI who have worked hard behind the scenes to make this program possible. A. Saha wishes to thank Leonard Searle for the hospitality he enjoyed while on sabbatical at OCIW, where this work was completed. A. Sandage and A. Saha acknowledge the support of NASA through the Space Telescope Science Institute for grant support for this project to determine H_0 through SNe Ia. L. L. and G. A. T. thank the Swiss National Science Foundation for financial support.

APPENDIX

PROOF THAT THE LARGE COLOR VARIATION OF THE CEPHEIDS IS NOT DUE TO DIFFERENTIAL REDDENING

We give here a diagram that shows in a transparent way that differential reddening does not exist in the Cepheid data of Table 3, and therefore that the large color variation seen in the lower quaality class data in NGC 4536 is due to some cause other than reddening.

The point is of great importance so as to avoid accepting all the color data as real, applying the "reddening corrections," and deriving a "true modulus" from the calculation (Madore 1976 in his rediscussion of the modulus of NGC 2403, and van den Bergh & Pazder 1992 in their SN "absorption" corrections). We present a definitive method to prove either the presence or absence of differential absorption by use of a diagram that uses only observed quantities.

A1. CEPHEID COLOR DATA IN THE CM DIAGRAM

To illustrate the color problem in NGC 4536 we show, in Figure 10, the color-magnitude diagram for the data in Table 3. The magnitude values are in the (interim) "ground" system discussed in § 3, which is very close (but not identical) to the standard values adopted in Table 3. The ridge and envelope lines drawn are taken from Figure 10 of the archive paper on IC 4182 (Saha et al. 1994), but transformed in ordinate for the difference in the adopted distance modulus of $(m - M)_0 = 28.36$ for IC 4182, using the (interim) modulus value marked for NGC 4536 in Figure 10. The color problem is evident for the Cepheids here. All quality classes, all periods, and all position classes (i.e., the whole of Table 3) are shown.

A2. DIAGNOSTIC DIAGRAM FOR DIFFERENTIAL ABSORPTION

Figure 11 is equivalent to the lower left diagram of Figure 8, but in a different representation. Plotted are the individual apparent V distance moduli as abscissa against the difference in the individual V and I apparent moduli as ordinate. These quantities can be determined for each Cepheid (U_V and U_I) by using equations (6) and (7). The top diagram shows the locus of the P-L relation. In the absence of reddening, the ridgeline of the P-L relation is represented by a single point. Reddening extends this point along the trajectory shown, i.e., objects on the ridgeline that suffer extinction will be observed somewhere along the central reddening trajectory. Because of the finite width of the instability strip, there will be envelope lines above and below the ridgeline, shown here at ± 0.40 mag along the abscissa from the point representing the ridgeline of the P-L relation. The locus of zero $E(V-I)$ reddening is drawn as a dashed line. It is slightly sloped because of the *intrinsic* change of color

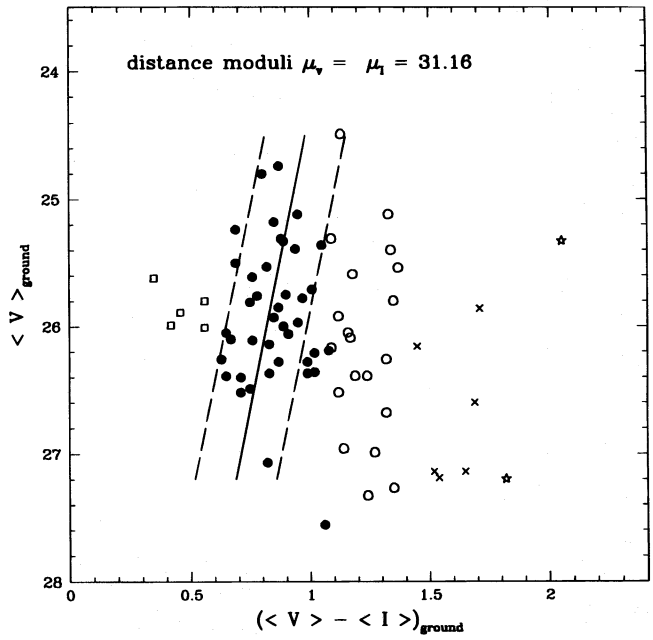

FIG. 10.—Color-magnitude plot for the Cepheids in Table 3. Ridgelines and envelope lines show the position of the Cepheid instability strip in IC 4182 (Fig. 10 of Saha et al. 1994) but transformed to the distance modulus of NGC 4536 using $(m - M)_0 = 28.36$ for IC 4182. The different symbols are used to subdivide the color range at $(\langle V \rangle - \langle I \rangle) = 0.6$, 1.1, 1.4. and 1.8.

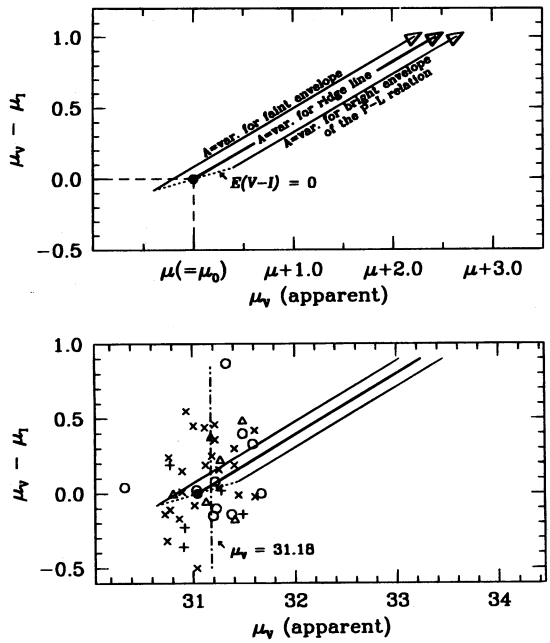

FIG. 11.—Diagnostic diagram with which to detect the presence of differential absorption. Apparent V distance modulus μ_V is the abscissa. Difference between the V and the I apparent moduli, $\mu_V - \mu_I$, is the ordinate. *Upper panel:* schematic presentation of the locus of Cepheids. Unreddened Cepheids on the ridgeline of the P-L relation are projected into a single point (*black dot*). Unreddened Cepheids within the P-L relation, but above or below the ridge line, are projected onto the dashed, slanted line (cf. text). Absorption moves individual Cepheids along the absorption lines (*full lines*). *Lower panel:* contours in the upper panel are repeated. In addition the Cepheids in Table 3 with Quality Index 4, 5, and 6 are shown. Symbols stand for position indices 1, 2. 3, and 4 (Table 3) with crosses plus signs, triangles, and open circles, respectively. The mean apparent Cepheid modulus is $\mu_V = 31.18$ (*dashed-dotted line*). Lack of adherence to the locus of absorption proves the absence of measurable differential absorption.

across the instability strip even in the absence of reddening. In the absence of reddening, and when observational errors are zero, all Cepheids should fall along this dashed line.

In essence, the top diagram shows the mapping of the P-L relation into these coordinates in an obvious way. If differential absorption is present, the Cepheid data should follow the slope of the ridgeline. Scatter about this line will be due to the intrinsic width of the instability strip *plus* errors in the data.

The bottom part of Figure 11 shows the 44 Cepheids with $QI \geq 4$. The apparent V and I distance modulus of each Cepheid are calculated from the data given in Table 3. There is no trend along the reddening trajectory. There is simply scatter. Whatever the cause of the scatter, it clearly is not due to differential reddening.

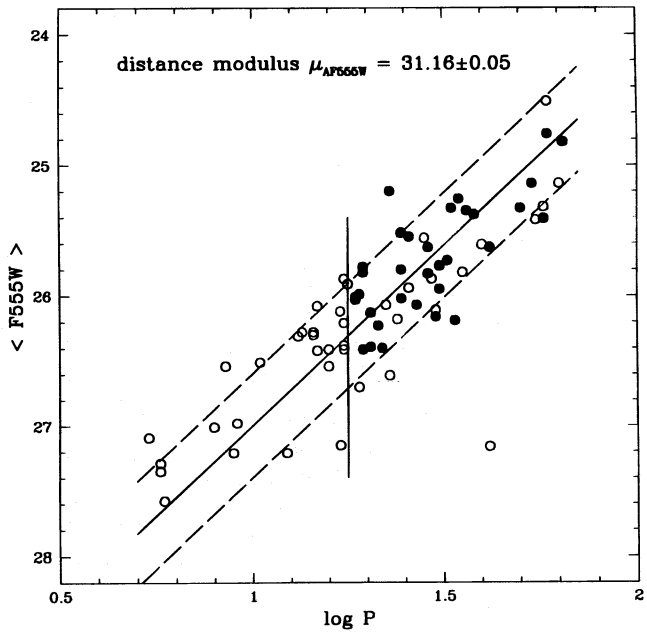

FIG. 12.—P-L relation in F555W for all the Cepheids in Table 3, but with a cut at log $P = 1.25$. Filled dots are for those variables with (⟨F555W⟩ − ⟨F814W⟩) bluer than 1.10. The ridge line has the slope of eq. (4).

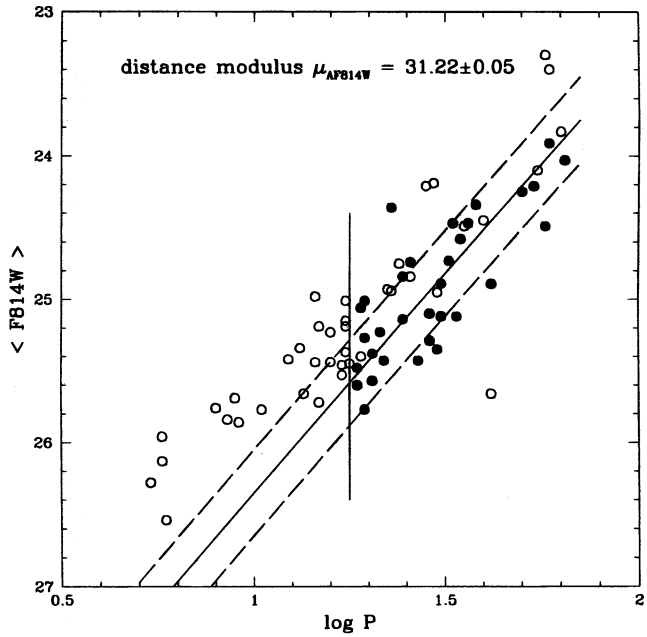

FIG. 13.—*P-L* relation in F814W for all Cepheids in Table 3, but with a cut at log $P = 1.25$. Filled circles are for those variables with colors bluer than 1.10. The ridgeline has the slope of eq. (5).

A3. *P-L* RELATIONS USING A PERIOD AND A COLOR CUT

Having proved now, via Figure 8 (lower left) and Figure 11 here, that the color variation among the Cepheids in NGC 4536 is not *primarily* due to differential reddening, we can logically make a color cut in the data without introducing a bias in $(m - M)_0$ that would have been present had differential reddening been present. Figure 12 shows the *P-L* relation in F555W with the ridge and envelope lines drawn using the slope of equation (4). A period cut is made at log $P = 1.25$. A color cut is also made at an instrumental color of 1.10. The resulting apparent modulus for the points plotted as solid dots agrees well with the apparent V modulus adopted in the text. (The 0.05 mag correction for the short/long exposure offset has *not* been applied in this diagram).

Figure 13 shows the same analysis for the F814W band. Again, the 0.05 mag offset has *not* been applied to the data or to the listed mean modulus in the diagram.

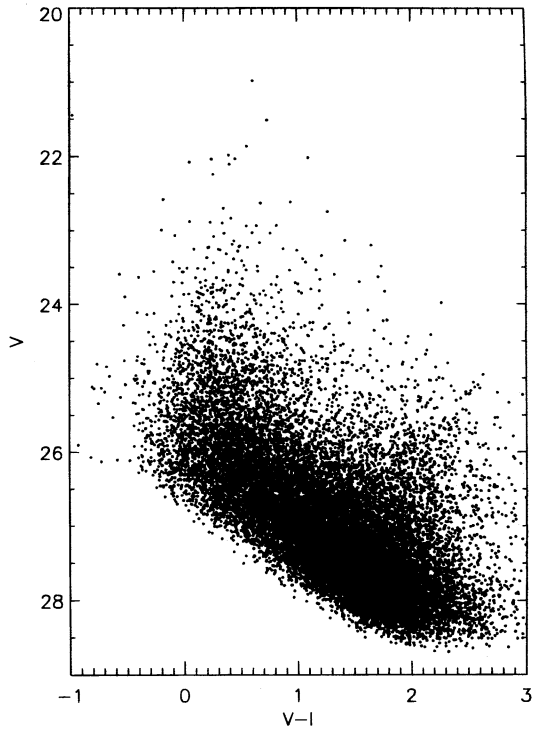

FIG. 14.—Color-magnitude diagram made from all stars detected on the deep combined (all epochs together) images in F555W and F814W

A4. COLOR-MAGNITUDE DIAGRAM

Finally, for completeness, we show in Figure 14, without comment, the color-magnitude diagram (CMD) of the stars measured in the master template catalog discussed in § 2. The mean of the brightest three blue supergiants is at $\langle V \rangle = 22.0$, corresponding to $B_V = -9.3$, fully consistent with the calibration of brightest stars known previously (e.g., Sandage & Carlson 1985) using $M_B(T)^{0,i} = -20.66$ for NGC 4536. We leave as a problem the apparent absence of the expected red giant branch, not really seen, if at all. Its tip should be near $V = 23.3$ in Figure 14.

REFERENCES

Binggeli, B., Sandage, A., & Tammann, G. A. 1985, AJ, 90, 1681
Binggeli, B., Tammann, G. A., & Sandage, A. 1987, AJ, 94, 251
Branch, D., et al. 1982, ApJ, 252, L61
———. 1983, ApJ, 270, 123
Branch, D., Fisher, A., Herczeg, T. J., Miller, D. L., & Nugent, P. 1994, ApJ, 421, L97
Branch, D., Fisher, A., & Nugent, P. 1993, AJ, 106, 2383
Branch, D., & Miller, D. L. 1993, ApJ, 405, L5
Branch, D., & Tammann, G. A. 1992, ARA&A, 30, 359
Burstein, D., & Heiles, C. 1984, ApJS, 54, 33
Buta, R. J., & Turner, A. 1983, PASP, 95, 72
Cadonau, R. 1986, Ph.D. thesis, Univ. Basel
Feast, M., & Walker, A. R. 1987, ARA&A, 25, 345
Fisher, A., Branch, D., Höflich, P., & Khokhlov, A. 1995, ApJ, 447, L73
Hamuy, M., Phillips, M. M., Maza, J., Suntzeff, N. B., Schommer, R. A., & Aviles, R. 1995, AJ, 109, 1
Harris, H. C., Hunter, D. A., Baum, W. A., & Jones, J. H. 1993, AJ, 105, 1196
Holtzman, J. A. 1995, private communication
Holtzman, J. A., et al. 1995a, PASP, 107, 156
———. 1995b, PASP, 107, 1065
Kippenhahn, R., & Smith, L. 1969, A&A, 1, 142
Labhardt, L., Sandage, A., & Tammann, G. A. 1996, A&A, submitted
Lafler, J., & Kinman, T. D. 1965, ApJS, 11, 216
Leibundgut, B. 1988, Ph.D. thesis, Univ. Basel
Leibundgut, B., Tammann, G. A., Cadonau, R., & Cerrito, D. 1991, A&AS, 89, 537
Madore, B. F. 1976, MNRAS, 177, 157
———. 1982, ApJ, 253, 575
Madore, B. F., & Freedman, W. L. 1991, PASP, 103, 933
Massey, P., Armandroff, T. E., Pyke, R., Patel, K., & Wilson, C. D. 1996, ApJ, in press
Mateo, M., et al. 1996, in preparation
Phillips, M. M. 1993, ApJ, 413, L105
Pskovskii, Yu, P. 1977, Soviet Astron., 21, 675
Pskovskii, Yu, P. 1984, Soviet Astron., 28, 658
Saha, A. 1996, in preparation
Saha, A., et al. 1996 in preparation (Papers VI, VII)
Saha, A., & Hoessel, J. G. 1990, AJ, 99, 97
Saha, A., Labhardt, L., Schwengler, H., Machetto, F. D., Panagia, N., Sandage, A., & Tammann, G. A. 1994, ApJ, 425, 14 (Paper II)
Saha, A., Sandage, A., Labhardt, L., Schwengeler, H., Tammann, G. A., Panagia, N., & Macchetto, F. D. 1995, ApJ, 438, 8 (Paper IV)
Sandage, A. 1988, ApJ, 331, 605
———. 1995, Practical Cosmology, Inventing the Past in the Deep Universe (23rd SAAS Fee Course), ed. B. Binggeli & R. Buser (Springer: Berlin), 170
———. 1996, Bias Properties of Extragalactic Indicators, AJ, in press
Sandage, A., & Carlson, G. 1985, AJ, 90, 1464
Sandage, A., Saha, A., Tammann, G. A., Labhardt, L., Schwengeler, H., Panagia, N., & Macchetto, F. D. 1994, ApJ, 423, L13 (Paper III)
Sandage, A., Saha, A., Tammann, G. A., Panagia, N., & Macchetto, F. D. 1992, ApJ, 401, L7 (Paper I)
Sandage, A., et al. 1996, ApJL, in press
Sandage, A., & Tammann, G. A. 1968, ApJ, 151, 531
———. 1993, ApJ, 415, 1
———. 1996, Two Lectures on the Observational Determination of the Hubble Expansion Rate Erice, Sicily, 3rd D. Chalonge School, Nov. 1994, in Current Topics in Astrofundamental Physics, ed. R. Sanchez (Singapore: World Scientific), in press
Schaefer, B. E. 1995, ApJ, 449, L9
Schechter, P. L., Mateo, M. L., & Saha, A. 1993, PASP, 105, 1342
Scheffler, H. 1982, in Landolt-Börnstein, Astronomy & Astrophysics, Vol. 2c, ed. K. Schaifers & H. H. Voigt (Berlin: Springer), 46
Stetson, P. B. 1995, private communication
Tammann, G. A. 1970, in IAU Symp. 39, The Spiral Structure of our Galaxy, ed. W. Becker & G. Contopoulos (Dordrecht: Reidel), 236
Tammann, G. A., & Sandage, A. 1995, ApJ, 452, 16
van den Bergh, S., & Pazder, J. 1992, ApJ, 390, 34